NUMERICAL INVESTIGATIONS ON THE AERODYNAMICS OF OVERTAKING MANEUVERS USING SIMPLIFIED ROAD VEHICLE MODELS

by

Bhaskara Kalyan Veeraghanta

A thesis submitted to the faculty of
The University of North Carolina at Charlotte
in partial fulfillment of the requirements
for the degree of Master of Science in
Mechanical Engineering

Charlotte

2021

Approved by:

_____
Dr. Mesbah Uddin

_____
Dr. Amirhossein Ghasemi

_____
Dr. Jun Xu

ABSTRACT

BHASKARA KALYAN VEERAGHANTA. Numerical investigations on the aerodynamics of overtaking maneuvers using simplified road vehicle models. (Under the direction of DR. MESBAH UDDIN)

Studying aerodynamics using Computational Fluid Dynamics (CFD) analysis of external flows is a crucial element in the design and development of modern-day road and racing vehicles. Although a plethora of both experimental and computational data related to aerodynamic optimization of isolated vehicle geometries is available in existing literature, very little is known about the complex aerodynamics involving vehicle interactions especially during an overtaking maneuver which has always been a field of interest in motorsports. The costs and difficulties associated with experimental studies of such intricate vehicle interactions using realistic vehicle geometries are often unreasonable due to geometric complexities and complexities involved with the various measurement techniques employed. The objective of this study is to validate and develop a CFD methodology that can be used to explore and analyze the flow fields of such complex aerodynamic phenomena associated with an overtaking maneuver using the Ahmed Body geometries. This is realized by first developing a simulation methodology for isolated Ahmed Bodies (with slant angles (ϕ) 25^o and 35^o respectively) owing to the availability of experimental data for validation of the CFD models and then utilizing the overset meshing technique in a virtual wind tunnel wherein one body is kept stationary whereas a small relative motion is specified to the trailing body in the longitudinal direction. The simulations were run in STAR-CCM+, a commercial CFD code. The work presented aims to discuss the effects of lateral distancing on the various aerodynamic parameters of both overtaken and overtaking bodies and to compare the wake region of the overtaken body in various homogeneous and heterogeneous configurations of Ahmed bodies.

ACKNOWLEDGEMENTS

I would like to to begin by thanking Dr. Mesbah Uddin for foreseeing my capabilities and taking me under his tutelage, for all the countless hours given in counsel, encouragement, and support throughout the length of this project. This research would not have molded into form without his constant guidance and criticism. I would also like to thank all the professors and the committee members, Dr. Amirhossein Ghasemi and Dr. Jun Xu, for their valuable insights during my time at UNC Charlotte. I am grateful and thankful to all my colleagues in the lab who have played a crucial role in the progress of this work. I would also like to thank Ms. Tracy Beauragard for her invaluable support throughout my term at UNC Charlotte, the Department of Mechanical Engineering, the College of Engineering, The Graduate School at UNC Charlotte, and the UNC Charlotte High Performance Computing group for their support throughout the length of this venture. I will forever be grateful for the patience and understanding from my family and friends, who have always been extremely supportive and encouraging throughout the course of my research.

DEDICATION

Mom and dad, this is for you. Everything I have and everything I am, I owe it all to you.

TABLE OF CONTENTS

LIST OF TABLES

LIST OF FIGURES

CHAPTER 1: INTRODUCTION

The aerodynamics of present-day road vehicles and racing cars is a very interesting, and highly intricate and complex phenomenon requiring an in-depth understanding of the transient behavior of vehicle interactions despite the abundance of existing literature and modern developments in the field. With dwindling natural resources owing to the lack in supply of fossil fuels and the high rate of consumption of fossil fuels by the transportation sector, conservation of energy is of utmost importance which is directly attributed to the fuel efficiency of the vehicles. This can be arrived at by focusing on the reduction in the coefficient of drag of vehicles. Not only will reducing the drag coefficient increase the fuel efficiency of vehicles, it will also assist in the quest to reach higher speeds in the field of motorsports.

The influence of aerodynamic properties on the performance of vehicles can be analysed with the use of isolated bluff bodies. A bluff body (such as an Ahmed body [3]) is fundamentally an isolated vehicle that can mimic the aerodynamic characteristics of a real vehicle without having all the complex geometrical features of a real vehicle. While extensive literature exists on understanding the flow around such bodies, the implications of turbulence exerted by external sources such as proximity of other stationary or moving objects is yet to be fully understood as in the case of an overtaking maneuver or platooning. These flow interactions between moving vehicles become more prominent at higher speeds in applications such as racing, leading to concerns over the safety of sports thereby making it an area of interest to study.

Modern-day technological advancements have strongly aided in the study of such multi-vehicle interactions. Along with wind tunnel studies and track testing, modern-day Computational Fluid Dynamics (CFD) tools have proven to be an important tool

to analyze the aerodynamics of such complex interactions. The costs and difficulties associated with experimental studies of such intricate vehicle interactions using realistic vehicle geometries are often unreasonable due to geometric complexities and complexities involved with the various measurement techniques employed thereby making CFD an important tool to study automotive aerodynamics and assist in the design and development of road and racing vehicles. CFD is also a much faster and cost-effective mode of analysis along with being more robust and reliable, and allows for introduction of engineering data and design optimization even in the early stages of research and development of a vehicle.

1.1 Motivation

Aerodynamics plays a crucial role in modern day motorsports where every hundredth of a second counts towards a victory. When two or more bodies are in close proximity to one another, the flow interactions due to the presence of each body on the other body(ies) result in highly intricate changes in the flow field in and around the system of bodies. These changes can result in flow excitation that can alter the aerodynamic forces, moments, and the wake region of each body. In order to understand these effects, researchers have carried out quasi-steady and quasi-static studies wherein two or more bodies were kept at predetermined intervals relative to each other. While these studies have provided invaluable data and an understanding of the flow patterns during such interactions, they fail to exhaustively explain the transient behavior of such interactions as the effects of relative velocity between the bodies is not accounted for, along with the assumption of a steady flow, which is not the case in a real life scenario.

As modelling such transient effects experimentally in wind tunnels is an expensive, time consuming, and a laborious process for full-scale vehicle geometries, and since it's nearly impossible to have the same track conditions to allow for a reliable track test for such studies, CFD can be used as an important tool to bridge the gaps in knowledge

and help understand the transient behavior on a deeper level. With the advent of autonomous vehicles, and the presence of vehicles with partial to full automation being more prevalent, it is very important to ensure the safety of the occupants inside self-driven vehicles. Along with the safety aspect, it is also important to ensure that the passengers inside self-driving vehicles feel comfortable as if the vehicle is being chauffeured by a real person. This is accomplished by developing real-time path planning approaches by using predictive behavior-based control modules. During an overtaking maneuver, the additional aerodynamic forces and moments which act on the overtaking and overtaken bodies can lead to displacements in the transverse axis and changes in the yawing moments of both the vehicles, thereby complicating the steering corrections that have to be performed by the drivers in both vehicles. The instabilities due to these steering corrections can lead to compromising the safety of vehicles in situations such as in cases of adverse weather conditions if the control modules are unable to correctly predict such behavior in self-driving vehicles. This investigation aims to study the effects of a realistic overtaking maneuver at highway speeds on the changes in transient aerodynamic forces and moments of two-vehicle homogeneous and heterogeneous systems that can be used to help model such control modules or sequences for trajectory planning of future vehicles with partial or full automation.

In the past, the influence of longitudinal spacing and relative velocity on the transient flow conditions have been studied. One of the earliest studies in the field was conducted by Yamamoto et al. [17] where they experimentally studied the dynamic aerodynamic influence of large overtaking vehicles on the motion stability of other smaller vehicles using $1/10^{th}$ scale models and observed that even a small change in relative velocity resulted in a significant change in the flow field. Following this, Noger and Gillerion [13], [18], [19], [14] conducted several experimental studies of an overtaking maneuver using $1/5^{th}$ passenger scale model cars with both quasi-static and

dynamic conditions. In their studies, it was determined that the transient forces acting on bodies in an overtaking maneuver are a function of three independent factors - longitudinal spacing, lateral spacing, and the relative velocity between the two vehicles and it was observed that as both longitudinal and lateral spacing, individually or simultaneously, decreased, there is a sharp rise in aerodynamic interactions between both the bodies. They also noticed the transient case produced lower aerodynamic coefficients as compared to a quasi-steady case, thereby agreeing with Yamamoto's results and presented the force and pressure data to validate the same. They also studied the influence of crosswinds on the aerodynamic coefficients and analyzed the transient phenomena in their experiment with an approach based on the presence of pseudo-harmonic variations of the aerodynamic coefficients to understand the importance of transient effects.

More recently, CFD was used as a tool to understand transient effects of dynamic multi-body interactions wherein newer mesh models, such as the sliding mesh model [20], [15] and overset mesh model [16] were used to capture transient effects that quasi-steady simulations fail to fully capture. The advantages of using an overset mesh model was studied by Chellaram [21]. This study aims to utilize the overset mesh model to understand the transient effects of lateral or transverse spacing during an overtaking maneuver for homogeneous and heterogeneous systems of Ahmed bodies.

1.2 Objective

The objective of this study is to develop and validate a framework of CFD methodology that can be used to explore and analyze the flow field for complex aerodynamic interactions, and to analyze the effects of lateral or transverse spacing associated with an overtaking maneuver using overset meshing technique for a system of homogeneous and heterogeneous Ahmed body geometry combinations . The author aims to present the transient effects of an overtaking phenomena on the aerodynamic coefficients and wake profile of the overtaken vehicle for different lateral spacings and to compare the

effects of lateral spacing on the two bodies in consideration. The author also aims to provide a comparison of the homogeneous system with the sets of heterogeneous systems during the overtaking maneuver at all transverse spacings. The last objective of this study is to provide a computationally less expensive methodology to analyze the transient effects of multi-vehicle interactions.

1.3 Thesis Outline

Chapter 1 introduces the reader to the objectives and the motivations behind this study. Chapter 2 provides an insight into the existing experimental and CFD literature related to multi-vehicle interactions and provides a background to the usage of Ahmed body and overset mesh technique. Chapter 3 details the numerical setup of the simulation and discusses the mesh and physics settings along with providing an insight into the solver setup and boundary conditions of the simulations. Chapter 4 discusses the validation of the numerical model used and contains the investigation into and analysis of the results of all the simulations. Chapter 5 highlights all the conclusions from this undertaking with a summary and outlines the scope for future work in this field.

CHAPTER 2: BACKGROUND AND LITERATURE REVIEW

2.1 Ahmed Body

The evolution of the functional and aesthetic design of automobiles has always been a fast changing progression since the very beginning. The modern car as we know has been through thousands of iterations in design over the period of the last century to be where it is currently. As all aerodynamic phenomena are individualistic in nature and vary depending on vehicle to vehicle, it is important to have a simplistic vehicle profile that can mimic the aerodynamic characteristics of a real vehicle without having all the complex geometrical features owing to a specific make or model in order to study the generic aerodynamic behaviour of automobiles. To fill this need, Ahmed et al. [3] introduced the Ahmed body. Ahmed body is a simplified bluff body that captures all the essential flow features of a ground vehicle model in a very simplistic form. The basic profile of an Ahmed body can be seen in Figure 2.1.

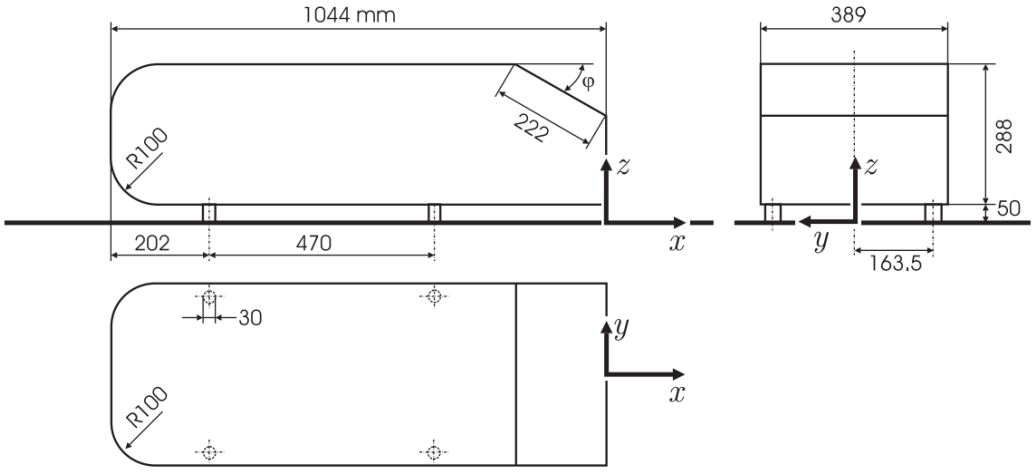

Figure 2.1: Schematic Diagram of Ahmed body (with slant angle $\phi = 25^o$) [1]

The three dimensional canonical shape of the Ahmed body along with the fixed separation point along the rear end, constrains the aerodynamic flow field while still producing the characteristic flow structures in the wake region of the model which occur in realistic ground vehicles. Ahmed body went on to become and still is one of the most widely used automotive geometries in the field of CFD to study ground vehicle aerodynamics. The main features of an Ahmed body are the flow separation and recirculation regions along the rear slant surface and the base of the body and the generation of counter-rotating C-pillar (or horseshoe) vortices along the side profile of the geometry. The front of the Ahmed body is designed such that air sticks to the length of the Ahmed body ensuring no or minimal flow separation during a fluid-body interaction at the front. The various flow structures around an Ahmed body profile can be seen in Figure 2.2.

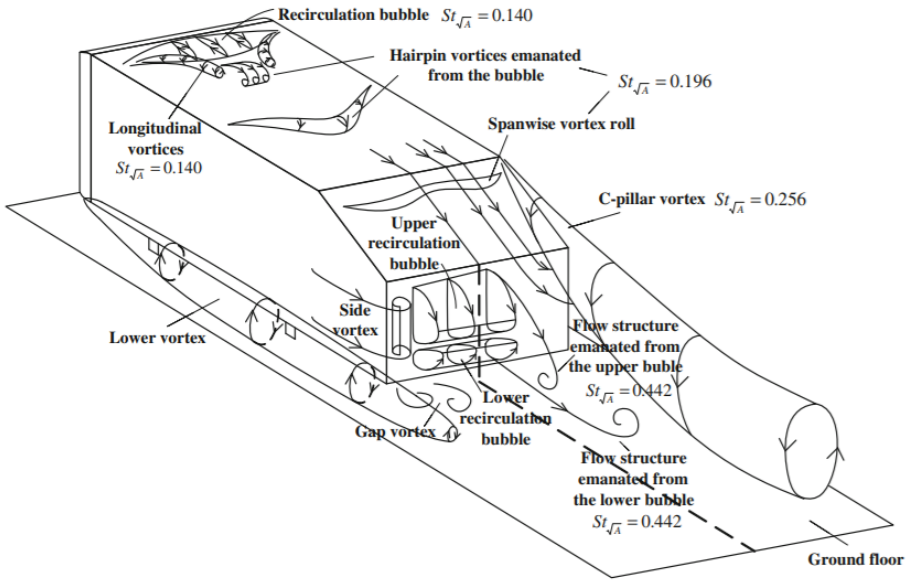

Figure 2.2: Flow Structures around an Ahmed body profile [2]

Ahmed body was originally developed to analyze the effects of the rear slant angle on the drag forces experienced by vehicles and to analyze the turbulence vortical structures thereby generated. While studying the effects of the rear slant angle on

the salient flow features of the vehicle, Ahmed et. al. [3] found out that the C-pillar vortices generated at the rear of the vehicle were dependent on the slant angle 'ϕ' at the rear of the vehicle and that nearly 85% of the induced drag on the body was due to the pressure drag generated at the rear of the vehicle. The effects of the slant angle (ϕ) on the drag coefficient observed by Ahmed et al [3] can be seen in Figure 2.3.

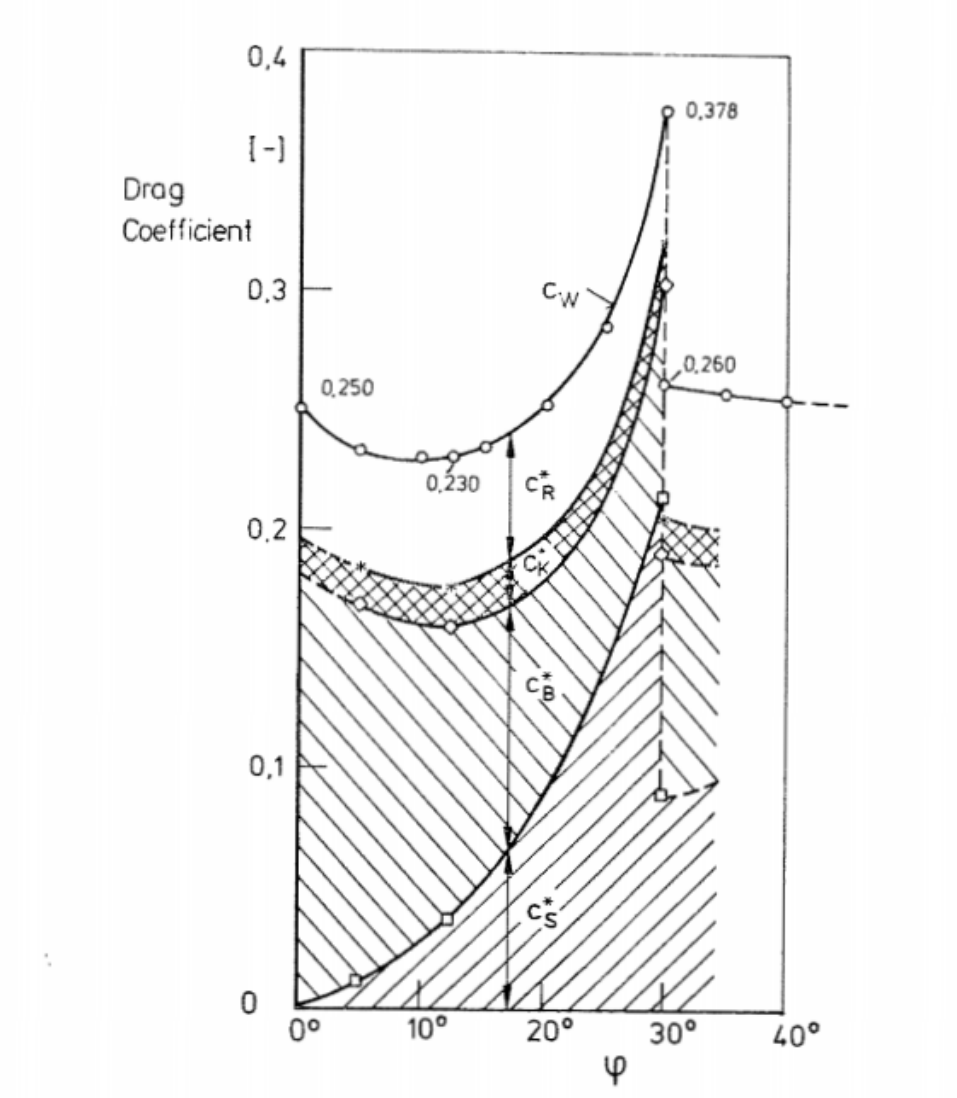

Figure 2.3: Effects of Slant angle (ϕ) on the coefficient of Drag [3]

Ahmed et. al. [3] also noticed that for smaller slant angles (when ϕ<30^o), the flow

separating at the roof-slant junction reattaches back onto the slant near the vertical base thereby forming an arch shaped separation bubble at the slant region. However as the slant angle reaches the 30^o mark, the separation bubble over the slant grows in size forming a low pressure arch vortex over the slant region that then draws in thereby strengthening the C-pillar vortices. The significant reduction in base pressure in these cases also results in a significant rise in drag values. However, as the slant angle increases beyond 30^o, the separated flow is no longer able to reattach itself onto the slant thereby decreasing the strength of the C-pillar vortices. This contributes to a rise in base pressure and therefore a reduction in drag. Due to this behavior, Ahmed body configurations with slant angles less than 30^o (or the sub-critical slant angle geometries) can be loosely perceived as 'two-box' designs such as a hatchback or a fastback whereas configurations with slant angles greater than the critical angle (or the super-critical slant angle geometries) can be looked upon as 'three-box' designs such as a notchback. Figure 2.4 represents the time-averaged flow field highlighting flow features of both sub-critical and super-critical Ahmed body configurations.

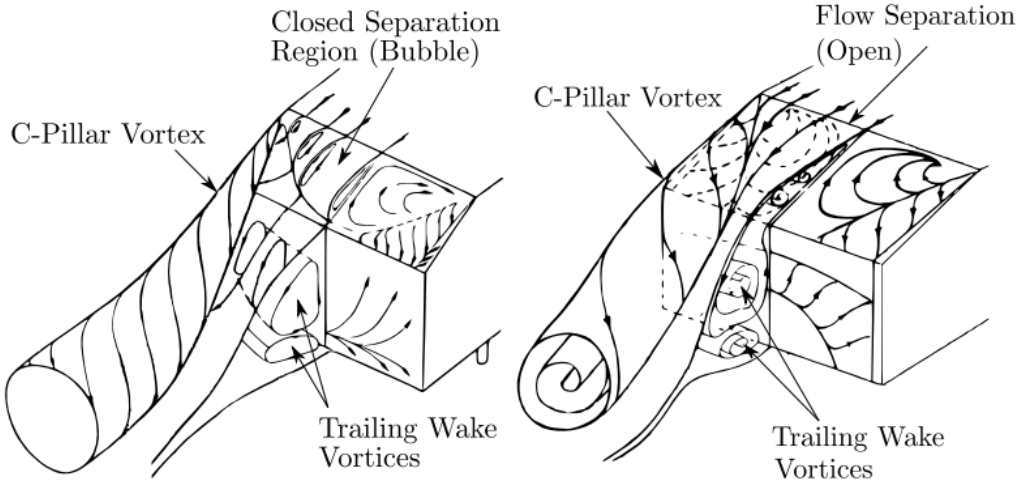

Figure 2.4: Schematic of the flow field highlighting flow features of sub-critical (on the left) and super-critical (on the right) Ahmed body configurations [4]

A plethora of both experimental and computational data related to aerodynamic

optimization of Ahmed body configurations is available in existing literature. A few prominent and well acclaimed studies that are widely accepted from the literature will be discussed here. Bayraktar et al. [5] performed one of the first studies of Ahmed body configurations with different slant angles. In their work, they investigated fluid flow around a full scale Ahmed body with various slant angles with varying yaw angles ranging from -15 to +15 degrees at a varying Reynolds number (Re). The experiments were conducted at the NASA Langley's Full-Scale Wind Tunnel in a semi-elliptical open jet test section with stationary road conditions in combination with a turntable that allowed for tests in yawed conditions. Bayraktar et al. [5] measured time averaged force coefficients and flow patterns in the wake region of the body and assessed the dependency for geometries with different slant angles at varying yaw conditions. Their results were comparable with the previous experimental studies and also gave a brief understanding of the vortex shedding in the flow on and around the Ahmed body. Figure 2.5 shows the trend of drag coefficient with respect to change in slant and yaw angles as obtained by Bayraktar et al. [5].

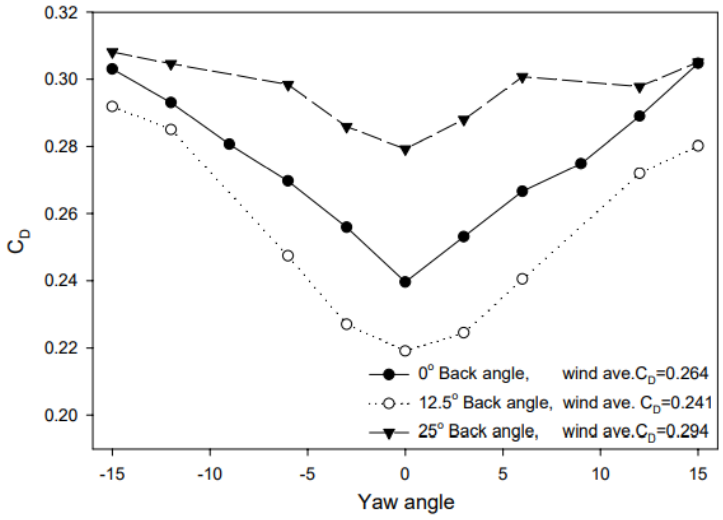

Figure 2.5: Variation in the coefficient of Drag of an Ahmed body with respect to change in slant and yaw angles [5]

Following this study, Lienhart et al. [22] used Laser Doppler Anemometry (LDA), Particle Image Velocimetry (PIV), and Hotwire Anemometer measurement techniques to study the sub-critical and super-critical slant angle configurations of Ahmed body in a stationary wind tunnel at a free stream velocity of 40 m/s and a Reynolds number of $2.29E6$. Although the higher bulk velocity in their experiment did not match with previous experiments, it was argued that the Reynolds number can be compared as it would not much affect the characteristic flow features remarkably.

Strachan et al. [23] [24] in their experiments used a moving ground wind tunnel along with LDA techniques to capture the flow field and measure the flow field parameters along with corresponding CFD simulations. A free stream velocity of 25 m/s was used which resulted in a Reynolds number of 16E5. In their experiments, they used an aerodynamic strut attached to the roof to mount the Ahmed body in the wind tunnel instead of using the stilts at the bottom. Their results were compared against that of Lienhart [22] and a matching trend was observed. However, there were certain discrepancies when their experimental data was compared with the CFD data wherein the predicted vortex shedding positions were misaligned although the main flow structures were successfully captured.

The studies conducted by Hinterberger et al. [6] were one of the first Large Eddy Simulation (LES) investigations done with Ahmed body geometries. The main objective of their study was to recreate Lienhart's work [22], using the same free stream velocity and Reynolds number values for a 25^o Ahmed body geometry, using LES and to understand the evolution of the vortical flow structures, mainly the C-pillar or horseshoe vortices, generated by the bodies and to analyze the dependency of aerodynamic properties of such flow structures. Streamwise velocity profile over the slant and the wake region as observed by Hinterberger can be seen in Figure 2.6. In their study, they also discussed the sensitivity of mesh on the prediction of the aerodynamic parameters and flow field features for an LES. Despite slight discrepancies in

the flow field at the lower regions of the slant, their results were in agreement with the existing experimental data by Lienhart.

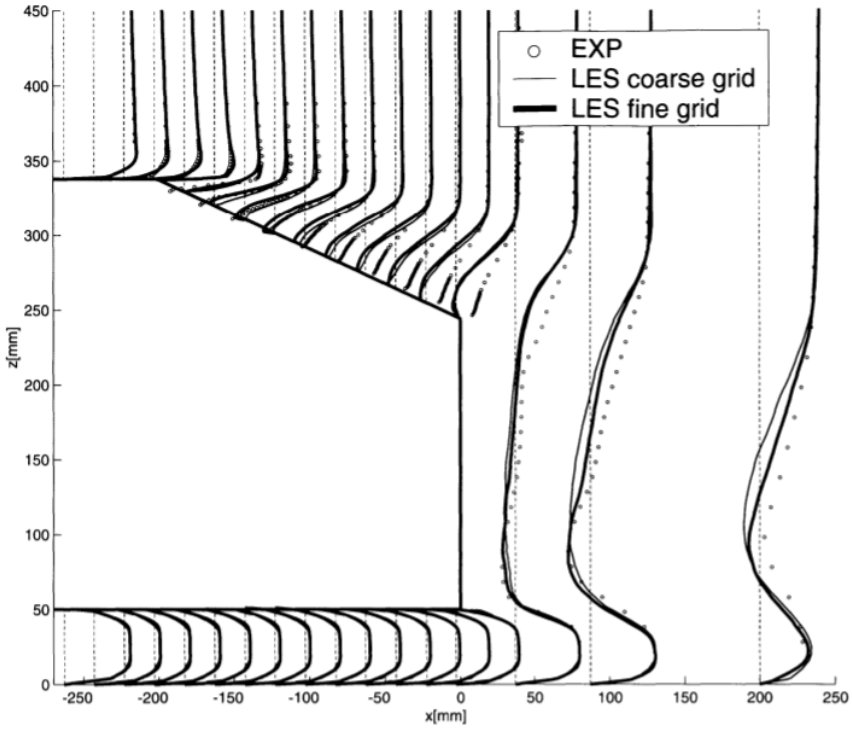

Figure 2.6: Streamwise velocity profile over the slant and the wake region as observed by Hinterberger [6]

High order LES simulations were analyzed by Minguez et al. [25] at a Reynolds number of 7.68E5. In their study, they used multi-domain spectral Chebyshev-Fourier solver to setup the simulations and LES was implemented using a Spectral Vanishing Viscosity (SVV) technique, with particular supervision at the near wall region. While the flow structures generated using the SVV-LES approach were comparable to the existing experimental data, the setup failed to accurately predict come aerodynamic properties especially the over-predicted coefficient of drag value for the body. This was due to the inability of LES to capture the finer flow features within the boundary layer and the near wall regions. While a higher resolution grid could potentially help the LES solver with the accuracy of the predictions, it would be computationally

far too expensive. As a result, the SVV-LES setup was useful in visualising the flow features around the Ahmed body but not so much in the prediction of the aerodynamic properties.

Similar results were also observed by Serre et al. [1] when they conducted LES based on spectral approximations stabilized by the SVV Method. While the separation and reattachment predictions were in good agreement, a major drawback of their study was the stern over-prediction of drag coefficient by over 44% due to the increase in the cross-sectional area owing to the presence of a confined recirculation region ahead of the body. Serre et al. [1] also conducted a Detached Eddy Simulation (DES) study as a part of the research using Menter's $K-\omega$ Shear Stress Transport (SST) turbulence model. The DES-SST model in a way is a unified LES-Reynolds Averaged Navier-Stokes (RANS) hybrid model in which the properties of a grid define the separation of the domain. RANS equations are solved in the near-wall region while the LES equations are solved beyond. The DES modification in the SST RANS model is applied to the dissipation term in the equation for the turbulent kinetic energy (K). The equation shown below represents the standard SST RANS model.

$$\epsilon = \beta^* K\omega \tag{2.1}$$

In this equation, 'ϵ' is the dissipation rate, 'β^*' is a constant in the SST model and 'ω' is the specific rate of dissipation of turbulent kinetic energy. However, in a DES-SST formulation, the equation for the dissipation rate is replaced with the following:

$$\epsilon = F_{DES}\beta^* K\omega, F_{DES} = \max(\frac{L_t}{C_{DES}\Delta}, 1) \tag{2.2}$$

In these equations, Δ, given by $\Delta = \max\{\Delta x, \Delta y, \Delta z\}$, is the maximum local grid spacing, 'L_t' is the turbulent length scale given by $L_t = \frac{\sqrt{K}}{\beta^*\omega}$ and 'C_{DES}' is a model

constant. The comparison of DES and LES as observed by Serre et al. [1] with respect to the ability to accurately predict the vortical structures in the wake region of the Ahmed body can be observed in Figure 2.7.

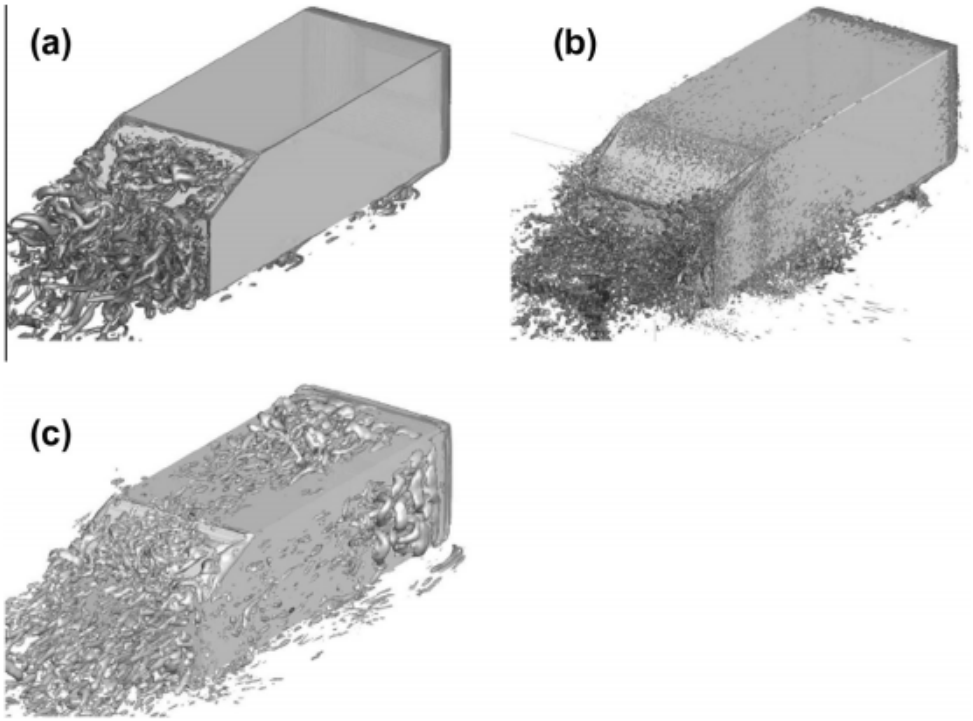

Figure 2.7: Comparison of the vortex structures visualised by iso-surfaces of the Q-criterion in the wake region of Ahmed body using (a)DES-SST (b)LES-NWR and (c)LES-SVV [1]

Guilmineau [26] studied the flow features around 25^o and 35^o Ahmed body configurations using a combination of RANS and DES-SST turbulence models. His DES models over-predicted the separation region over the slant and the coefficient of drag although they were able to slightly predict the occurrence of C-pillar vortices. The RANS models on the other hand were successfully able to predict the flow characteristics for the 35^o slant angle geometry with good accuracy. Despite this success, the RANS models failed to give acceptable results for the 25^o configuration due to the inability of the CFD solver to correctly predict the reattachment of the flow at the slant base of the Ahmed body. However, this study proved that RANS solvers are

fully capable in predicting flow structures accurately for sub-critical and super-critical Ahmed body configurations with the exception of the 25^o case.

Guilmineau et al. [27] presented further studies of the flow features around 25^o and 35^o Ahmed body configurations. In this study, they used four different numerical setups to model turbulence - Menter's $K-\omega$ SST RANS turbulence model, Explicit Algebraic Stress Model (EARSM) based on a $K-\omega$ model, DES-SST turbulence model, and an Improved Delay Detached Eddy Simulation (IDDES) hybrid RANS-LES turbulence model. As with their previous studies, a good co-relation was observed for 35^o Ahmed body models using all numerical setups. For the 25^o configuration, improvements were observed in the prediction of flow features, however, with the exception of the IDDES model, the prediction of the reattachment phenomenon still remained an obstacle.

2.2 Interaction of Multiple Vehicles

Although a plethora of both experimental and computational data related to aerodynamic optimization of isolated vehicle geometries is available in existing literature, very little is known about the complex aerodynamics involving vehicle interactions. While the costs and difficulties associated with experimental studies of such intricate vehicle interactions using realistic vehicle geometries are often times unreasonable, there is still some experimental data available that gives us an insight into such vehicle interactions. While studying vehicle interactions using Ahmed Bodies is the objective of this study, understanding vehicle interactions for simpler bluff bodies is essential.

In order to understand the aerodynamic interactions of a two body system, Martinuzzi et al. [7] conducted an experiment using two wall mounted cubes in tandem. It was observed that the flow pattern was greatly dependant on the longitudinal spacing between the two wall mounted cubes. While flow separation was observed at the leading body, the effects of this separation on the trailing body were highly de-

pendent on the longitudinal spacing between them. It was observed that for smaller distances of <1.4L ('L' being the length of the cubes), the flow that was separated at the leading body tends to reattach itself onto the trailing body. At 1.4L<longitudinal spacing<3.5L, a sharp rise in turbulence activities and vortical structures was noticed between the leading and trailing cube owing to the entrainment of flow off of the leading body. At longer distances, it was noticed that the separated flow from the leading body tends to reattach itself onto the trailing body in its upstream region as can be seen in Figure 2.8. Martinuzzi et al.'s results highlighted the potential benefits of vehicle platoons and helped gain a large understanding of multi-body interactions.

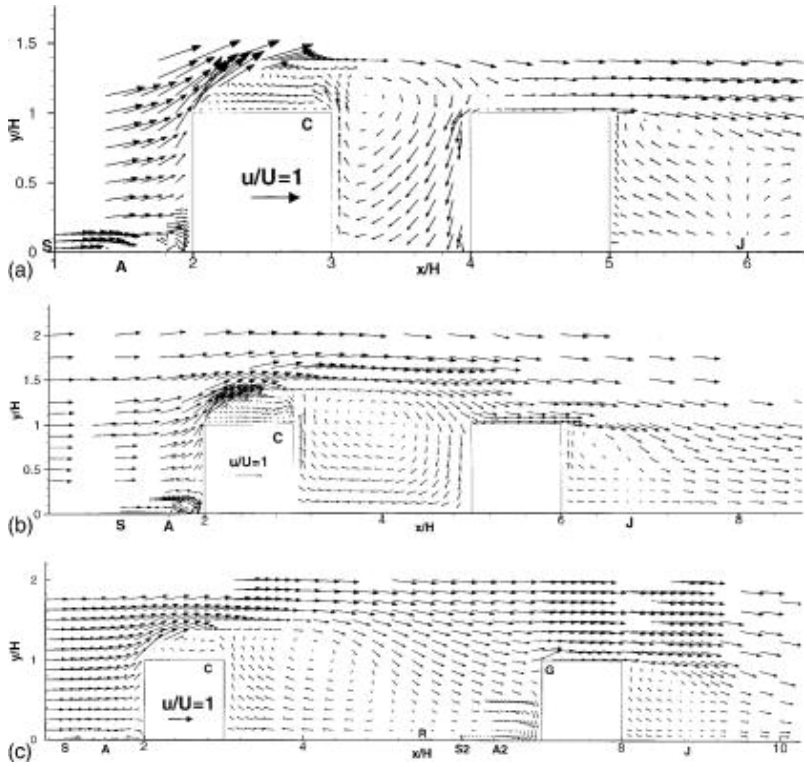

Figure 2.8: Vectorial representation of the mean velocity components for (a) $S/H = 1$; (b) $S/H = 2$; and (c) $S/H = 4$ respectively viewed on the symmetry plane [7]

Schito et al. [8] conducted both experimental and CFD platooning studies using Ahmed body geometries to validate the CFD results with that of the experimental data obtained. In their study, they also used simplified geometries of a compact car,

sedan, van, and a truck to study the aerodynamic interactions of various multi-vehicle configurations to analyze the influence of vehicle profile and relative longitudinal spacing between the vehicles. They observed that for vehicles with an estate back, such as an SUV or a station wagon, and trucks, a drag reduction of up to 50% can be achieved through vehicle platooning. On the contrary, they noticed that the fastback models, such as a sedan model, which have better performances when in an isolated scenario respond poorly without much reduction in drag when compared to estate models under platooning conditions. They also observed the change in drag for a truck as a trailing body when in a platoon with cars is negligible. However, cars experienced a heavy reduction in drag when trailing a truck. It was also concluded that two-box designs are likely to have more aerodynamic advantages compared to three-box designs in platooning conditions. The effects of multi-vehicle platooning on the coefficient of drag is shown in Figure 2.9.

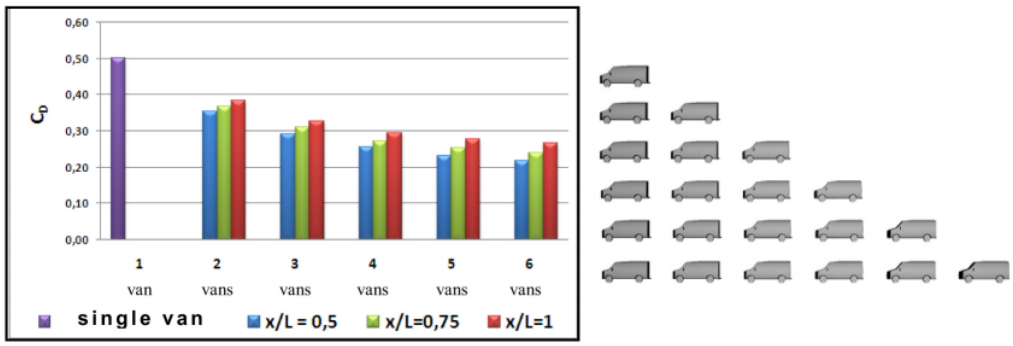

Figure 2.9: Effects of multi-vehicle platooning on the coefficient of drag as observed by Schito et al. [8]

The effects of longitudinal vehicle spacing on the aerodynamics of Ahmed Bodies were studied by Watkins et al. [9] experimentally at the RMIT Industrial Wind Tunnel, a closed jet wind tunnel with a stationary ground setup. In their study, Watkins et al. used used two co-linear 30^o Ahmed body geometries combined with a six-component internal force balance system to provide motion to the trailing body

(or the downstream model) in order to study vehicle interactions as one vehicle approaches the other. Data was extracted for aerodynamics properties of both vehicles and the respective wake regions for distances from x/L=0.1-4 ('L' being the length of the Ahmed body) downstream of the leading body. It was observed that as the trailing body moved from 4L downstream to 1L downstream, the drag of the trailing body fell below the value that it would be if in an isolated case as expected. However, as the trailing body moved further upstream from 1L to 0.1L, a significant rise in drag of up to 30% was observed. This sharp rise in drag of the trailing body at a smaller longitudinal spacing was attributed to the strong vortex system arising from the slant back of the leading vehicle which after separating impinges into the region at the rear of the vehicle instead of always reattaching itself near the wake thereby creating a low pressure, high momentum flow in the region between the two bodies. It was also observed that the decrease in drag for the leading body was always more pronounced compared to the increase in drag for the trailing body. Also, the trailing model wake did not appear to demonstrate a significant change in its structure from that of a model in isolation, insinuating that the unexpected rise in drag is at the front of the body. Watkins et al. also noted a significant reduction in drag of the leading vehicle as the proximity to the trailing body was increased. The lift coefficients of both the vehicles were also found to be highly sensitive to the vehicle spacing. These variations in lift and drag coefficients with respect to vehicle spacing can be seen in Figure 2.10. While Watkins et al. agree that their measurements using a fixed road setup can be compromised from the growth of the boundary layer on the tunnel floor, this study is a proof that despite being generally considered as a method for reducing drag, drafting can have significant drag penalties on trailing vehicles in a close proximity.

Pagliarella et al. [10] also experimentally studied the performance of vehicles in platooning conditions using both homogeneous and heterogeneous two-vehicle platoons at the RMIT Industrial Wind Tunnel. In their studies, they used a combination of

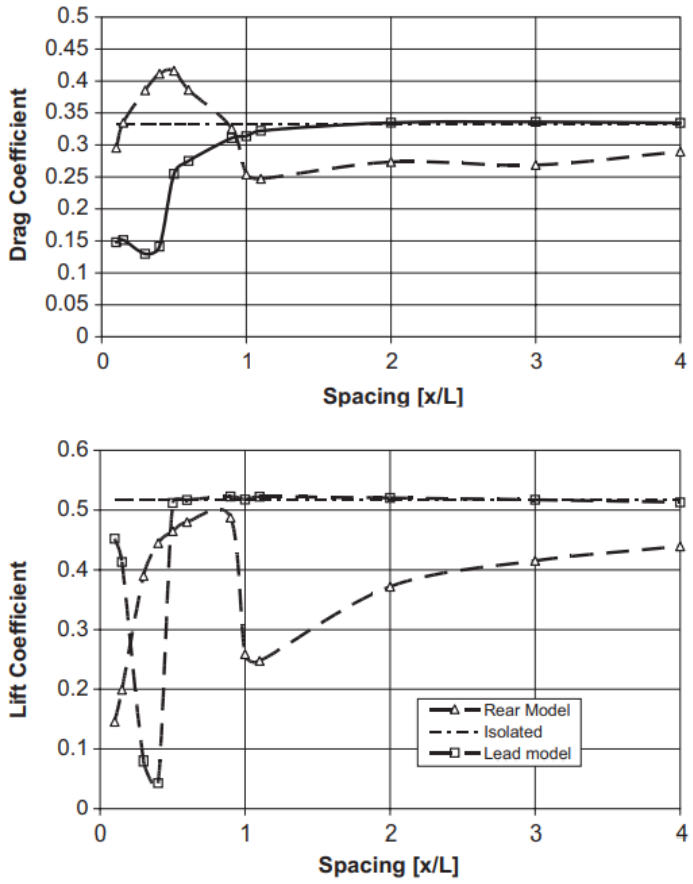

Figure 2.10: Effects of vehicle spacing of drag and lift coefficients [9]

25^o (sub-critical) and 35^o (super-critical) Ahmed body configurations to understand the effects of heterogeneity while running four tests, two of which were homogeneous using both sub-critical and super-critical Ahmed Bodies respectively while the rest were heterogeneous using a combination of both as the leading and trailing bodies. The net saving in drag for all the platooning conditions can be seen in Figure 2.11.

It was observed that the potential for increased aerodynamic performance by longitudinal platooning was negligible for any combination of sub and super-critical Ahmed body geometries beyond a longitudinal spacing of 2L which agrees with the conclusion that Watkins et al. [9] came to. It was also noticed that the net aerodynamic performance of the platoon was broadly dominated by the geometric configuration of the

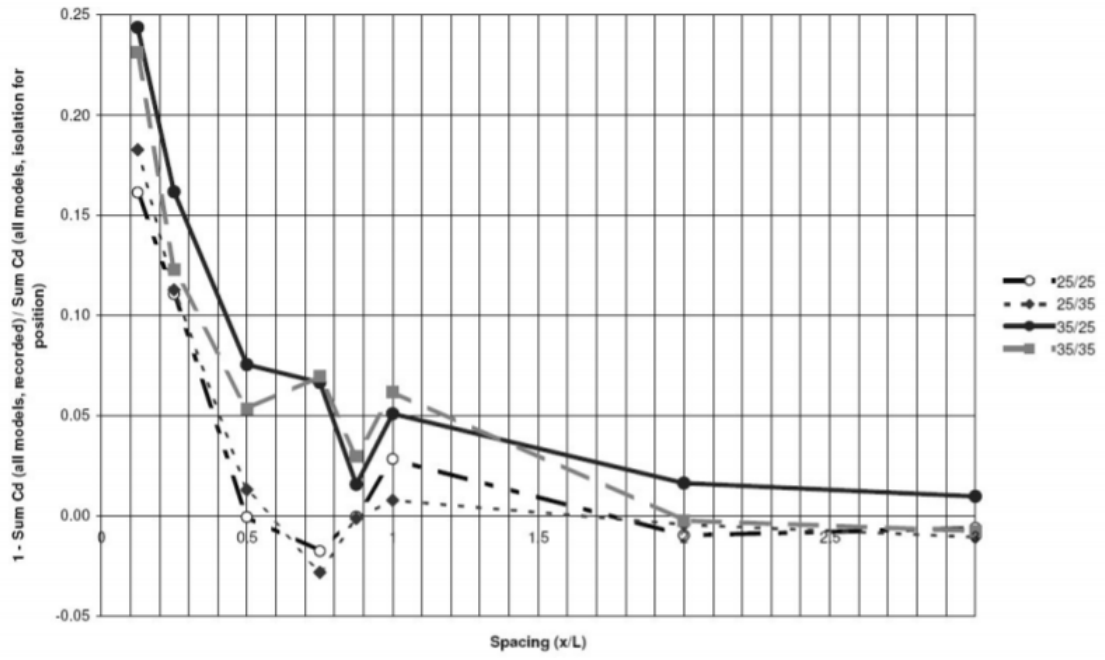

Figure 2.11: Net saving in drag in platooning configurations as observed by Pagliarella et al. [10]

leading model regardless of the heterogeneity of the two-vehicle platoon and whilst the trailing model performance for a given leading model showed minor differences at close proximity, the performance beyond such proximity was largely insensitive. Also, the most significant gain in performance of the platoon as a whole was realized when the super-critical Ahmed body model acted as the leading geometry in the platoon. The general behavior of the wake profiles of both the leading and trailing bodies individually also largely agree with the work of Watkins et al. [9]. While a significant net platoon drag reduction was observed at a spacing x/L$<$0.5, a sharp rise in drag of the trailing body was observed.

Humphreys et al. [11] performed CFD studies to analyze the platooning characteristics of a generic tractor-trailer geometry using RANS (Realizable K-ϵ or RKE) and DES models. The aim of this study was to characterize the fuel consumption of tractor-trailer models in terms of longitudinal spacing in a platooning condition and to

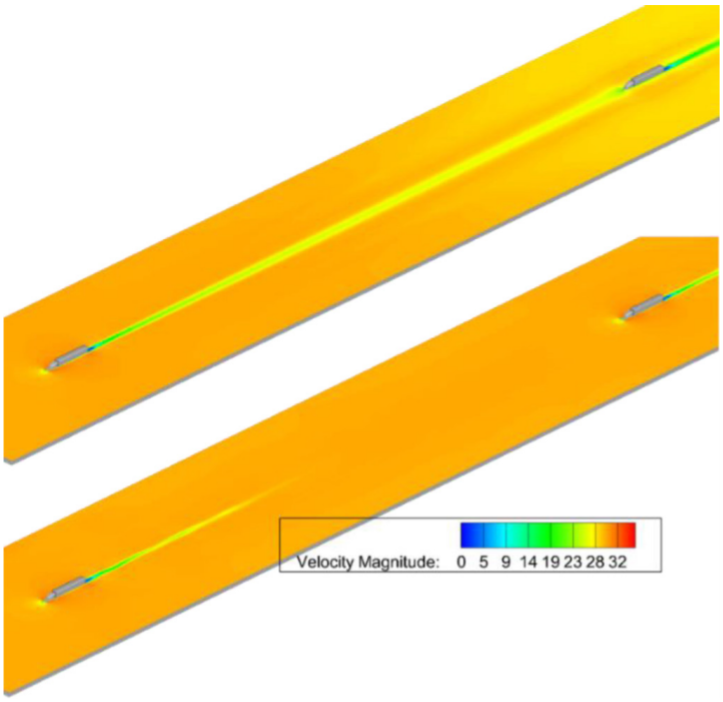

Figure 2.12: Differences in wake diffusion capabilities of RKE (top) and DES (bottom) over a large separation distance [11]

compare the performance of DES and RKE turbulence models. The major difference observed between the two turbulence models was in their ability to relaminarize flow in the wake regions of the two model. While in reality, the flow always relaminarizes with increase in distance due to the dissipation of turbulent kinetic energy, the RKE model failed to relaminarize the flow resulting in a wake that theoretically extends to infinity while the DES model was able to diffuse the wake. Figure 2.12 shows the difference in prediction capability of wake diffusion of RKE and DES model. The diffusion of wake is particularly important because the trailing model has a reduction in drag as long as it lies within the low pressure wake region behind the leading model. It was noted that even with the DES model, a reduction in drag was observed for the trailing body at extremely large separation distances while the gains when using RKE model extended towards infinity. Despite this inaccuracy, it was observed that

both RKE and DES had similar trends in prediction of wake profile and aerodynamic properties at smaller separation distances of less than x/L=4 from the rear of the leading model so much so that Humphreys et al. justified the usage of RKE for such proximities owing to decreased computational resources as the overall behavior of the drag reduction trend with respect to the separation distance was similar to the more robust, transient, higher order solution over a range of practical operation separation distance.

2.3 Overtaking Maneuver

While vehicle interactions under platooning conditions are an extremely valuable source of information, they differ extensively compared to the more interesting and intricate wake interactions as observed in an actual overtaking maneuver between two vehicles. Experimental studies concerning overtaking maneuvers have continuously proven to be extremely inconvenient, expensive, and complex owing to the difficulties in measurement techniques for a body in motion while the other is stationary. Studying such a setting is also computationally expensive as compared to the study of an isolated body or even a platooning condition. Not only are vehicle interactions sensitive to longitudinal spacing, but also to the lateral spacing between two vehicles, the effects of which this endeavour is aiming to study. Despite the setbacks in understanding such an interaction, there have been a few studies, both experimental and CFD, that have provided a glimpse into the aerodynamics associated with overtaking maneuvers some of which are discussed below.

One of the earliest studies of overtaking maneuvers was conducted by Dominy [12] in 1990. Although in his wind tunnel experiment, there was no actual overtaking, Dominy studied the advantages of slipstreaming using quarter scale open wheel Grand Prix racing cars to understand how much of an advantage it can have leading to an overtaking maneuver. The experiment was conducted at the Imperial College London rolling road wind tunnel (the experimental setup of which can be seen in Figure 2.13).

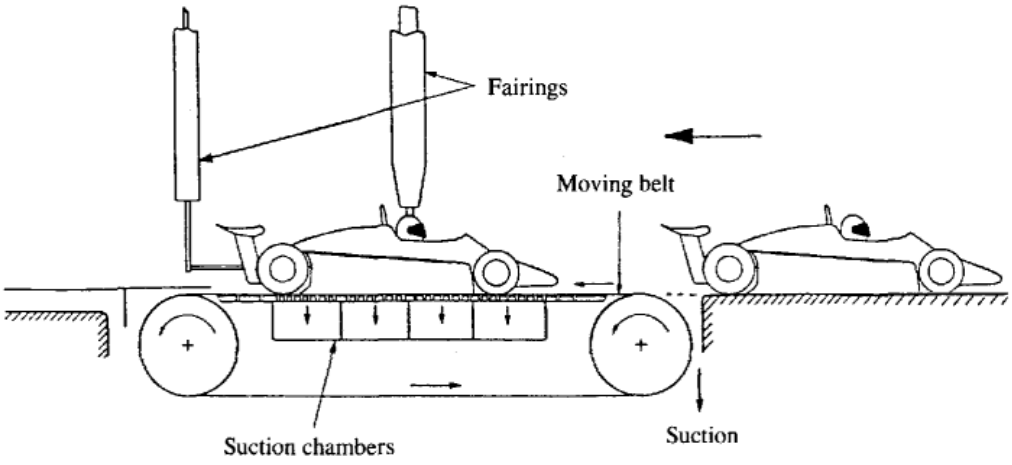

Figure 2.13: Experimental setup of Dominy et al. [12]

It was observed that the trailing car experienced a loss in downforce by 36% and a gain in drag by 23% thereby giving it a higher chance to overtake the leading vehicle in a straight line. It was also observed that if an offset was introduced in the axis of the trailing car, some of the downforce lost was getting recovered and the recovery continued with the increase in offset until a limiting point was reached at which the trailing car was in a completely undisturbed flow. Dominy's results provide us with a basic understanding of the sensitivity of lateral spacing in an overtaking phenomenon and vehicle interactions in general.

In 1997, Yamamoto et al. [17] experimentally studied the aerodynamic influence of large overtaking vehicles (such as a bus) on the motion stability of other smaller vehicles (such as passenger cars) using several quasi-static analyses conducted at discrete predetermined positions. When comparing their test results with actual car tests, Yamamoto et al. noted that the interference phenomenon can be treated as a quasi-static problem when the relative velocity between both the bodies is small. However, it was also found that relative speed between the two bodies can have a very large influence on the motion stability of the body being overtaken especially if the relative speed is small in which case the acting time of the aerodynamic force

becomes long.

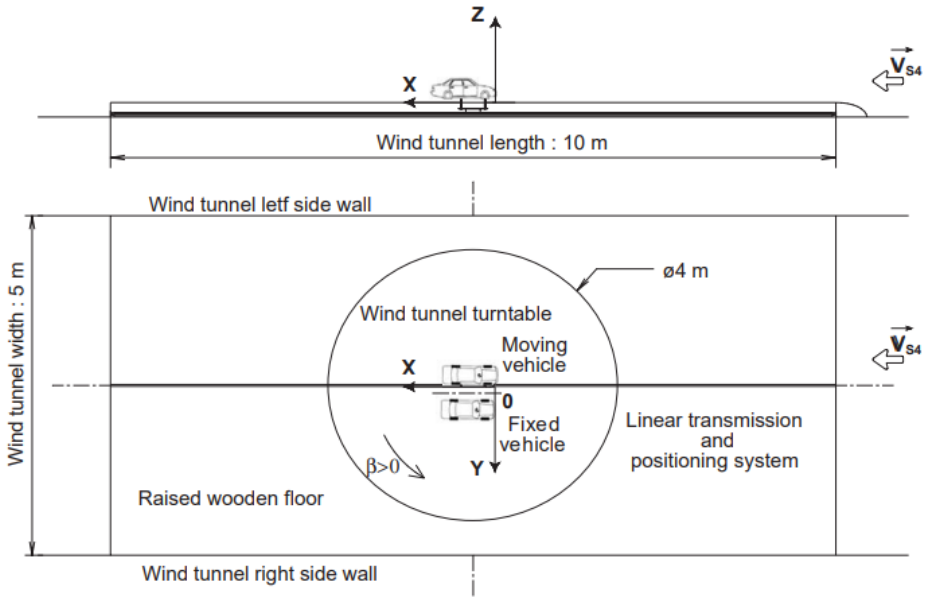

Figure 2.14: Experimental setup of Noger et al. [13]

Following Yamamoto's studies, Noger [13], [18], [19] conducted several experimental studies of an overtaking maneuver using $1/5^{th}$ passenger scale model cars with both quasi-static and dynamic conditions at the wind tunnels of Institut Aerotechnique of Saint-Cyrl'Ecole. In their first study, it was determined that the transient forces acting on bodies in an overtaking maneuver are a function of three independent factors - longitudinal spacing, lateral spacing, and the relative velocity between the two vehicles. The experimental setup in their tests allowed for varying several factors such as longitudinal and lateral spacing, yaw angles, inlet or wind tunnel velocities, and the relative velocity between the two bodies.

In their several experiments, it was observed that as both longitudinal and lateral spacing, individually or simultaneously, decreased, there is a sharp rise in aerodynamic interactions between both the bodies as largely agreed by Yamamoto's [17] results. This is evidenced by the changes in drag, downforce, side force, and the moment coefficient values of both bodies as shown in Figure 2.15. From the plot, it can be

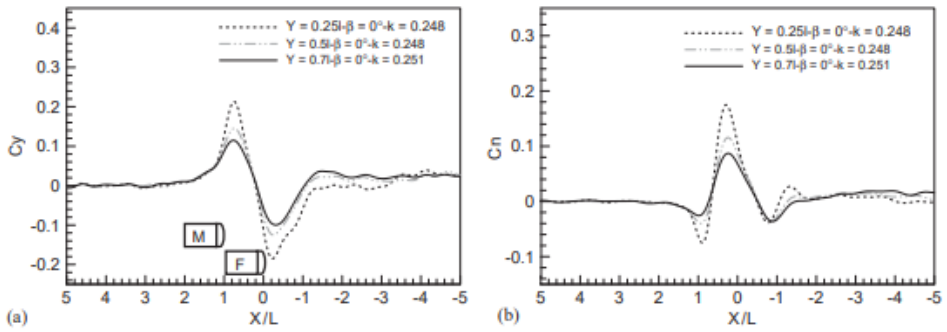

Figure 2.15: Effects of transverse spacing on (a) side force co-effieicnt and (b) yawing moment coefficient for the overtaken vehicle as observed by Noger et al. [13]

seen that the side force coefficient of the overtaken body reaches a minimum right before the overtaking body is parallel to it and reaches a maximum when the low pressure region at the rear of the overtaking body is right next to the high pressure region at the front of the overtaken body. It is also interesting to note that the location of peaks of the forces remained at the same position while their magnitude differed considerably with varying lateral spacing. The effects of varying relative velocity, however, on the coefficients of side force and yawing moment were very small as can be seen in Figure 2.16.

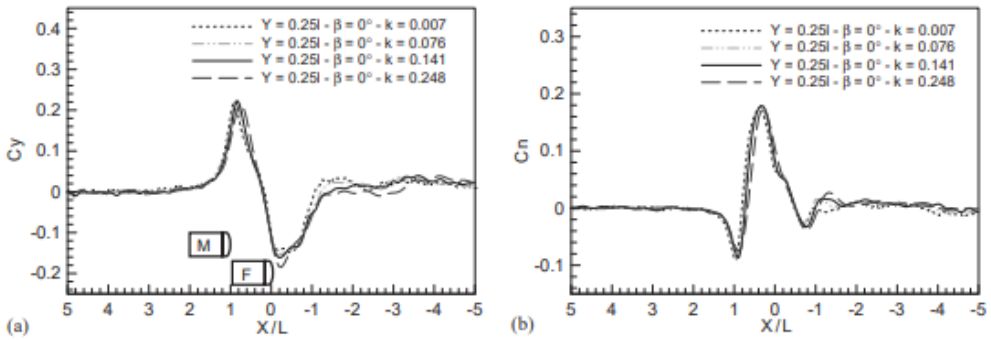

Figure 2.16: Effects of varying relative velocity (a) side force co-effieicnt and (b) yawing moment coefficient for the overtaken vehicle as observed by Noger et al. [13]

An other important observation was made on the effects of crosswind on the aero-

dynamic coefficients and it was observed that the presence crosswinds had nearly no effect on both the overtake and overtaking vehicles respectively as long as the crosswind angle remained relatively small.

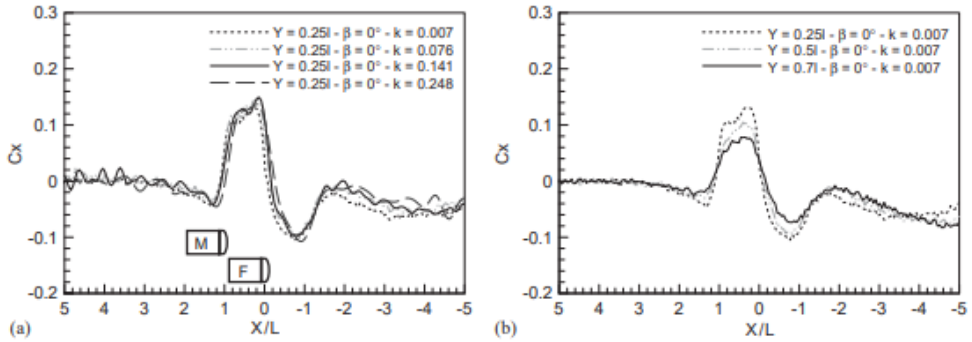

Figure 2.17: Effects of relative velocity and lateral spacing on the change in coefficient of drag of the overtaken vehicle as observed by Noger et al. [13]

Figure 2.17 shows the effects of longitudinal and lateral spacing on the change in drag coefficient of the overtaken body. It can be seen that the drag coefficient value drops to a minimum when the front of the overtaking vehicle is in line with the rear of the overtaken vehicle. This is due to the interaction between the high pressure region at the front of the overtaking vehicle and the low pressure region at the rear of the overtaken vehicle. Beyond this point, the value starts rising rapidly until it reaches a maximum value right when both the vehicles are parallel to each other. After this, the second minimum is reached at a point when the front end of the overtaken vehicle is in line with the rear end of the overtaking vehicle beyond which, the value started to rise again. It was also noted that the wake due to the passing maneuver still effected the overtaken vehicle even when the overtaking vehicle was far ahead of the vehicle being overtaken thereby unable to fully recover the drag coefficient value of a single vehicle.

Following this study, Gillerion and Noger [14] conducted a number of quasi-static steady simulations at several discrete locations using the same experimental setup to

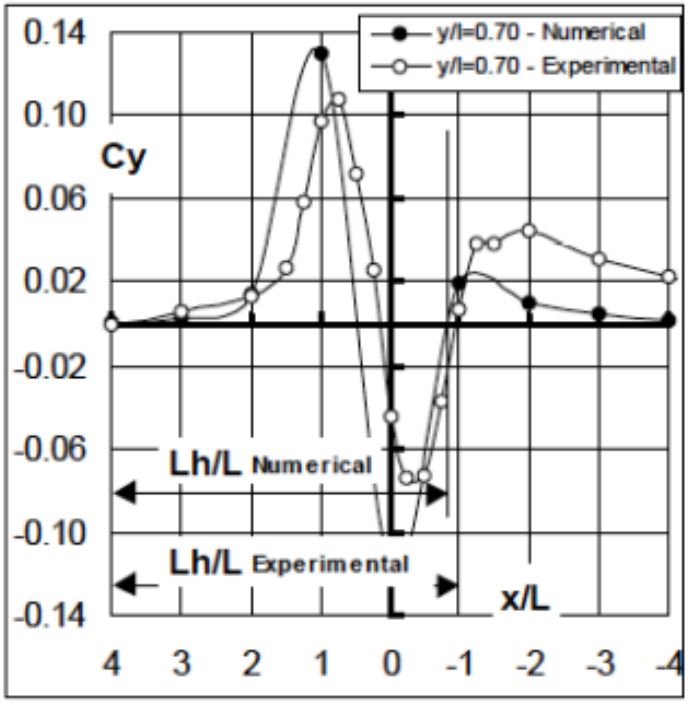

Figure 2.18: Differences in transient experimental data and quasi-static CFD data for the coefficient of side force as observed by Gillerion et al. [14]

compare against the data generated using CFD using two Ahmed body geometries. Both the experiment and CFD were conducted at a free stream inlet velocity of 30 m/s with a relative velocity of 10 m/s given to the passing body and a $K-\omega$ turbulence model was used. Upon comparing the plots of both the transient experimental and quasi-static simulation data, it was observed that while the quasi-static simulation was able to accurately predict the behavior of side force coefficient and yawing moment coefficient, it was unable to account for the transient effects observed experimentally as can be seen in Figure 2.18. The authors also analyzed the transient phenomena in their experiment with an approach based on the presence of pseudo-harmonic variations of the aerodynamic coefficients and presented values of Strouhal numbers associated. The variations of the transient aerodynamic characteristics were analyzed with the assumption of a pseudo-harmonic variation with a time period of $T = L_h/V_r$

or a frequency of $f = V_r/L_h$ where 'V_r' is the relative velocity and between both vehicles and 'L_h' is the length of travel of the overtaking body. A Strouhal number was then calculated with the formula given below, which is a value that has a significant importance at a later point in this thesis.

$$S = \frac{fL}{V_r} \tag{2.3}$$

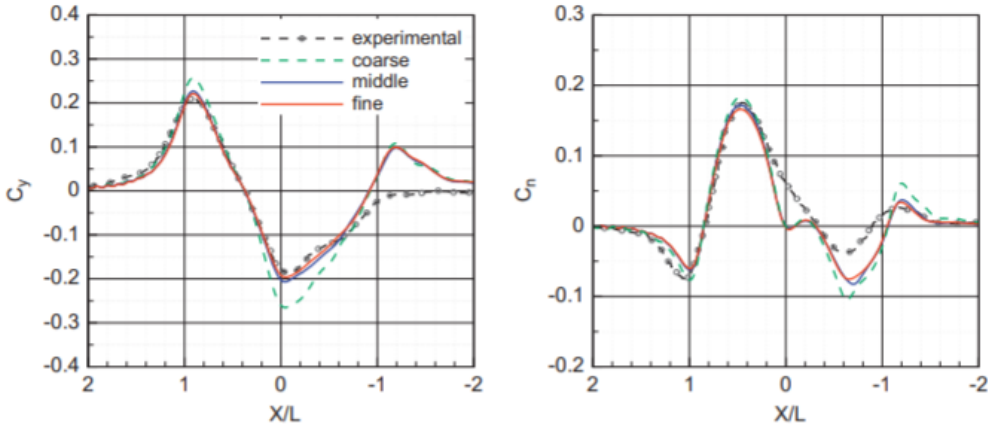

Figure 2.19: Comparison of CFD and experimental data for different mesh resolutions for side force co-effieicnt (left) and yawing moment coefficient (right) of overtaken body as observed by Uystepruyst et al. [15]

More recently, Uystepruyst et al. [15] conducted several transient three dimensional Unsteady Reynolds-Averaged NavierâStokes (URANS) CFD simulations wherein the relative motion between the two vehicles was provided by a combination of deforming and sliding computational grids to measure the aerodynamic components on a scaled 30^o degree slant angled Ahmed body. In their analysis, the aerodynamic influence of a passing maneuver on the overtaken body were studied using RANS equations coupled with an eddy viscosity $\zeta - f$ model equations proposed by Hanjalic et al. [28].The accuracy of the results and their turbulence model were validated with existing experimental data (as can be seen in Figure 2.19) until a suitable mesh was obtained. As the computational domain used by Uystepruyst et al. was significantly larger than

in any previous CFD studies, it allowed for a better resolution thereby allowing more accurate results. Several simulations were run for varying values of relative velocities and compared to the existing literature following the agreement of which, simulations were run for various values of free-stream velocities. A dimensionless coefficient 'k' was defined as the ratio of relative velocity to free-stream velocity ($k = V_r/V_o$) and effects of varying 'k' on the aerodynamic coefficients were studied and compared to the existing data by Gillerion et al. [14].

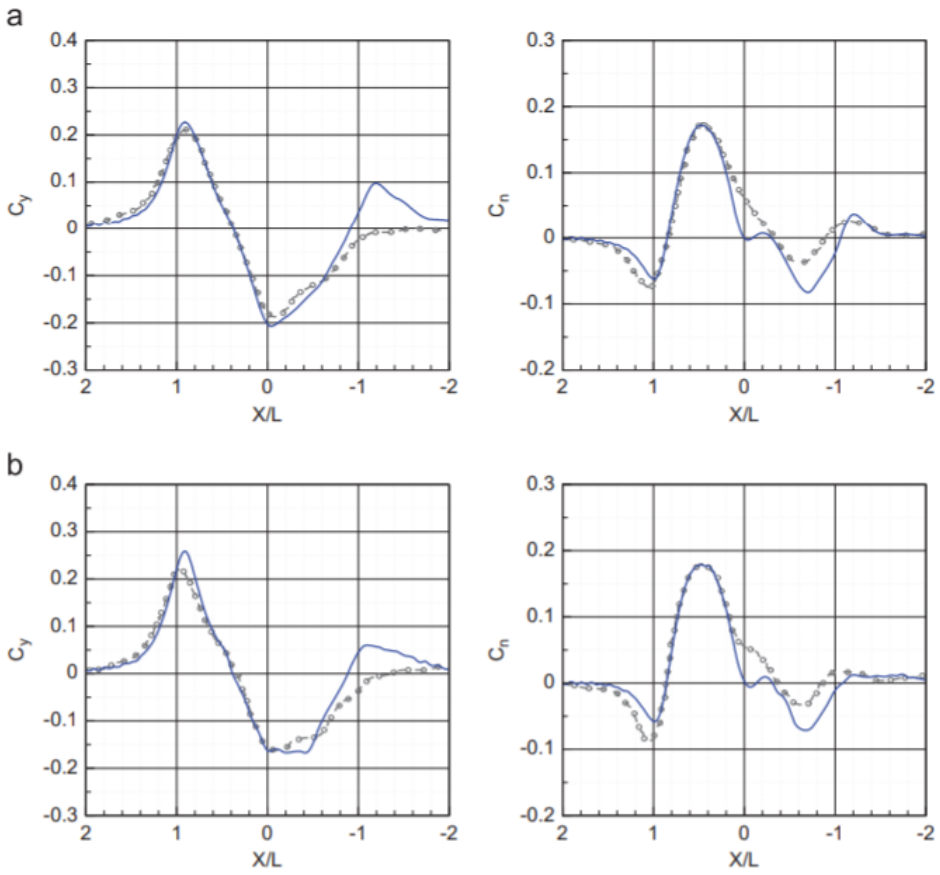

Figure 2.20: Effects of varying relative velocity on the side force coefficient (left) and yawing moment coefficient (right) of the overtaken body with (a) $k = 0.248$, and (b) $k = 0.141$ for experimental data (solid line) and CFD data (dotted line) as observed by Uystepruyst et al. [15]

Figure 2.20 shows the effects of varying relative velocity on the side force coefficient and the yawing moment coefficient of the overtaken body for different values

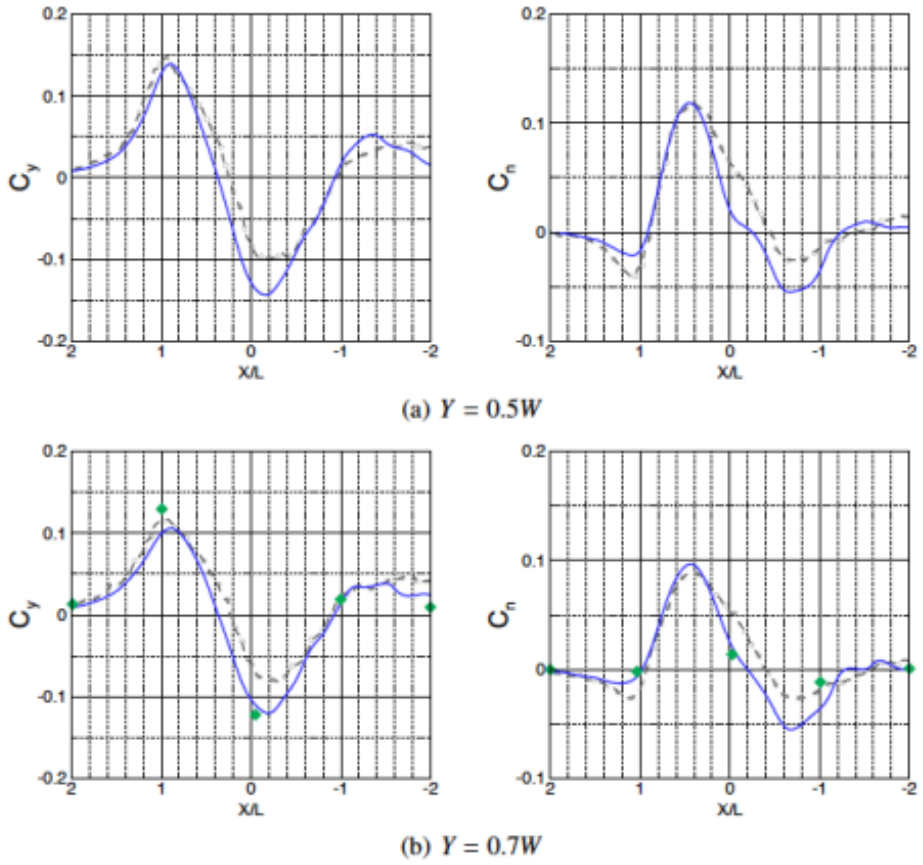

Figure 2.21: Effects of lateral spacing on the side force coefficient and yawing moment coefficient of the overtaken body as observed by Uystepruyst et al. [15]

of the dimensionless coefficient 'k' comparing the results of both CFD and existing experimental data. In their study, the coefficients of side force and yawing moment decreased with increase in relative velocity which is different to Noger's [13], [19] conclusion where the aerodynamic coefficients were independent of relative velocity. However, these results go hand in hand with Corin et al.'s [20] results where it was found that while the drag coefficient increased with increase in relative velocity, side force coefficient decreased for the same. Uystepruyst et al. also studied the effects of lateral spacing on the aerodynamic coefficients of the overtaken body during a passing

maneuver (Figure 2.21). It was noticed that the effects of the passing maneuver on the drag coefficient decreased with increase in lateral spacing. When the front of the overtaking body was in line with the rear of the body being overtaken, a maximum was observed due to the interaction of the high pressure region in front of the overtaking body and the low pressure region at the rear of the overtaken body. This was also the point at which side force coefficient of the overtaken body reached a maximum. As the overtaking body slowly moved forward, the drag coefficient kept decreasing and when the overtaking body was in line with the overtaken body, a minimum was observed. Beyond this point, the drag coefficient started to slowly rise again to its original value until the rear of the overtaking body was in line with the front of the overtaken body. These simulations were a major breakthrough and proved that three dimensional multi-vehicle transient simulations are possible in CFD.

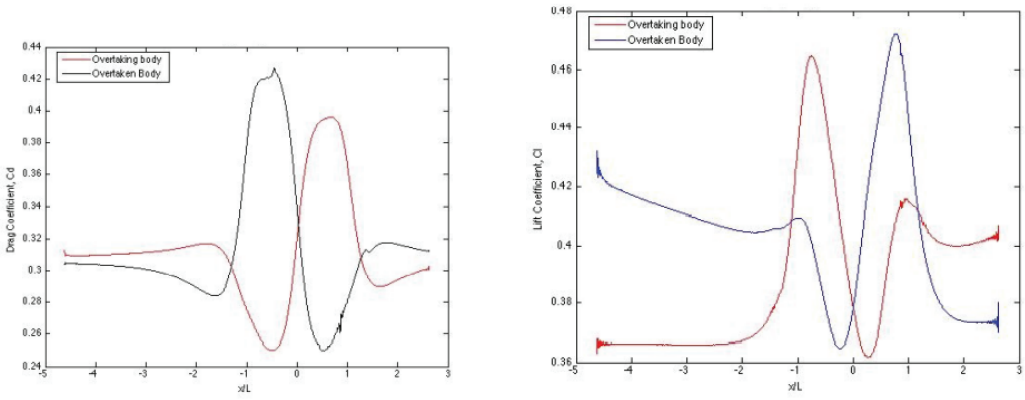

Figure 2.22: The behavior of drag coefficient and lift coefficient of both overtaking and overtaken bodies as observed by Uddin et al. [16]

Uddin et al. [16] conducted a CFD study using two Ahmed body geometries tandem to understand the transient effects in an overtaking maneuver. In their study, they developed a new meshing methodology, called the overset mesh model, using which relative motion was provided to one Ahmed body model in the longitudinal direction while keeping the other model stationary in a virtual wind tunnel using an

unsteady Reynolds Averaged Navier-Stokes (URANS) turbulence model. The overset mesh model was validated by comparing the trends of aerodynamic coefficients with existing experimental and CFD data from Noger's and Gillerion's studies and a good correlation was observed between their results and the existing literature thereby suggesting that their simulation methodology is fully capable of investigating multi-vehicle transient interactions such as an overtaking maneuver. Figure 2.22 shows the trend of drag and lift coefficients of both overtaking and vehicle being overtaken as observed by Uddin et al. in their study using overset meshing technique.

To this day, the several experimental studies conducted by Noger and Gillerion [13], [19], [18], [14] on overtaking maneuvers remains as one of the largest sources of literature for studies in this field. The plethora of experimental data provided from their studies stands as a benchmark against which modern numerical and CFD data can be compared to. Their studies are also significant in highlighting the differences in transient and quasi-static modeling of experiments and simulations, and portray the need for more efficient transient state simulations in understanding an overtaking maneuver, and largely multiple-vehicle interactions in general. The results from the sliding mesh simulations by Noger and Gillerion were used as a benchmark and a clear understanding of the behavior of the aerodynamic coefficients from their literature along with the results from Uddin's [16] study provided for the development and validation of the overset meshing technique used in this study.

2.4 Overset Mesh

An overset mesh (also known as a Chimera mesh or an overlapping mesh) is a meshing technique that allows modelling intricate motions in CFD simulations. It was first used by NASA in 1988 to model and understand the transient behavior of the Integrated Space Shuttle Launch Vehicle (or SSLV). While a small grid of less than one million cells was tested, the grid took nearly an year to generate due to the lack of infrastructure and computational power combined with the absence of

purpose-built tools to generate the mesh. In modern day however, there are several tools and packages that are easily available which have the power to generate complex overset grids making it easier to understand and analyze the transient behavior in CFD simulations.

An overset mesh contains a background region and overset region(s) that are meshed independently according to user needs and then attached together to couple the equations solved in each region to obtain a universal solution [29]. It is an important tool in CFD to study moving objects as independent meshes allow for unrestrained motion of objects with respect to each other. The major advantages of using an overset meshing technique are as follows:

- Transient simulations that include multiple moving components can be easily modelled by moving the independent meshes along with objects in consideration as the solution is automatically re-integrated at each time step. This setup enables to maintain local refinements and boundary layers around the moving objects without the need to refine the whole computational domain.

- It provides flexibility as multiple components can be meshed independently thereby giving the user more control over generating a grid.

- Greater control over local mesh refinement wherever necessary.

Despite its ability in enabling the study of transient simulations, overset mesh or Chimera mesh does have a couple of drawbacks. To smoothly transition information to and from the overset region and the background region, the cell sizes in the overlap region have to be in the same order of magnitude. Also, while simulating moving objects, the movement is restricted to a single cell per time step. However, modern software packages such as STAR-CCM+ are more than capable to handle these drawbacks with minimal user input. The overset mesh setup developed by the author for this study is an adaptation of the model developed by Chellaram [21].

CHAPTER 3: NUMERICAL SETUP

This chapter details the numerical setup for each simulation encompassed within this study and elucidates the boundary conditions chosen, and the mesh and physics setup of all the simulations. The numerical setup was developed and refined with the help of existing literature and all the knowledge gained by successive testing and validation of the results. Due to the availability of a vast amount of studies and data, an Ahmed body geometry was chosen as a test model for this undertaking. Ahmed body models with various slant angles were created in PTC Creo Parametric 7.0.0.0 (with the same dimensions as in Figure 2.1) before imported into Simcenter STAR-CCM+ 19.03 (Build 14.06.012), a commercial finite volume CFD solver.

Once the Ahmed body geometry was imported into the CFD solver, a virtual wind tunnel of dimensions $50L \times 30L \times 25L$ was created around it such that the lead car was placed at 10L from the inlet with the overtaking car 4.5L further downstream from the lead car. A total of 15 overset simulations were run (5 homogeneous and 10 heterogeneous) each at lateral/traverse spacing of 0.10W*, 0.25W*, 0.5W*, 0.75W*, and 1.0W* respectively where $W^* = y/W$ where 'W' is the width of the Ahmed body. A 35^o Ahmed body was used in the homogeneous simulations while both 35^o and 25^o Ahmed bodies were used in the heterogeneous configurations respectively. Prior to simulating the overtaking phenomenon, single body simulations were run with both 25^o and 35^o Ahmed bodies and results were compared with the existing experimental data to validate the numerical setup.

3.1 Mesh and Solver Setup

Meshing is essentially the discretization of the domain into smaller components. The finer the mesh, i.e., the smaller the size of the components (called cells) that encompass the domain, the higher is the fidelity of the simulations, and higher are the computational resources required to run the simulation. Mesh generation plays a crucial role in the accuracy of the computational results.

To study the dependency of the accuracy of the results on the mesh setup, a mesh sensitivity study was first conducted by temporarily removed the overtaking body. The results from this study were compared with the existing experimental by Strachan [23] until a suitable mesh setup was found. To make sure the CFD is comparable with experimental data, an inlet velocity of 25 m/s was chosen which corresponds to a Reynolds number of 1.6E6. A trimmed cell mesher was used to generate the volume mesh due to its ability to refine cells in the wake region along with a surface remesher and a prism layer mesher, and automatic surface repair was turned on to ensure no errors are generated during meshing. Surface controls were added to the vehicle geometries to adequately capture the boundary layer and several volumetric controls were implemented in the regions of interest to properly capture the wake region and the interaction between the two vehicle geometries. Four volume sources were used near the Ahmed bodies to ensure the resolving of flow near the surface also making sure the closest cell size was smaller than Taylor microscale which was calculated by using the formula in Equation (3.1) where 'L' is the length scale, 'Re' is the Reynolds number, and 'A_1' is an undetermined constant set to 0.5.

$$\lambda = \sqrt{15}\frac{1}{\sqrt{A_1}}\frac{1}{\sqrt{Re}}L \tag{3.1}$$

To ensure a y^+ value of less than 0.5 (Figure 3.1) across all the surfaces of the Ahmed body, a prism layer near wall thickness of 0.008 mm was used along with

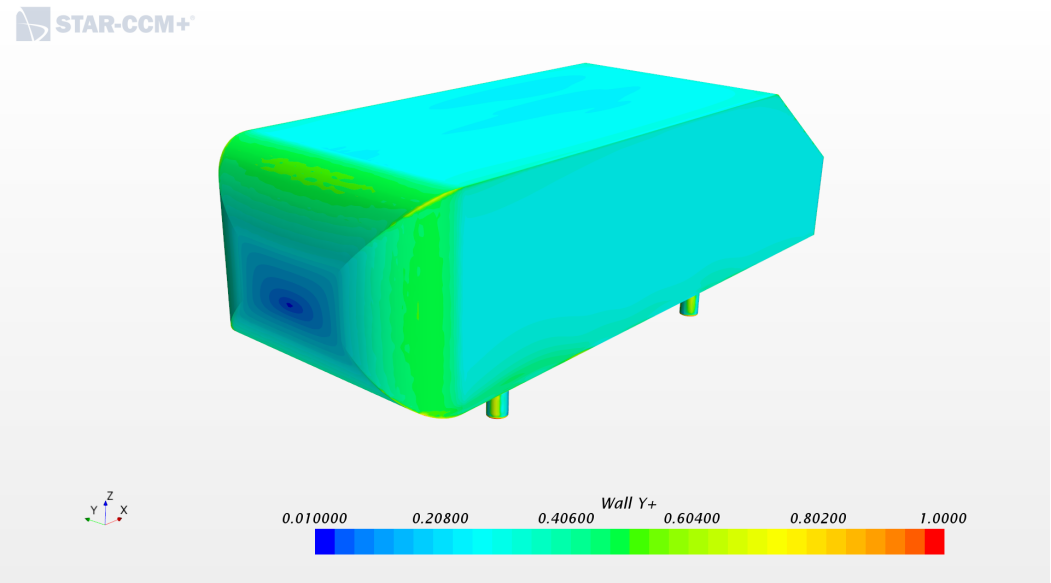

Figure 3.1: y^+ distribution on the 35^o Ahmed body model

32 prism layers with the prism layer total thickness set to 10 mm which resulted in a stretch factor of nearly 16%. The prism layer distribution along the front curved face, and along the top and slant edge can be seen in Figures 3.2 and 3.3 respectively. Figures 3.4 and 3.5 show the mesh structure around the Ahmed body.

Tables 3.1 and 3.2 show the variation of drag and lift coefficients of 25^o and 35^o Ahmed bodies respectively with respect to change in base size of cells and the percentage error compared to experimental data from Strachan [23]. Although using a base size of 4 mm resulted in more accurate value of drag coefficient, 8 mm was chosen as the base size to run overset simulations as the advantage of using 4 mm base size was minimal especially with the wake structures being very alike for both 4 mm and 8 mm cases respectively compared to the computational expenses that were required to run the simulations. A relatively large under-prediction of lift coefficient can observed for the 25^o Ahmed body geometry. This is due to the inability of RANS model to correctly predict the reattachment of flow on the rear slant edge of the geometry. RANS models are known to have a tendency to under predict the Turbulent Kinetic

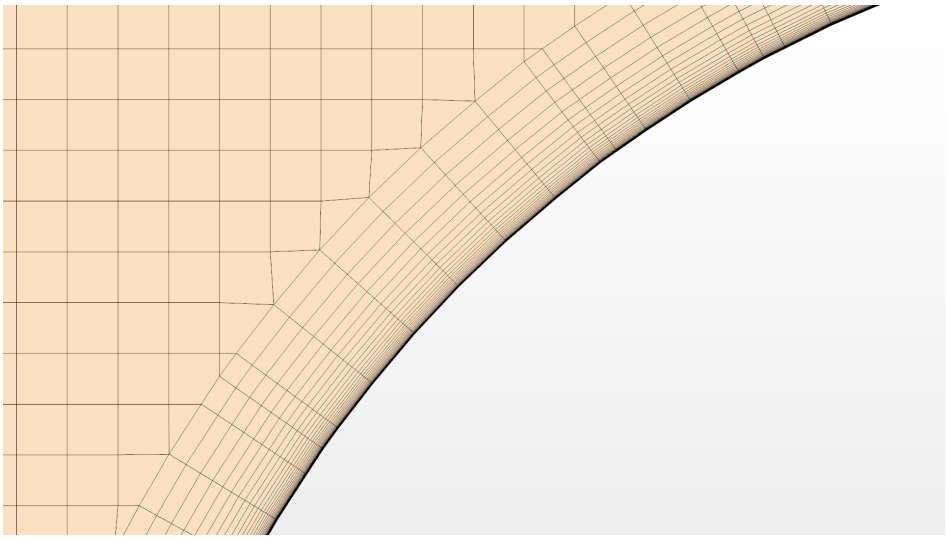

Figure 3.2: Prism layer distribution along the front face on the 35^o Ahmed body model

Energy (TKE) over the slant edge which leads to an over prediction of the separation bubble over the length of the slant edge and into the wake region. The predictions obtained from this study match with the CFD data of Guilmineau who has studied this phenomenon extensively [26].

Table 3.1: Mesh Independence of Cd for 25^o Ahmed body model

Base size (mm)	Total number of cells (in millions)	Cd	Cd% Error	Cl	Cl% Error
16	21.63	0.312	4.34	0.321	13.42
12	33.56	0.286	-4.34	0.025	-91.16
8	42.48	0.296	-1.00	0.096	-66.07
4	65.84	0.297	-0.67	0.097	-65.72

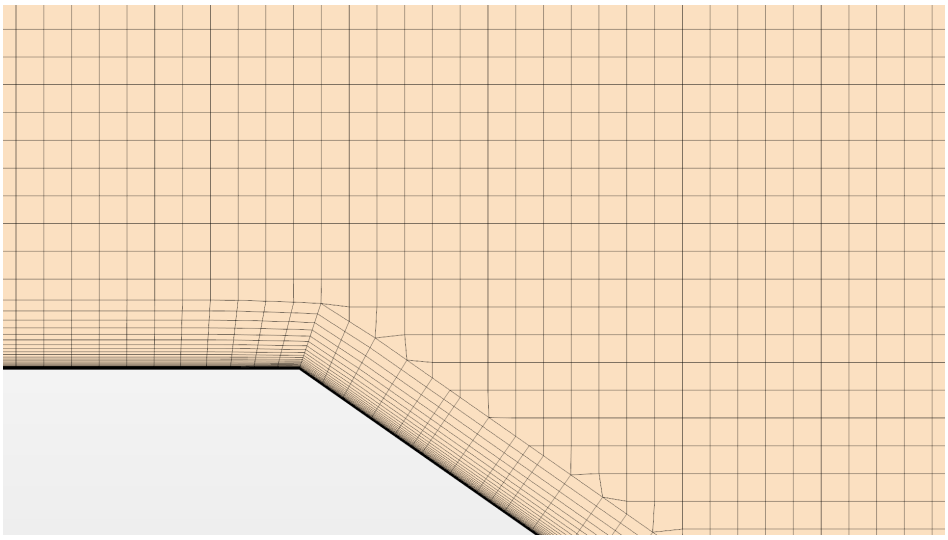

Figure 3.3: Prism layer distribution along the slant edge on the 35^o Ahmed body model

Table 3.2: Mesh Independence of Cd for 35^o Ahmed body model

Base size (mm)	Total number of cells (in millions)	Cd	Cd% Error	Cl	Cl% Error
16	21.86	0.257	-6.54	-0.031	-42.59
12	33.91	0.265	-5.09	-0.039	-27.77
8	43.37	0.278	1.09	-0.061	12.96
4	66.72	0.276	0.36	-0.053	-1.85

The final mesh parameters used in the simulation can be seen in Table 3.3. The same mesh setup was used to run overset simulations which resulted in a total cell count between 51-55 million cells for all 15 simulations. For the overset mesh, a block of dimensions $2L \times 1W \times 0.5L$ was created to be placed around the overtaking body such that the lower surface of the block coincides with the ground of the wind tunnel. This entire block with the overtaking Ahmed body would constitute of the overset region and the overtaking vehicle was given the same mesh parameters as the overtaken body to ensure an accurate solution. At this point, an interface was created

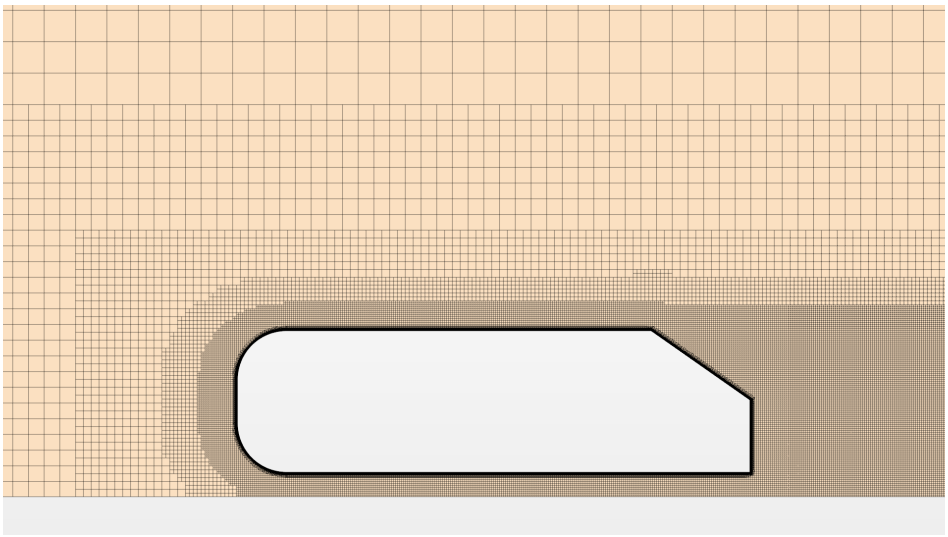

Figure 3.4: Close up view of the mesh along the side profile of the 35^o Ahmed body model

between the overset region and the background region to ensure a clear solution.

Table 3.3: Final mesh parameters used in the simulations

Mesh Parameters	Value
Base Size	8mm
Smallest cell size	4mm
No. of Prism Layers	32
Prism layer Near Wall thickness	0.008mm
Prism layer Total thickness	10mm

Baseline simulations using a single body were run with an unsteady solver with a time step of 0.001s with 4 inner iterations for a period of 3 seconds. Convergence was observed at the 2 second mark and no change in the residuals was observed at this point in this cycle. At the 3 second mark, several time steps were considered and a CFL independence study was conducted at several CFL numbers after which, a final time step of 4E-4 was chosen along with 8 inner iterations using which the simulations were run for 2 more seconds. For the overset simulations, the simulations

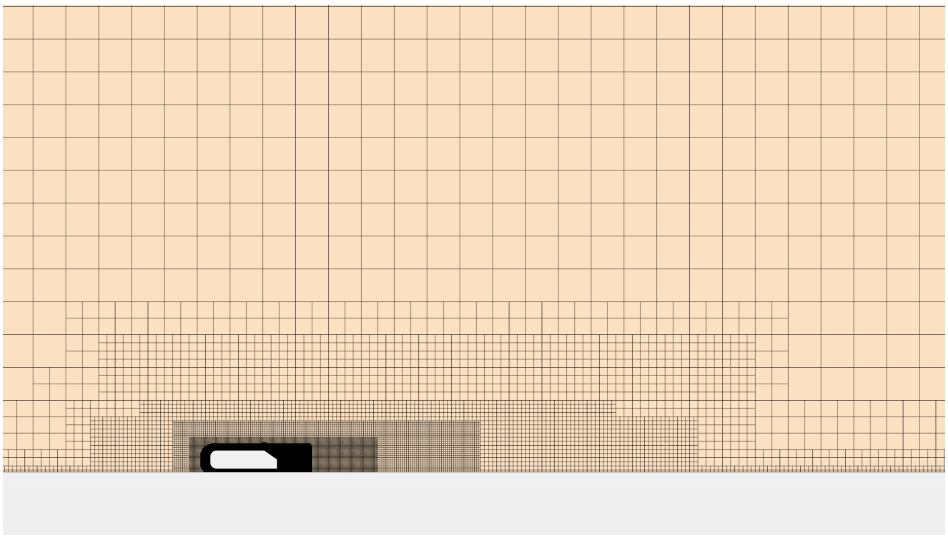

Figure 3.5: Zoomed out view of the mesh along the side profile of the 35^o Ahmed body model

were initialized with a time step of 0.001 seconds with 4 inner iterations for 2 seconds until convergence was observed at which point, the simulations were run for an other 2.7144 seconds with a time step of 4E-4 and 8 inner iterations thereby bringing the total simulation time to 4.7144 seconds for each overset simulation. This time step resulted in a CFL number of 2.5. The overset simulations were run on a CPU with 144 cores with 8 GB per core and an approximate computer wall time of 4 days.

3.2 Physics Setup and Boundary Conditions

An unsteady Reynolds Averaged Navier-Stokes (URANS) solver was used for this study to analyze the transient behavior of the wake structures during an overtaking maneuver for all simulations with an initial free-stream velocity of 25 m/s, a constant air density of 1.2 kg/m^3, and a dynamic viscosity of 1.855E-5 Pa-s which resulted in a Reynolds number of 1.6E6 matching that of Strachan's experimental data [23]. For the overset region, a relative velocity of 10% (2.5 m/s) of the free-stream velocity was given after initialization. The following physics continua were selected:

- Space: Three dimensional flow

- Equation of state: Constant density
- Solver: Implicit unsteady
- Flow type: Segregated flow
- Material: Gas
- Viscous regime: Turbulent
- Turbulence model: SST $K-\omega$
- Wall distance: Exact wall distance
- y^+ treatment: All y^+ treatment
- Other: Overset conservation, cell quality remediation, and solution interpolation

Menter's SST $K-\omega$ turbulence model [30] is essentially a modified version of the two-equation $K-\omega$ model that combines Wilcox's $K-\omega$ model [31] and the $K-\epsilon$ model [32]. At the boundaries it uses the $K-\omega$ model thereby taking advantage of its robustness and its ability to predict near wall flow characteristics for even adverse pressure gradients with very low y^+ values; away from the walls, it takes advantage of the free-stream independence provided by the $K-\epsilon$ model and in between it uses a combination of both these models using blending functions. The formulation hence derived ensures a proper selection of $K-\epsilon$ and $K-\omega$ zones without any user interaction. Originally, the SST model was intended for use for various aeronautical applications but due to the robustness of its formulation, it is widely used in the external aerodynamics analysis of automotive bodies. In this study, Menter's SST $K-\omega$ turbulence model with default closure coefficients was used to account for universality of the turbulence model for all geometries of Ahmed bodies in all the

different simulations. The formulation of transport equations used in Menter's SST $K-\omega$ turbulence model is given below.

$$\frac{\partial(\rho k)}{\partial t} + \nabla.(\rho k \bar{v}) = \nabla.\left[(\mu + \frac{\mu_t}{\sigma_k})\nabla k\right] + P_k - \rho\beta^* f_{\beta^*}(\omega k - \omega_0 k_0) + S_k \tag{3.2}$$

$$\frac{\partial(\rho\omega)}{\partial t} + \nabla.(\rho\omega\bar{v}) = \nabla.[(\mu + \sigma_\omega \mu_t)\nabla\omega] + P_\omega - \rho\beta f_\beta(\omega^2 - {\omega_0}^2) + S_\omega \tag{3.3}$$

In these equations, the turbulence eddy viscosity μ_t is given by $\mu_t = \rho k T$ where 'ρ' is density, 'T' is the turbulent time scale, and 'k' is the turbulent kinetic energy. In Equations (3.2) and (3.3), '$\bar{v}$' represents the mean velocity, 'μ' is the dynamic viscosity; 'σ_k', 'σ_ω', '$C_{\epsilon 1}$', and '$C_\epsilon 2$' are the closure coefficients, and 'P_k', 'P_ω' are the production terms given by equations $P_k = G_k + G_{nl} + G_b$ and $P_\omega = G_\omega + D_\omega$ respectively where 'G_k' is the turbulent production term, 'G_b' is the buoyancy production term, 'G_{nl}' is the non-linear production term, 'G_ω' is the specific dissipation production term, and 'D_ω' is the cross diffusion term.

To set up the boundary conditions, the wind tunnel is divided into 4 different faces - the inlet, outlet, ground, and the symmetry plane as seen in Figure 3.6. The inlet section is set to velocity inlet with an initial free-stream velocity of 25 m/s which was the velocity used by Strachan [23] in his experiment, the data from which is used to validate this numerical setup. The outlet section was set to pressure outlet, the ground is defined as a no-slip wall with a tangential velocity of 25 m/s to simulate a rolling road, and the far sides and the top of the wind tunnel were defined as symmetry planes (Table 3.4). The same boundary conditions were used for the baseline URANS simulations with a single Ahmed body as well as the 15 overset simulations.

Table 3.4: Boundary conditions setup

Boundary Type	Boundary
Velocity Inlet	Inlet
Pressure Outlet	Outlet
Wall (No-slip)	Ground
Symmetry Plane	Top and Side Walls

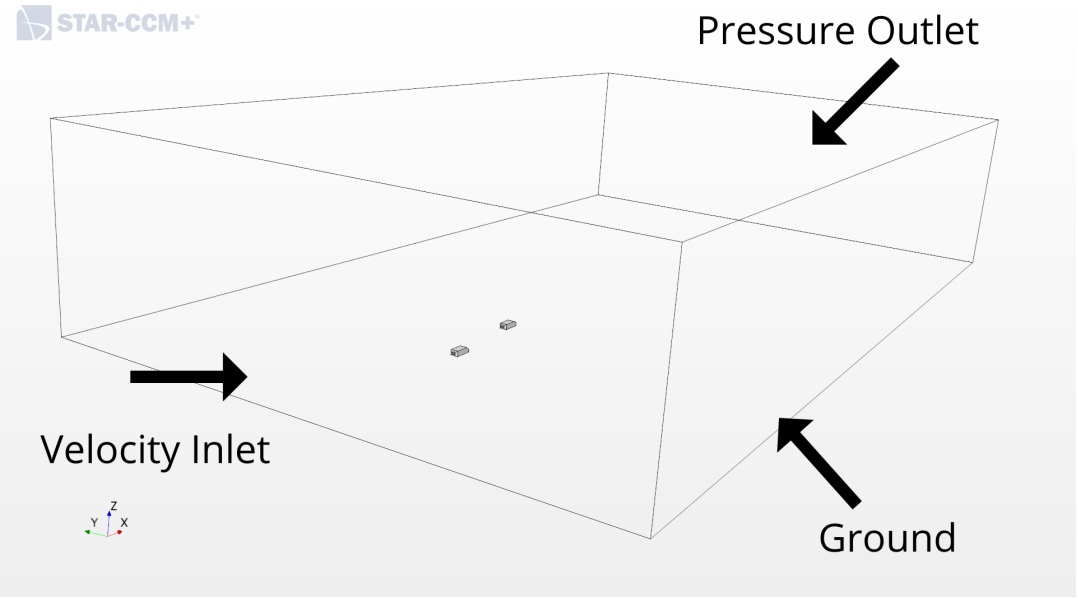

Figure 3.6: Virtual wind tunnel showcasing boundary conditions

CHAPTER 4: RESULTS AND DISCUSSIONS

4.1 Spectral Analysis

The force and moment coefficient plots obtained as a result from all the simulations were observed to require post processing due to a clear presence of noise. This is usually observed when the mesh of the volume considered is unable to resolve small scale motions beyond a certain frequency due to the mesh being coarser than that required by Direct Numerical Simulation (DNS) or LES. While a coarser grid might help save computational resources while still producing results that are acceptable as an accurate engineering solution, the numerical noise as a result of the high frequency patterns is unphysical and has to be removed for the solution to have a physical meaning. In order to clearly analyze the force and moment coefficient plots from all the simulations, a spectral analysis was conducted for all the data.

$$C = \frac{V\Delta t}{\Delta x} \tag{4.1}$$

The mesh size and time step were chosen to keep the Courant number as low as possible. Courant number, given by Equation (4.1), is a dimensionless value that broadly indicates the amount of information traveled across a computional grid per unit time. In the equation, 'V' denotes the local velocity, Δx denotes the cell size, and Δt denotes the time step respectively. In order to ensure convergence and the accuracy of the solution, it is ideal to maintain a Courant number of less than 1. However, as the computational resources to achieve that are very high, it is common practice to ensure the smallest Courant number possible while still maintaining a reasonable computational time and accuracy of the results.

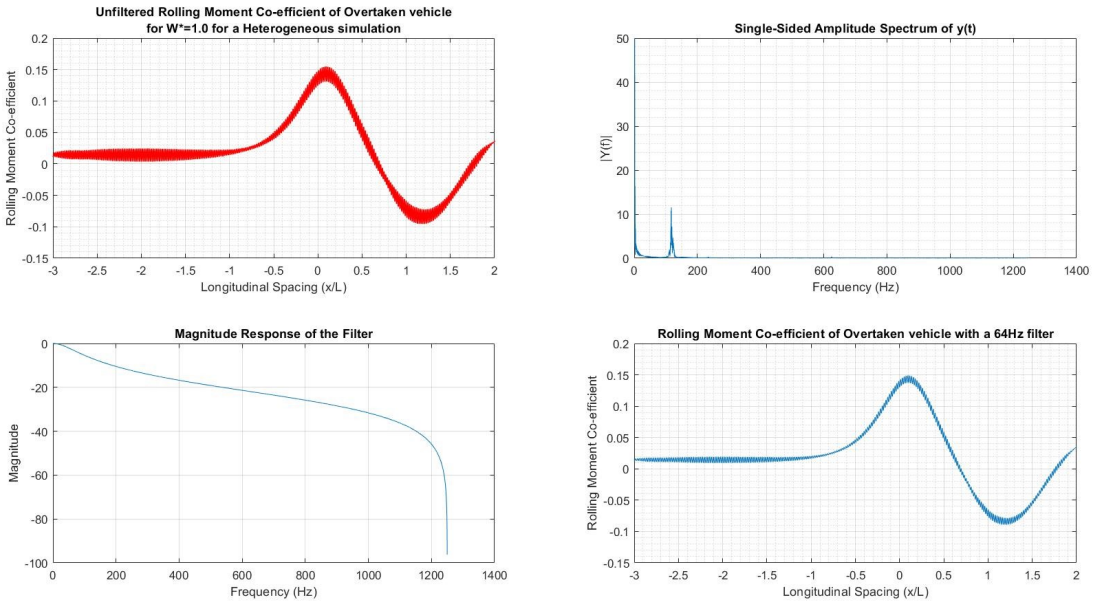

Figure 4.1: Spectral Analysis of the Rolling Moment coefficient of the overtaken body for a heterogeneous simulation (25^o, 35^o) at W*=1.0

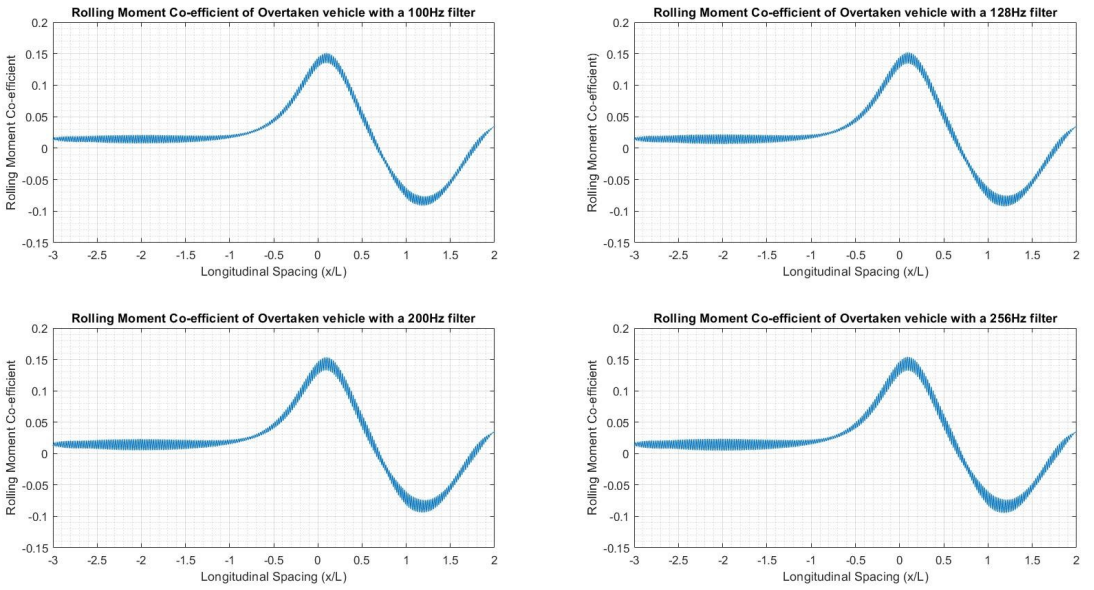

Figure 4.2: Rolling Moment coefficient of the overtaken body filtered at different frequencies

Spectral Analysis of the rolling moment coefficient of the overtaken body for a het-

erogeneous simulation (25^o, 35^o) at W*=1.0 can be seen in Figure 4.1. Considering that a URANS solver only resolves the dominant large scale structures, the smaller structures with higher frequencies that can be seen in the amplitude spectrum plot of Figure 4.1 would have inconsequential effects on the force and moment coefficients. It can be assumed that motions of 1 or more orders of magnitude smaller than the dominant frequency would have no effects on the force and moment coefficients. Therefore, for this analysis, a frequency of 64 Hz was used to consistently filter all the data, using a MATLAB code that was developed by the author. Cut-off frequencies of 100 Hz, 128 Hz, 200 Hz, and 256 Hz were tried, however, they were seen to still contain some noise (as can be seen in Figure 4.3).

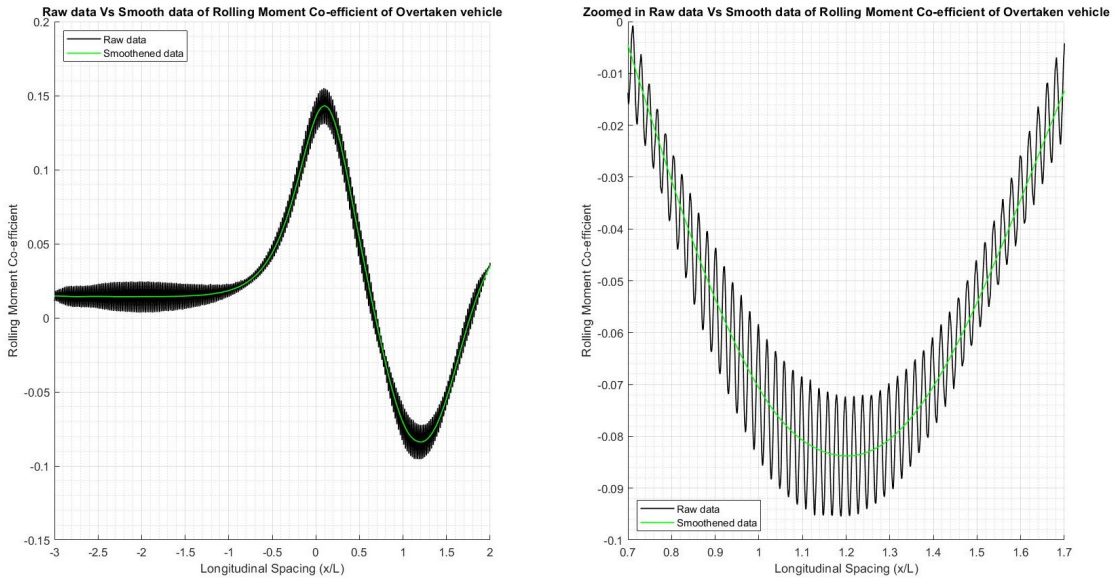

Figure 4.3: Raw data Vs Smoothened data after filtering

Furthermore, the data obtained from using a 64 Hz filter was passed through a Gaussian filter to further smoothen the lines in order to obtain the final plots that were used for this analysis. Figure 4.3 shows the final result of this entire process with respect to the raw data. A plot of rolling moment coefficient was used to showcase the functioning of the filtering process as it was one of the noisiest sets of data. From

the results, it is very clear that the filtering process used was a success at removing noise from the data.

4.2 Effects of Lateral Distancing on the Aerodynamic coefficients

Once the post processing of all the data was completed, the force and moment coefficients were plotted as a function of longitudinal and lateral spacing to help understand the trends in their behavior. Figure 4.4 shows the behavior of the coefficient of drag along the overtaken vehicle for all 5 lateral spacings of W*=0.10, W*=0.25, W*=0.50, W*=0.75, and W*=1.0 respectively for all 5 homogeneous and 10 heterogeneous simulations that were conducted. The results agree well with the experimental results of Noger et al. [13] (Figure 2.17) and CFD results of Uddin et al [16] (Figure 2.22).

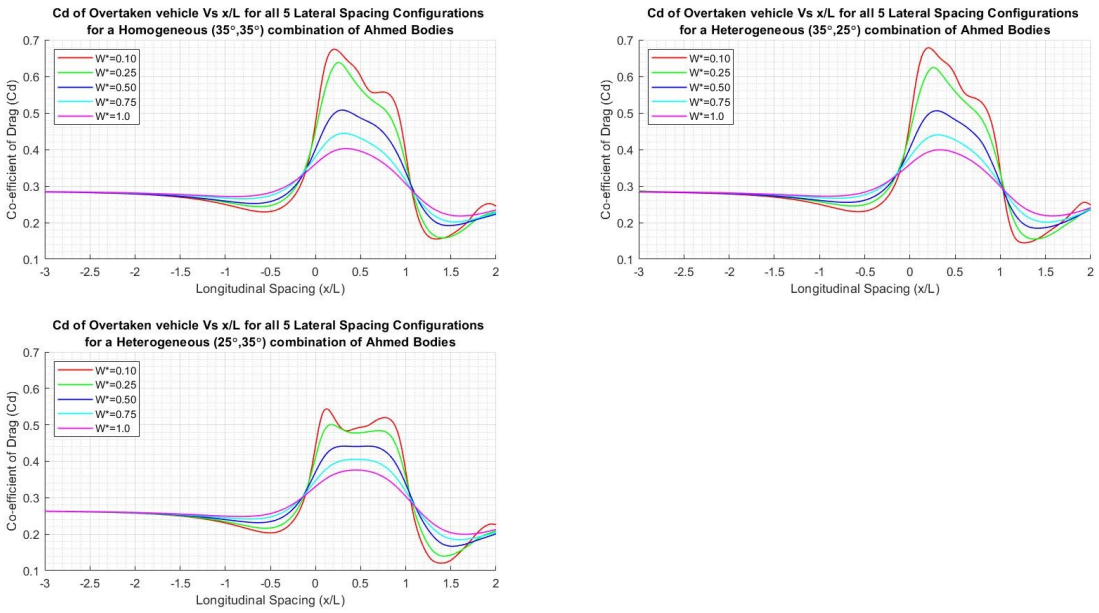

Figure 4.4: Behavior of Drag coefficient along the Overtaken vehicle for all lateral spacings

In Figure 2.17(a), the drag coefficient is plotted at a lateral spacing of W*=0.25 for various values of relative velocities. In Figure 2.17(b), the drag coefficient is

plotted for lateral spacings of W*=0.25, W*=0.50, and W*=0.70 for a fixed value of relative velocity. It can be seen that the general trend of the behavior of Cd from both plots obtained experimentally matches well with the CFD data obtained in Figure 4.4. As observed by Noger et al. [13], it can be seen that the effects of the overtaking maneuver decrease in magnitude with an increase in both longitudinal and lateral spacing respectively as the separation between the overtaken and the overtaking bodies increases.

As a general trend, it can be observed that as the two vehicles approach each other, there is a slight drop in the value of drag coefficient which starts at a longitudinal spacing of nearly -1.5L where 'L' denotes the car length. This drop in drag coefficient is inversely proportional to the lateral spacing with it being the highest at W*=0.10 and smallest at W*=1.0. This drop continues until a local minimum is observed at -0.5L at which point, the value of the drag coefficient begins to rise sharply. At -0.5L, the front of the overtaking vehicle is only half a car length behind the rear of the overtaken vehicle resulting in a strong interaction between the high pressure region at the front of the overtaking vehicle and the low pressure region behind the overtaking region. These interactions were also observed by [10] whose results closely match with the CFD results obtained.

Beyond this point, a sharp rise in the drag coefficient can be seen reaching a local maximum at nearly 0.25L. At this point, the fronts of both overtaken and overtaking vehicles are 0.75 car lengths apart. Interestingly, this peak in the drag coefficient of overtaken vehicle corresponds to a minimum in the drag coefficient of the overtaking vehicle as can be seen in Figure 4.5. These peaks can be attributed to the intense interactions between the pressure fields of the two bodies due to the close proximity. It can be seen that the peaks of the drag coefficient are also inversely proportional to the lateral spacing. The tallest peak is observed at the closest lateral spacing of W*=0.10 and the smallest peak can be observed at W*=1.0. The maximum change

in drag coefficient of the overtaken body for all the simulations can be seen in Table 4.1. It is interesting to observe that for a common overtaken vehicle geometry, the maximum change in the value of the drag coefficient of the overtaken body is almost the same despite the conditions of homogeneity and heterogeneity while changing the overtaken vehicle geometry brought about larger differences in the value of the maximum change in drag coefficient at larger lateral spacings.

Table 4.1: Maximum change in the drag coefficient of the overtaken vehicle for all simulations

Lateral Spacing	Homogeneous setup (35^o,35^o)	Heterogeneous setup (35^o,25^o)	Heterogeneous setup (25^o,35^o)
W*=0.10	0.40	0.40	0.28
W*=0.25	0.36	0.34	0.24
W*=0.50	0.23	0.23	0.18
W*=0.75	0.16	0.16	0.15
W*=1.0	0.12	0.12	0.12

The value of the drag coefficient can be seen dropping sharply beyond 0.75L until both vehicles are side by side (at 1L). At this point, it is interesting to notice that the drag coefficient for all lateral spacings is nearly the same and higher than the free stream drag coefficient. It is also to be noticed that the drag coefficient values of both leading and trailing bodies are nearly the same when the two vehicles are side by side as can be seen in Figure 4.5. This observation aligns with the CFD results of Uddin et al. [16] (Figure 2.22).

Once the overtaking vehicle gets past the overtaken vehicle, a reversal in trends of the drag coefficient can be observed for both the overtaken and the overtaking bodies supporting the literature by Noger at al. [13] and Gillerion et al. [14]. The drag coefficient of the overtaken vehicle dropped to have a local minimum between 1.25L

and 1.5L while that of the overtaking vehicle rose sharply to reach peak values all the way up to a range between 1.75L and 2L at which the simulations ended.

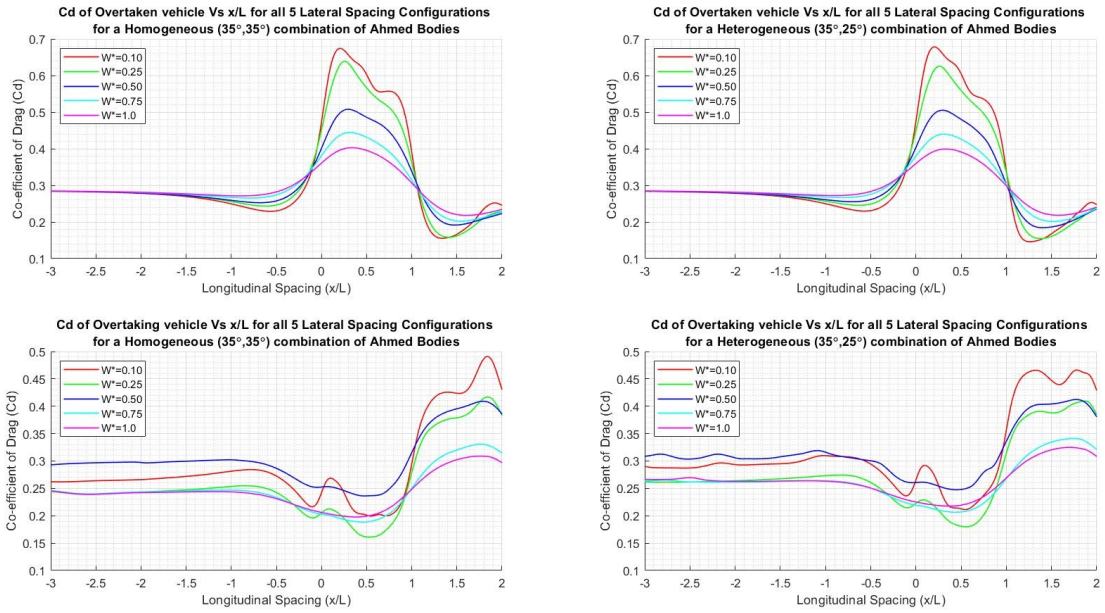

Figure 4.5: Comparison of Drag coefficient along the overtaken and overtaking vehicles for a homogeneous and a heterogeneous system

Figure 4.6 shows the behavior of the coefficient of lift along the overtaken vehicle for all 5 lateral spacings of W*=0.10, W*=0.25, W*=0.50, W*=0.75, and W*=1.0 respectively for all 5 homogeneous and 10 heterogeneous simulations that were conducted. The lift coefficient largely remains unchanged up to -1L at which point it tends to decrease marginally reaching a local minimum for the heterogeneous simulations with 25^o Ahmed body geometry as the overtaken vehicle. For the homogeneous set of simulations and for the heterogeneous set with 35^o Ahmed body as the overtaken vehicle, no drop in value was observed supporting the previously made statement that changing the trailing body geometry does not majorly impact the trends of the force coefficients on the overtaken vehicle. Once the overtaking vehicle is between -0.5L to 0L, a sharp rise in the value of lift coefficient can be seen. This rise continues up to around 0.25L at which it reaches a peak. As observed with the value of the

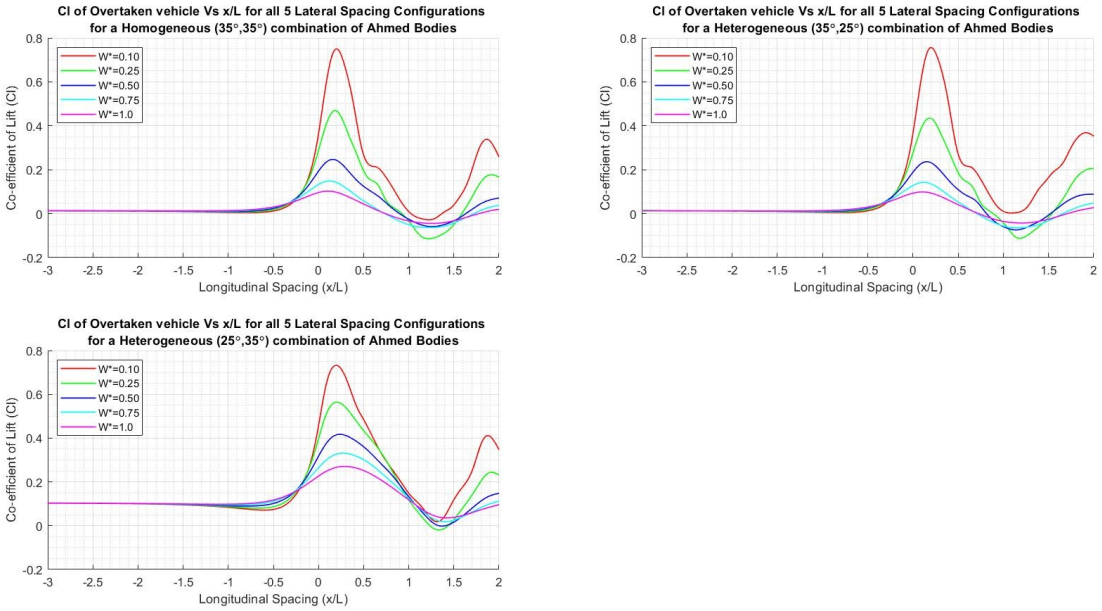

Figure 4.6: Behavior of Lift coefficient along the Overtaken vehicle for all lateral spacings

drag coefficient, the peak value of the lift coefficient is also inversely proportional to the lateral spacing. At this point, the nose of the overtaking vehicle is a quarter car length ahead of the rear of the overtaken vehicle.

Beyond this point, the value of the lift coefficient can be seen to drop sharply until both the vehicles are side by side (1L) at which point, the lift coefficients of both the overtaking and overtaken bodies were observed to be nearly equal which supports the CFD results of Uddin et al. [16]. The lift coefficient continues to drop until the overtaking vehicle pulls slightly ahead by nearly a quarter car length (1.25L) at which point local minimums can be observed. Beyond this point, the trends are reversed for both the vehicles as was observed in the case of the drag coefficient. As the longitudinal spacing increase further, an increase in the lift coefficient of the overtaken vehicle can be seen again up to nearly 1.75L beyond which it tends to start decreasing all the way until 2L.

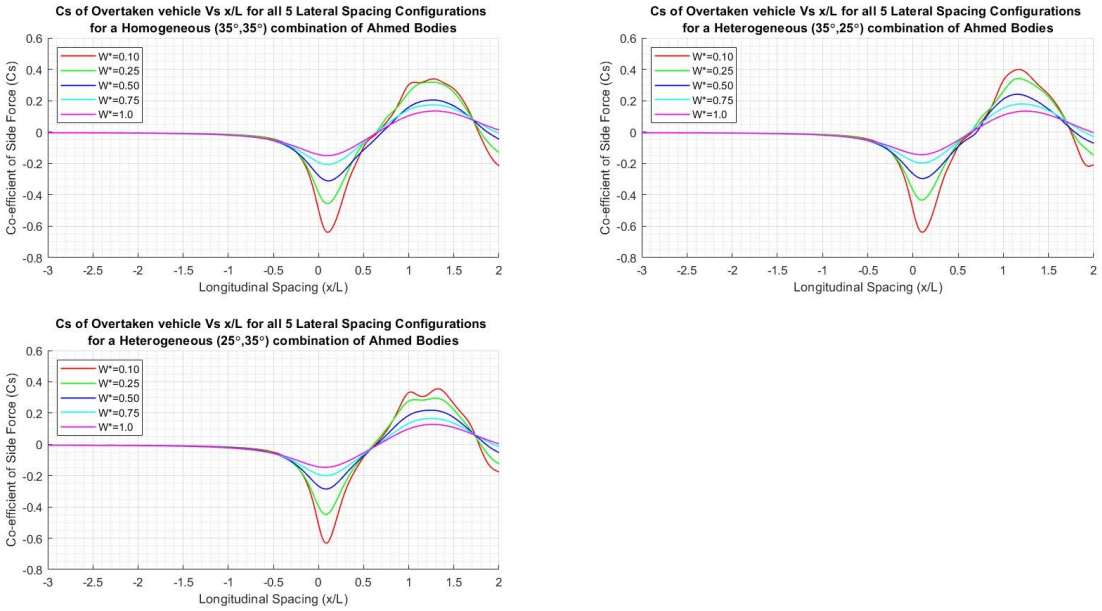

Figure 4.7: Behavior of Side Force coefficient along the Overtaken vehicle for all lateral spacings

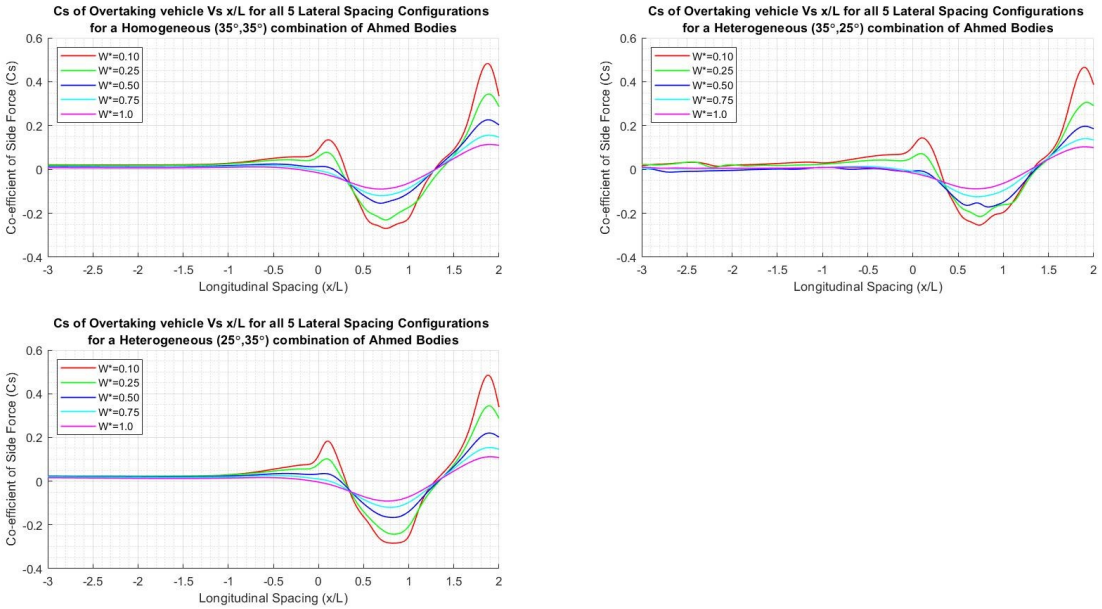

Figure 4.8: Behavior of Side Force coefficient along the Overtaking vehicle for all lateral spacings

Figures 4.7 and 4.8 show the behavior of the coefficient of side force along the overtaken and overtaking vehicles respectively for all 5 lateral spacings of W*=0.10, W*=0.25, W*=0.50, W*=0.75, and W*=1.0 for all 5 homogeneous and 10 heterogeneous simulations that were conducted. The results obtained for the coefficient of side force correlate well with the data obtained by Noger et al. [13] (Figure 2.15), Gillerion et al. [14] (Figure 2.18), and Uystepruyst et al. [15] (Figures 2.19 and 2.21). It can also clearly be observed from Figures 4.7 and 4.8 that the change in side force coefficient decreases with an increase in lateral spacing.

The value of the side force coefficient remained largely unchanged until the overtaking vehicle reached -1L at which point it started to decrease to reach a peak value between 0L and 0.5L. At this point, the nose of the overtaking car is just ahead of the rear of the overtaken car. The peak values in side force coefficient are caused by the interaction of the high pressure region at the nose of the overtaking car with the low pressure region at the rear of the overtaken car. The opposite is observed for the side force coefficient of the overtaking vehicle where an increase in the side force coefficient value is observed along with a local maximum at this location. This opposite trend indicates an increase in velocity of flow in the y-direction pushing the nose of the overtaking vehicle away from the tail of the overtaken vehicle causing a spike in the yawing moment coefficient which will be discussed later on.

Beyond this point, a sharp rise in the value of side force coefficient can be seen for the overtaken vehicle as the overtaking vehicle slowly moves forward and positions itself parallel to the overtaken vehicle (at 1L). At 0.5L, when the nose of the overtaking vehicle is exactly half a car length downstream from the nose of the overtaken vehicle, the values of the side force coefficient for both the overtaken and the overtaking vehicle were observed to be nearly equal. As the overtaking car slowly moves along, a local maximum can be observed between 1L and 1.5L for the overtaken body at this location while the side force coefficient value mirrors itself for the overtaking body and sees

a local minimum. The side force coefficient starts to decrease in magnitude beyond this point all the way the overtaking vehicle reaches 2L while the side force coefficient of the overtaking vehicle continues to rise until it reaches a peak value between 1.5L and 2L. It is to be noticed that the magnitude of this peak value is greater than that of the peak value reached by side force coefficient of the overtaken vehicle and the increase in value varies inversely with the lateral spacing.

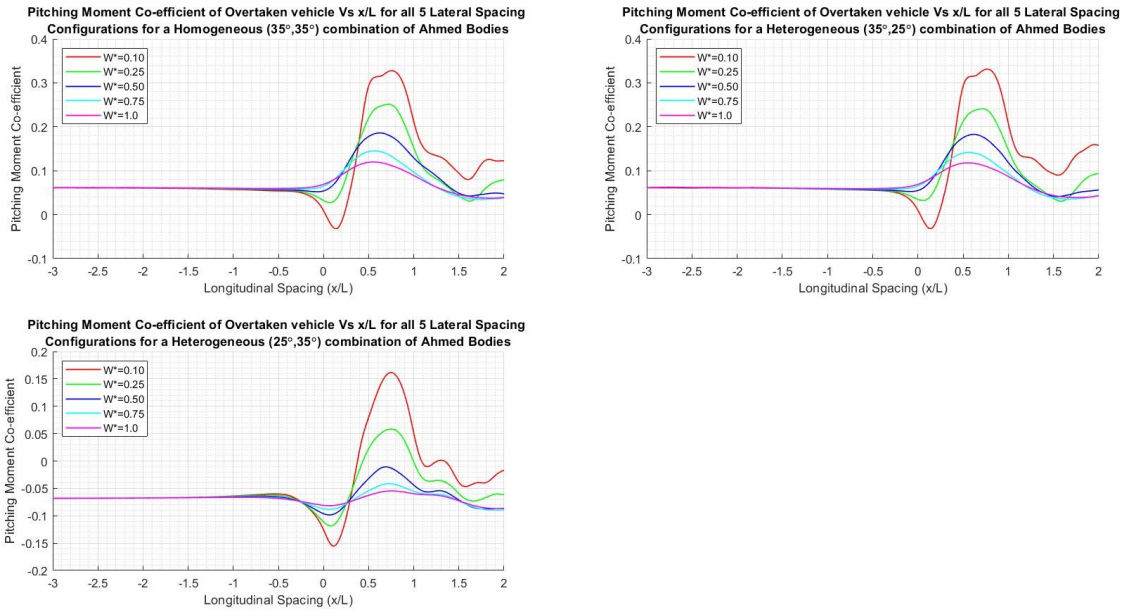

Figure 4.9: Behavior of Pitching Moment coefficient along the Overtaken vehicle for all lateral spacings

Plots of moment coefficients were also generated to help analyze the effects of an overtaking maneuver along with the plots for force coefficients. Figure 4.9 shows the behavior of the coefficient of lift along the overtaken vehicle for all 5 lateral spacings of W*=0.10, W*=0.25, W*=0.50, W*=0.75, and W*=1.0 respectively for all 5 homogeneous and 10 heterogeneous simulations. The magnitude of the effect of the overtaking maneuver on the change in the pitching moment coefficient can be seen to correspond inversely with the lateral spacing. Between 0L and 0.5L, when the nose of the overtaking vehicle is roughly a quarter car length ahead of the tail

of the overtaken vehicle, a local minimum can be observed on the pitching moment coefficient of the overtaken vehicle. This can again be attributed to the interaction of the high and low pressure regions at the nose of the overtaking vehicle and the tail of the overtaking vehicle respectively causing an increase in the z-component of velocity of the flow. Beyond this point, a sharp rise in the value of the pitching moment coefficient can be seen as both the vehicles align side by side and a peak can be observed at a point when the nose of the overtaking vehicle is a quarter car length behind the nose of the overtaken vehicle. Following this, the value dropped sharply. However, it is interesting to notice that for lateral spacings of W*=0.10 and W*=0.25, the two closest lateral spacings, the pitching moment coefficient does not completely go back down to the free-stream pitching moment coefficient unlike the case for the other lateral spacings. Due to the very close proximity in the first two cases, it can be safely assumed that it would take a longer time and a bigger separation between the two vehicles for the pitching moment coefficient to go back to the free-stream value.

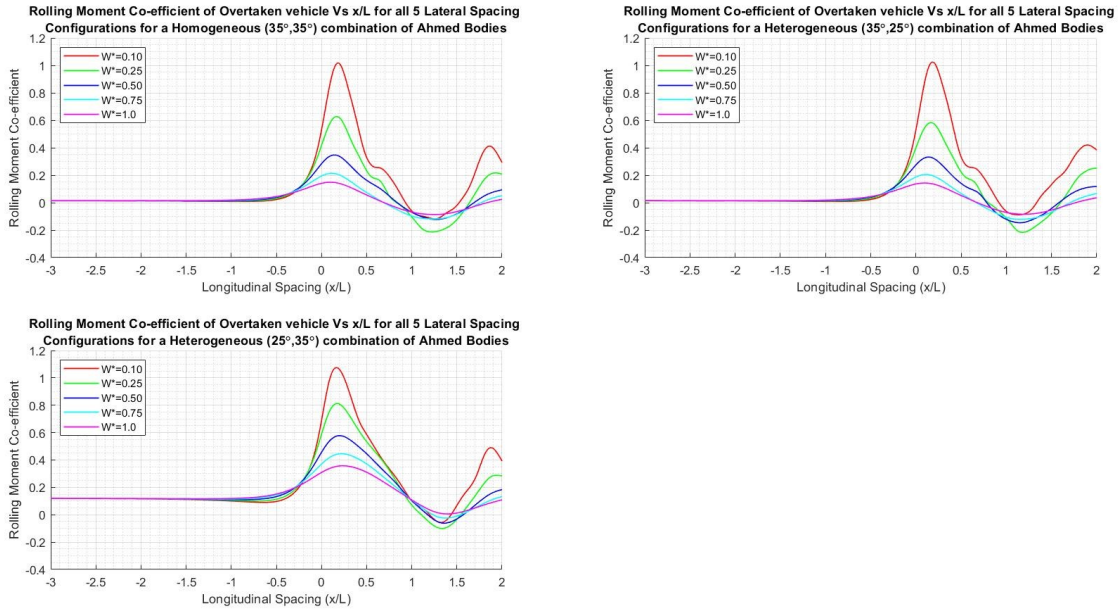

Figure 4.10: Behavior of Rolling Moment coefficient along the Overtaken vehicle for all lateral spacings

The trends in the distributions of rolling moment coefficient along the overtaken vehicle for all 5 lateral spacings of W*=0.10, W*=0.25, W*=0.50, W*=0.75, and W*=1.0 for all 5 homogeneous and 10 heterogeneous simulations can be seen in Figure 4.10. As the overtaking body tends to approach the vehicle being overtaken, a huge spike in the rolling moment coefficient can be seen which starts rising at nearly -0.5L pas which the peak values are observed at nearly 0.25L when the nose of the overtaking vehicle is just in front of the tail of the overtaking vehicle. Beyond this point, the value tends to decrease sharply reaching a minimum at 1.25L when the nose of the overtaking body is a quarter car length ahead of the nose of the overtaken vehicle. A second, yet smaller, maximum can be observed between 1.5L and 2L after which the rolling moment coefficient value can be assumed to slowly fall back to it is original free-stream value as the overtaking vehicle moves further upstream.

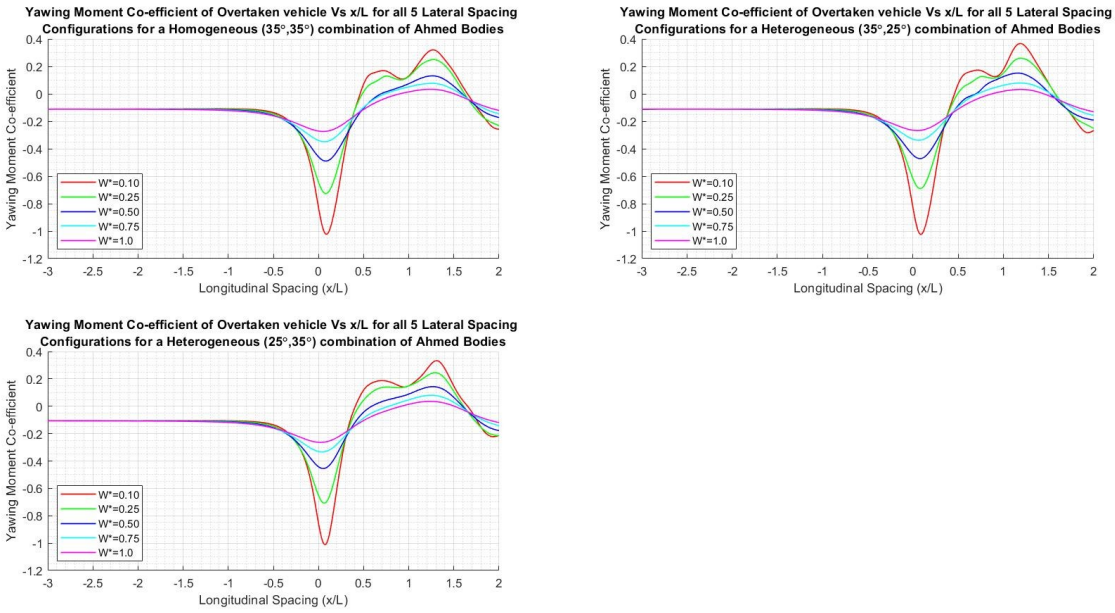

Figure 4.11: Behavior of Yawing Moment coefficient along the Overtaken vehicle for all lateral spacings

The yawing moment coefficient is yet another very important factor in analysing the effects of an overtaking phenomenon. The trends in the behavior of the yawing

moment coefficient along the overtaken vehicle for all 5 lateral spacings of W*=0.10, W*=0.25, W*=0.50, W*=0.75, and W*=1.0 for all 5 homogeneous and 10 heterogeneous simulations can be seen in Figure 4.11. The effects on the Yawing moment coefficient were extensively studied by Noger et al. [13] and Uystepruyst et al. [15]. Figures 2.15, 2.19, and 2.21 show the trend in the yawing moment coefficient distribution as obtained in their studies. It can be seen that the CFD data corresponds very well with that of the experiments. It is to be noted, however, that the axis convention used to plot the experimental data differs to that of the CFD data. The axis convention of the CFD simulations can be seen in Figure 3.1. The 'y' and 'z' axes used in this convention have opposite directions compared to the convention that was used to plot the experimental data. Figure 4.12 compares the yawing moment coefficient along the overtaken and overtaking vehicles for a set of homogeneous and a heterogeneous simulations.

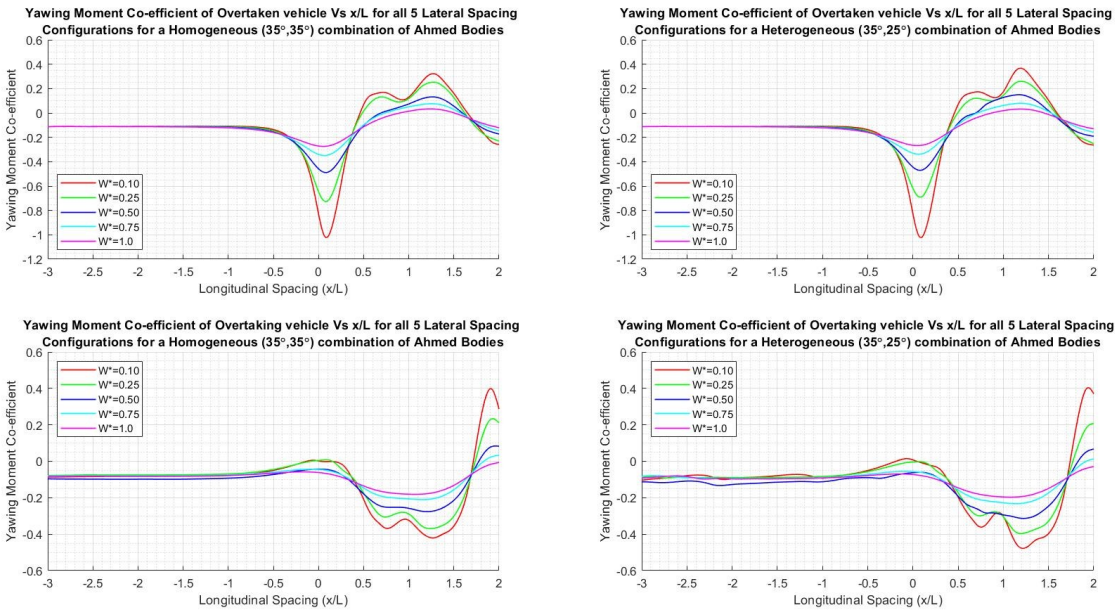

Figure 4.12: Comparison of Yawing Moment coefficient along the overtaken and overtaking vehicles for a homogeneous and a heterogeneous system

It is again very clear from the CFD data that the effects of the overtaking maneuver

on the change in the value of yawing moment coefficient on both overtaken and overtaking vehicles is inversely proportional to the lateral spacing. The yawing moment coefficient of the overtaken vehicle largely remained unchanged until the overtaking vehicle reached -0.75L at which point, it started to drop drastically to have a peak minimum at roughly 0.25L when the nose of the overtaking vehicle is just ahead of the tail of the overtaken vehicle. This peak can be attributed to the increase in side force between the nose of the overtaking vehicle and the tail of the overtaken vehicle at this location (Figure 4.7) due to the interactions of the high and low pressure regions in front of the overtaking vehicle and the rear of the overtaken vehicle respectively. Due to these pressure interactions, a large increase in the magnitude of velocity of the y-direction pushes against both the bodies thereby pushing the nose of the overtaking vehicle away from the tail of the overtaken vehicle. The effects of this interaction on the overtaking vehicle can be seen in Figure 4.8. The yawing moment coefficient of the overtaking vehicle are in contrast to the overtaken vehicle and have a local maximum at this point (0.25L).

As the overtaking vehicle continues to move forward, the value of the yawing moment coefficient of the overtaken vehicle rises sharply until it reaches a first peak just after 0.5L, at which point the nose of the overtaking vehicle is half a car length away from the nose of the overtaken vehicle. For the overtaking vehicle, a negative peak is observed which is almost a mirror image of the behavior that was predicted for the overtaken vehicle. It is to be observed however, that just before the overtaking vehicle reaches 0.5L, the values of the yawing moment coefficient for both the overtaking and the overtaken vehicle are nearly equal. A second peak can be observed 1.25L just after the overtaking vehicle moves past the overtaken vehicle by a quarter car length. This peak is again mirrored in the negative direction for the overtaking vehicle. Beyond this point, the yawing moment coefficient of the overtaken vehicle can be seen to slowly settle down to its free-stream value further upstream. How-

ever, for the overtaking vehicle, the yawing moment coefficient rises sharply from the negative peak to have yet an other peak on the positive side between 1.5L and 2L after which it can be assumed to settle down to it's free stream value. While data exists to compare the trends in the moment coefficients of the overtaken vehicles in both overtaking and platooning cases, no data is available to compare the same for the overtaking vehicle.

The effects of the overtaking maneuver as a function of lateral/traverse spacing on the force and moment coefficients obtained from study support the existing experimental studies conducted by Noger et al. [13] and Uystepruyst et al. [15] which showed that as the lateral spacing between the vehicles is increased, the effects of the overtaking maneuver on the force and moment coefficients are decreased.

4.3 Effects of Heterogeneity on the Aerodynamic coefficients

To the best of the author's knowledge, there is no data from experimental studies to understand the effects of heterogeneity on the aerodynamics coefficients during an overtaking phenomenon. However, Pagliarella et al. [10] and Watkins et al. [9] have conducted experimental studies to analyze the effects of heterogeneity in a platooning scenario. The net saving in drag using several combinations of Ahmed body geometries as observed by Watkins can be seen in Figure 2.11. In their studies, both Pagliarella and Watkins used a set of sub-critical (25^o) and super-critical (35^o) Ahmed body geometries to understand the effects of heterogeneity to whose results, the trends in drag and lift coefficients from CFD are compared. The author aims to present and analyze the effects of heterogeneity during an overtaking maneuver on the overtaken vehicle in this section.

Figure 4.13 compares the trends of the coefficient of drag of the overtaken vehicle for the homogeneous set of simulations and the two sets of heterogeneous simulations at all lateral spacings. From the figure, it can be seen that the initial value of drag coefficient is higher for the two sets of simulations with 35^o geometry as the overtaken

model while the value of drag coefficient for the simulation set with 25^o geometry overtaken body is slightly lower. Furthermore, the trends in the behavior of the two sets of simulations with a 35^o model as the overtaken model are very similar with only minute differences. On the other hand, major changes in the pattern of drag coefficient can be in the simulation set with 25^o geometry as the overtaken vehicle especially at the peaks. This can also be noticed in Table 4.1 where the maximum change in drag coefficient of the overtaken vehicle with 25^o Ahmed body as the overtaken geometry is considerably less at larger lateral spacings as compared to the other two sets of simulations with a 35^o geometry as an overtaken vehicle.

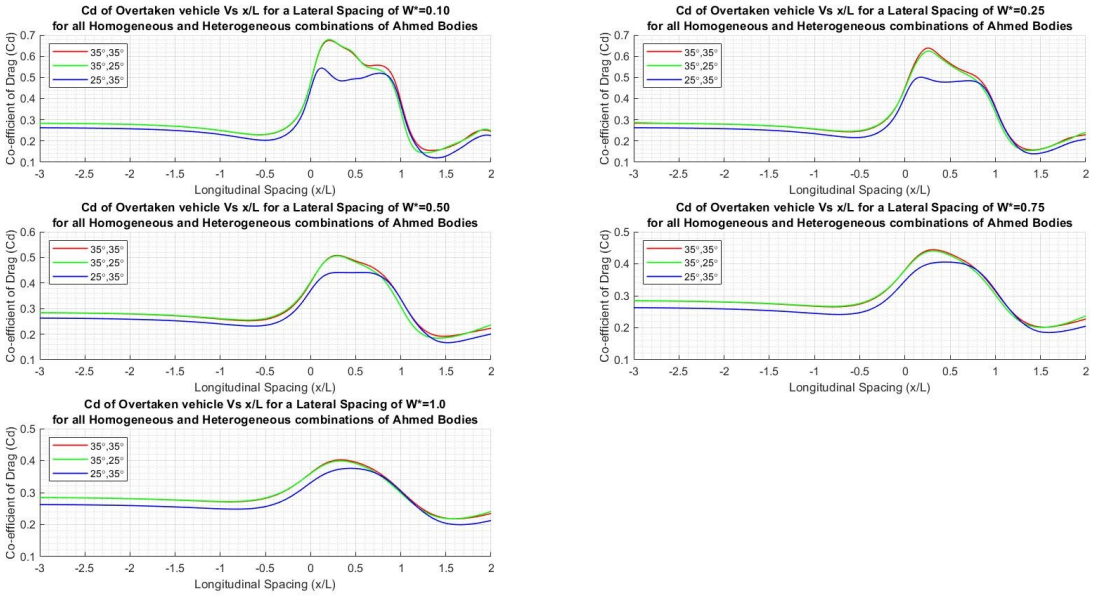

Figure 4.13: Comparison of Drag coefficient along the Overtaken vehicle for all Homogeneous and Heterogeneous simulations

This observation is in line with Watkins' conclusion that the aerodynamic performance of the overall system, i.e., the two bodies as a whole is broadly dominated by the geometric configuration of the overtaken model (or the leading model in case of a platoon) regardless of the heterogeneity of the two vehicle system with a different overtaking (or trailing) vehicle model. Also the analysis done in the previous section,

the overtaking model for a given overtaken model shows only minor differences at close proximity, the performance beyond which was is largely insensitive. From the CFD data, it can also be seen that the most significant boost in performance of the two vehicle system as a whole is realized when the overtaken body is a super-critical or a 35^o Ahmed body geometry further supporting Watkins' conclusions.

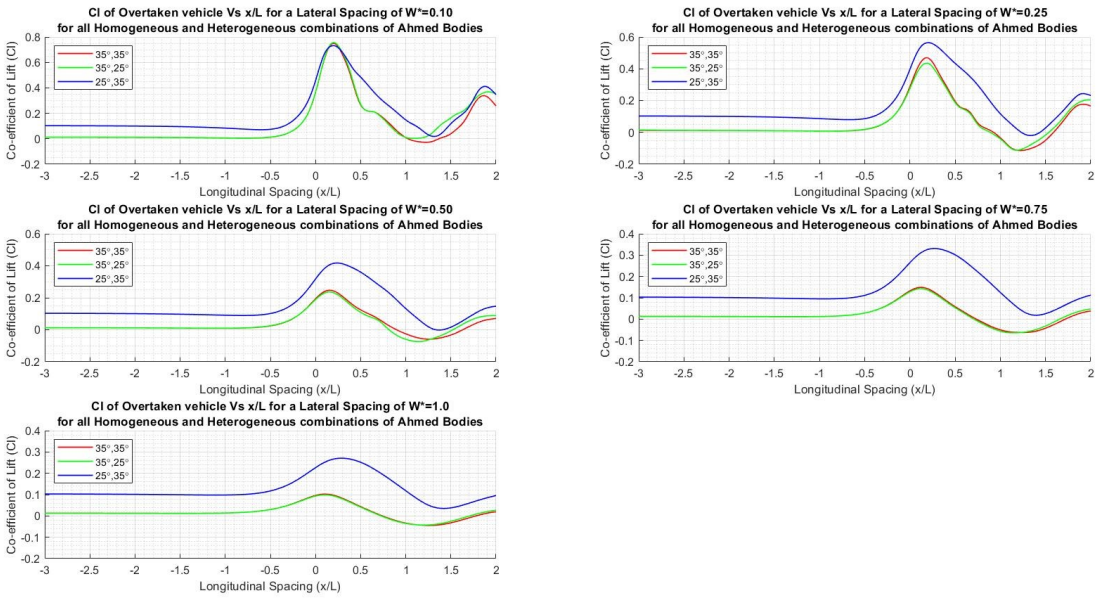

Figure 4.14: Comparison of Lift coefficient along the Overtaken vehicle for all Homogeneous and Heterogeneous simulations

A comparison of the trends in the coefficient of lift of the overtaken Ahmed body for the homogeneous set of simulations and the two sets of heterogeneous simulations at all lateral spacings can be seen in Figure 4.14. The initial value of the lift coefficient of the simulation set with the 25^o overtaken model is higher than that of the sets i=with 35^o model owing to the difference in geometry. The simulation set with the 25^o geometry model as the overtaken model displays the most change in the case of the life coefficient as well. The peak values for the simulations with a 35^o overtaken model are lower than that of the 25^o model. However, it is interesting to see that the location of all the peaks and the local maximums and minimums for both drag and

lift coefficients are consistent despite having different magnitudes.

An other interesting observation is that the difference in peak values of lift coefficients between the two overtaken vehicle geometries is increasing with an increase in lateral spacing. This is counter intuitive considering we know that the effects of the overtaking phenomenon diminish with an increase in the lateral spacing. However, this can be reasoned with one of the two explanations, the first one being the inability of RANS models to correctly predict flow reattachment on the rear slant of the 25^o geometry at the front thereby predicting a larger separation region and effecting considerably the prediction of lift coefficient and its behavior. The other reasoning would be the effects of lateral spacing. At close proximity, there is a very strong interaction of the pressure regions between the high and low pressure regions at the nose of the overtaking vehicle and the tail of the overtaken vehicle respectively which decrease in magnitude with increasing lateral spacing due to which a huge increase of velocity in the 'y' and 'z' directions can be observed. This increase in velocity in the z-direction can not only increase the peak values of the lift coefficient of the overtaken vehicle, it can also increase the peak values of the rolling moment coefficient as well. If this is the case, then it would make sense that the changes due to the heterogeneity increase with respect to lateral spacing up to a point after which, the effects due to overtaking diminish with a further increase in lateral spacing thereby decreasing the effects on the overtaken geometry.

Figure 4.15 compares the trends of the coefficient of side force of the overtaken vehicle for all the homogeneous and heterogeneous simulations at different lateral spacings. Unlike in the previous two cases with drag and lift coefficients, the side force coefficient shows the least amount of change due to heterogeneity of both the overtaking and the overtaken bodies. While there are minor changes in the magnitudes of the peak values of the coefficient of side force, the trend largely remains the same. As is the case with both lift and drag coefficients, all the simulations share

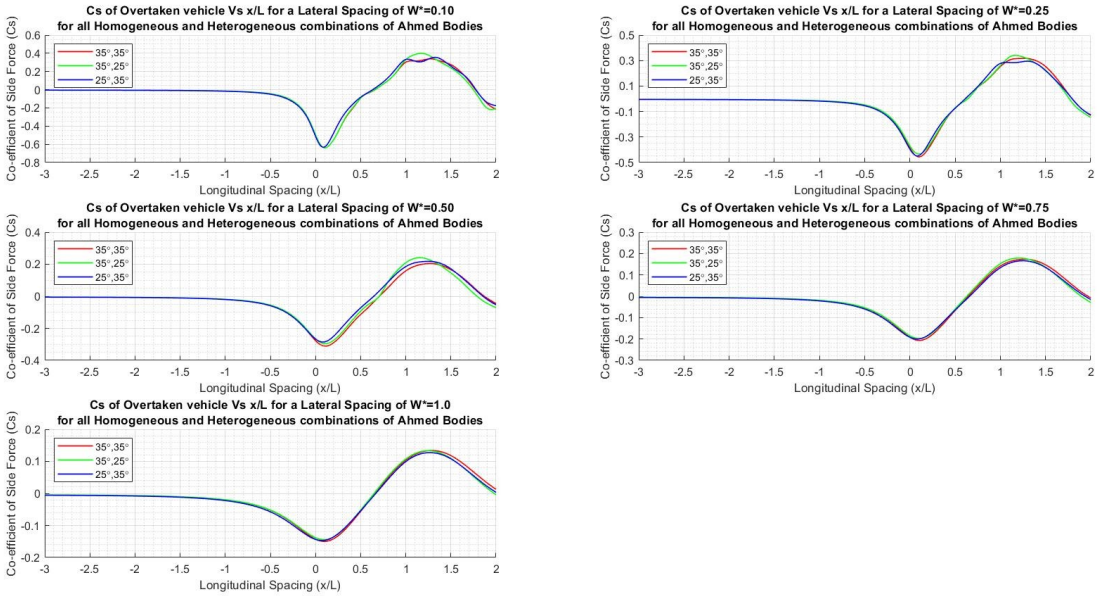

Figure 4.15: Comparison of Side Force coefficient along the Overtaken vehicle for all Homogeneous and Heterogeneous simulations

the same position at which maximum and minimum peaks are observed although the magnitude of the peaks themselves vary as an inverse function of the lateral spacing as can be expected. From this data, as the magnitudes of the minimum and the maximum peaks of all the simulations are nearly equal, it can be safely said that an equal amount of side force exists between the nose of the overtaking body and the tail of the overtaken body due to which the yawing moment coefficient that acts on the front left of the overtaking body (pushing it right) and the rear right of the overtaken body (pushing it left) should be of nearly equal magnitude on both bodies for all simulations. This statement was also proven earlier while analyzing Figure 4.12.

A comparison of the trends in the coefficient of pitching moment of the overtaken Ahmed body for all the simulations at different lateral spacings can be seen in Figure 4.16. A huge decrease in the magnitude of the initial pitching moment coefficient value can be seen for the simulations with a 25^o geometry as the overtaken body. Out of all the force and moment coefficients analyzed, the pitching moment coefficient was the

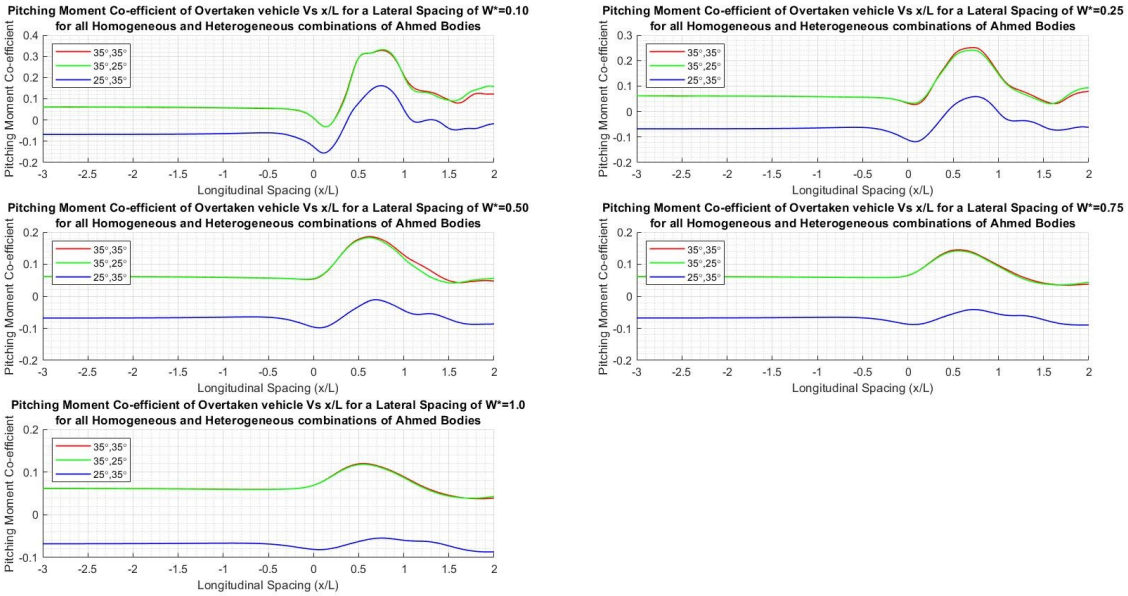

Figure 4.16: Comparison of Pitching Moment coefficient along the Overtaken vehicle for all Homogeneous and Heterogeneous simulations

most sensitive to the effects of heterogeneity when the overtaken vehicle geometry is changed although the changes that came with varying the overtaking vehicle geometry were minimal. This difference in value is carried out throughout the entire time period of the simulation. The interesting observation here is that for W*=0.10, 0.25, and 0.50, the difference in value of the pitching moment coefficient between the sets of simulations with varying overtaken body remained nearly consistent at most points along the longitudinal spacing while for W*=0.75 and 1.0, a very small change in the difference is observed at the location of the peaks.

Figure 4.17 compares the trends of the coefficient of rolling moment of the overtaken vehicle for the homogeneous set of simulations and the two sets of heterogeneous simulations at all values of lateral spacings. The effects due to heterogeneity on the behavior of the rolling moment coefficient are very similar to that of the lift coefficient. While the dominant reason for the change in aerodynamic performance is still the presence of a different overtaken geometry as in the 25^o, 35^o case, the change in the

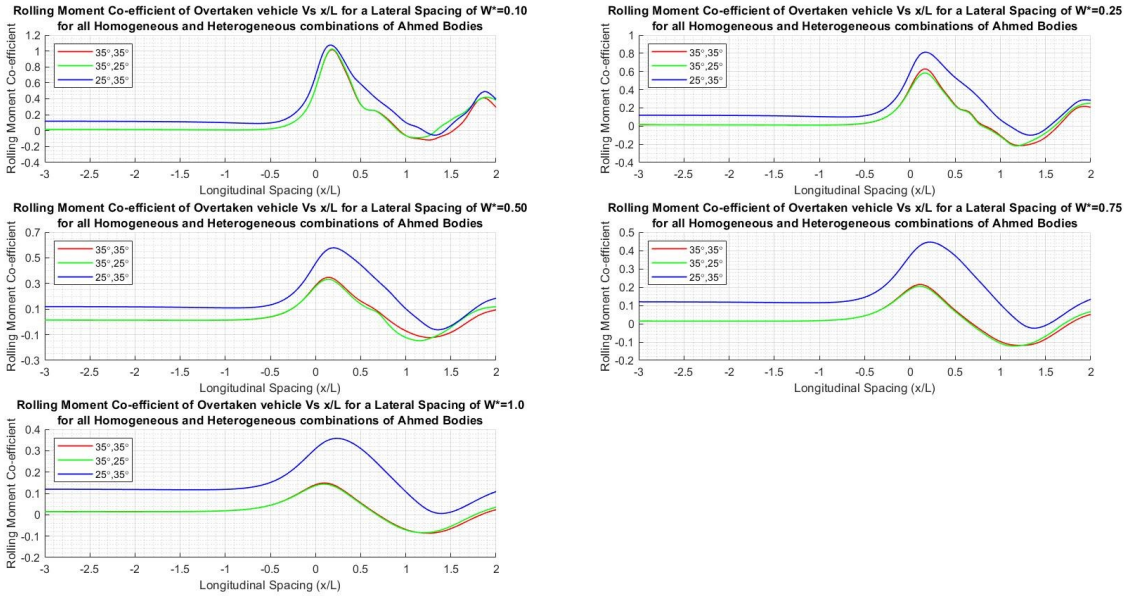

Figure 4.17: Comparison of Rolling Moment coefficient along the Overtaken vehicle for all Homogeneous and Heterogeneous simulations

peak value of the rolling moment coefficient seems to be increasing with an increase in lateral spacing the explanation of which was presented earlier in this section. With the exception of this one counter-intuitive observation, the prediction of the rolling moment coefficient is as expected.

As seen in the previous sections of this analysis, the change in yawing moment coefficient takes a maximum absolute value when the nose of the overtaking vehicle is in line with the tail of the overtaken vehicle at which point, there is a huge side force acting on both bodies trying to push the bodies away from each other. This statement was proved in the previous sections of this analysis. Drawing a conclusion from this, it can be said that the magnitude of yawing moment coefficient will change as a direct function of the side force coefficient. A comparison of the trends in the coefficient of yawing moment of the overtaken Ahmed body for all the simulations at different lateral spacings can be seen in Figure 4.18. From the figure, it can be seen that, along with the side force coefficient, the yawing moment coefficient is the least

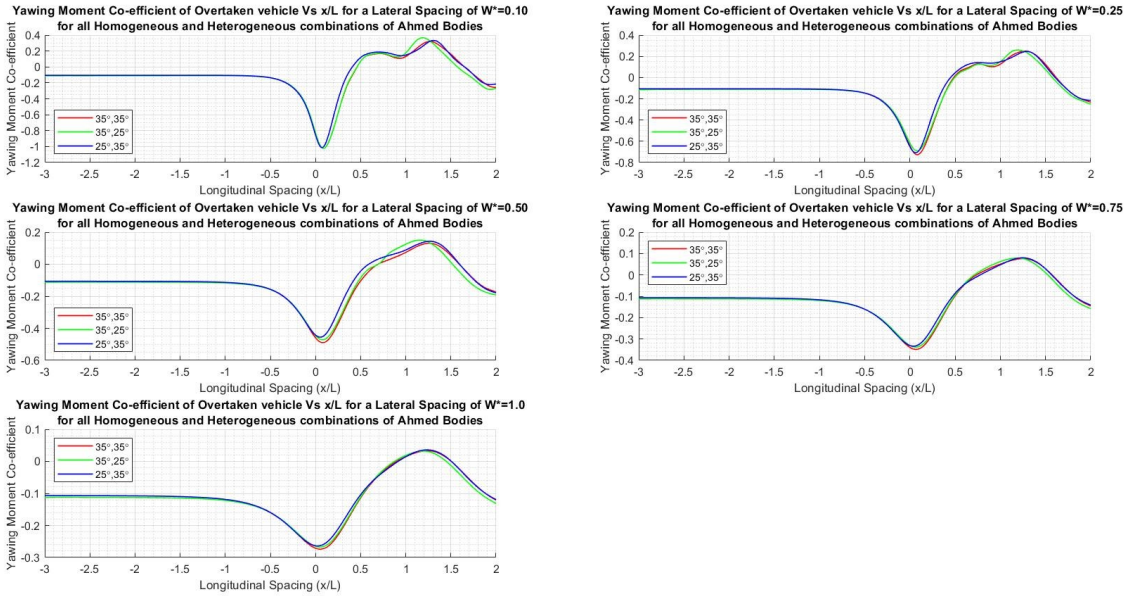

Figure 4.18: Comparison of Yawing Moment coefficient along the Overtaken vehicle for all Homogeneous and Heterogeneous simulations

sensitive to the effects of heterogeneity for varying both the overtaking and overtaken vehicle geometries. And as expected, all the simulations share the same position at which maximum and minimum peaks are observed although the magnitude of the peaks themselves vary as an inverse function of the lateral spacing.

4.4 x/L from Initial to -0.5

In order to fully understand the trends of the aerodynamic coefficients explained in the previous sections, the analysis of the results is further broken down into smaller steps based on the longitudinal spacing. Several scalar scenes were generated throughout the course of the simulation in order to evaluate the reasons behind the trends in aerodynamic coefficients. In these next few sections, scalar scenes of the homogeneous set of simulations are compared with one set of heterogeneous simulations with 25^o Ahmed body as the overtaken geometry. As we have seen previously, the aerodynamic performance of the two car system is broadly dominated by the geometry of the

overtaken vehicle and not much change is observed when heterogeneity is introduced by replacing the overtaking vehicle. Hence, only two sets of simulations (35^o, 35^o and 25^o, 35^o) are discussed below in the following sections using scalar scenes.

To properly understand the trends in the distribution of drag coefficient, we have to take a deeper look at the profiles of pressure coefficient. The interaction of the high pressure region at the nose of the overtaking vehicle and the low pressure region at the tail of the overtaken region started interacting at a longitudinal spacing x/L=-2. This interaction was more prominent in the homogeneous case where the 35^o Ahmed body geometry was used for the overtaken vehicle. Figures 4.19 and 4.20 showcase the distribution of pressure along the top view of the two vehicle homogeneous and heterogeneous systems respectively at x/L=-2. This was the point at which the drag coefficient of the overtaken vehicle initially started to drop slowly as can be seen in Figure 4.4.

To understand this further, we can look at the scenes generated for the velocity in x-direction. In the positive x-direction, the velocity field in the wake region of the overtaken body can be seen interacting with the nose of the overtaking vehicle thereby reducing the velocity of the overtaking vehicle in x-direction. This velocity lost in the x-direction is the sum total of the combined velocities gained in the 'y' and 'z' directions respectively. Figures 4.21 and 4.22 show the distribution of Vx along the top view of the two vehicle homogeneous and heterogeneous systems respectively at x/L=-2. It can be clear from the figures that lateral spacing plays a crucial role in the overall aerodynamic performance of the system. For smaller lateral distances, the interaction of the nose of the overtaking body with Vx in the wake region of the overtaken body is significantly higher as compared to the case with more lateral spacing. This impingement of the wake on the nose of the overtaking region combined with the interactions of the high and low pressure regions of both bodies provide a clear insight of the variation in the profile of drag coefficient of both bodies.

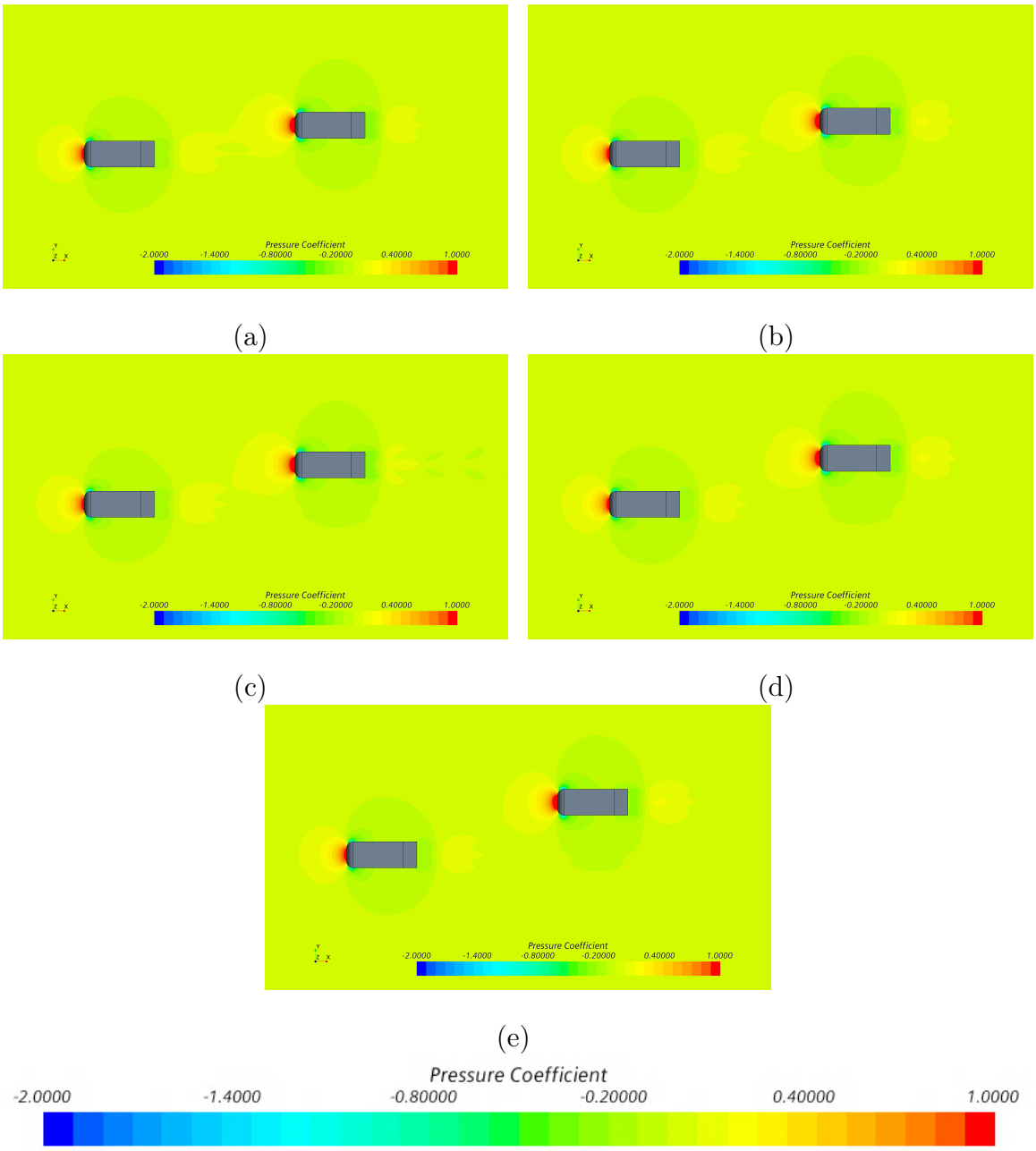

Figure 4.19: Pressure distributions along the two vehicle homogeneous system at x/L=-2 for (a) W*=0.10, (b) W*=0.25, (c) W*=0.50, (d) W*=0.75, and (e) W*=1.0

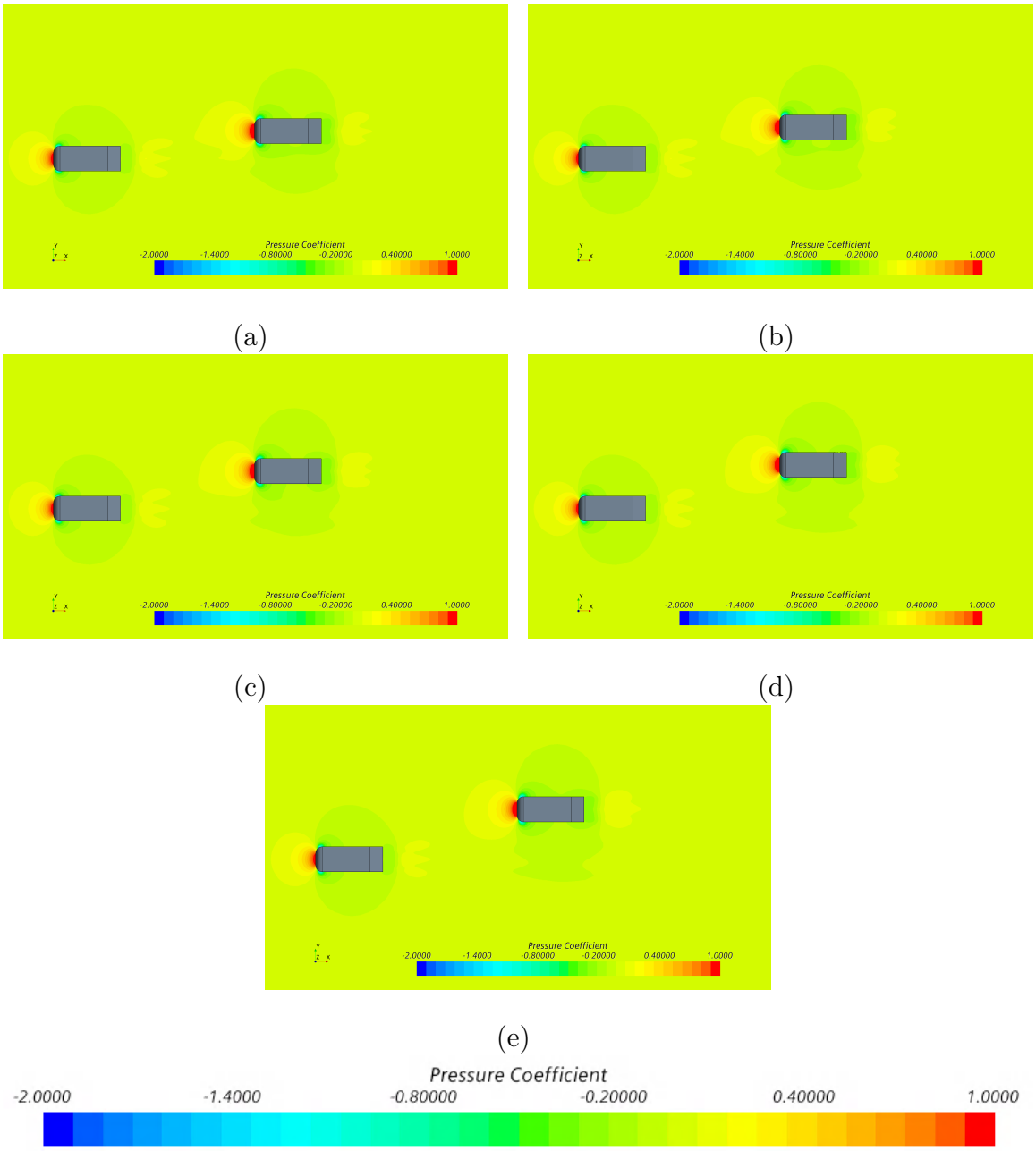

Figure 4.20: Pressure distributions along the two vehicle heterogeneous system at x/L=-2 for (a) W*=0.10, (b) W*=0.25, (c) W*=0.50, (d) W*=0.75, and (e) W*=1.0

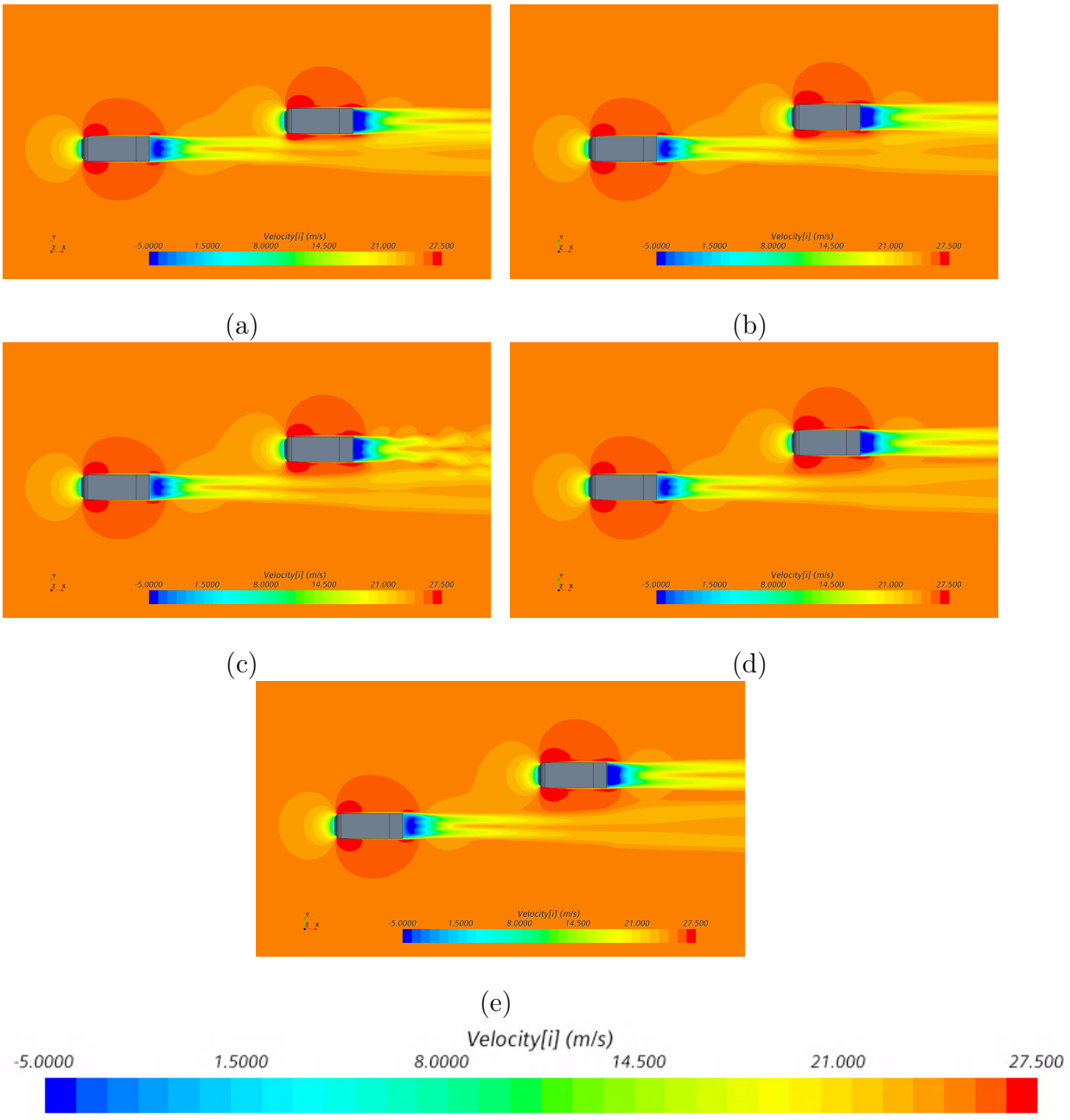

Figure 4.21: Vx distributions along the two vehicle homogeneous system at x/L=-2 for (a) W*=0.10, (b) W*=0.25, (c) W*=0.50, (d) W*=0.75, and (e) W*=1.0

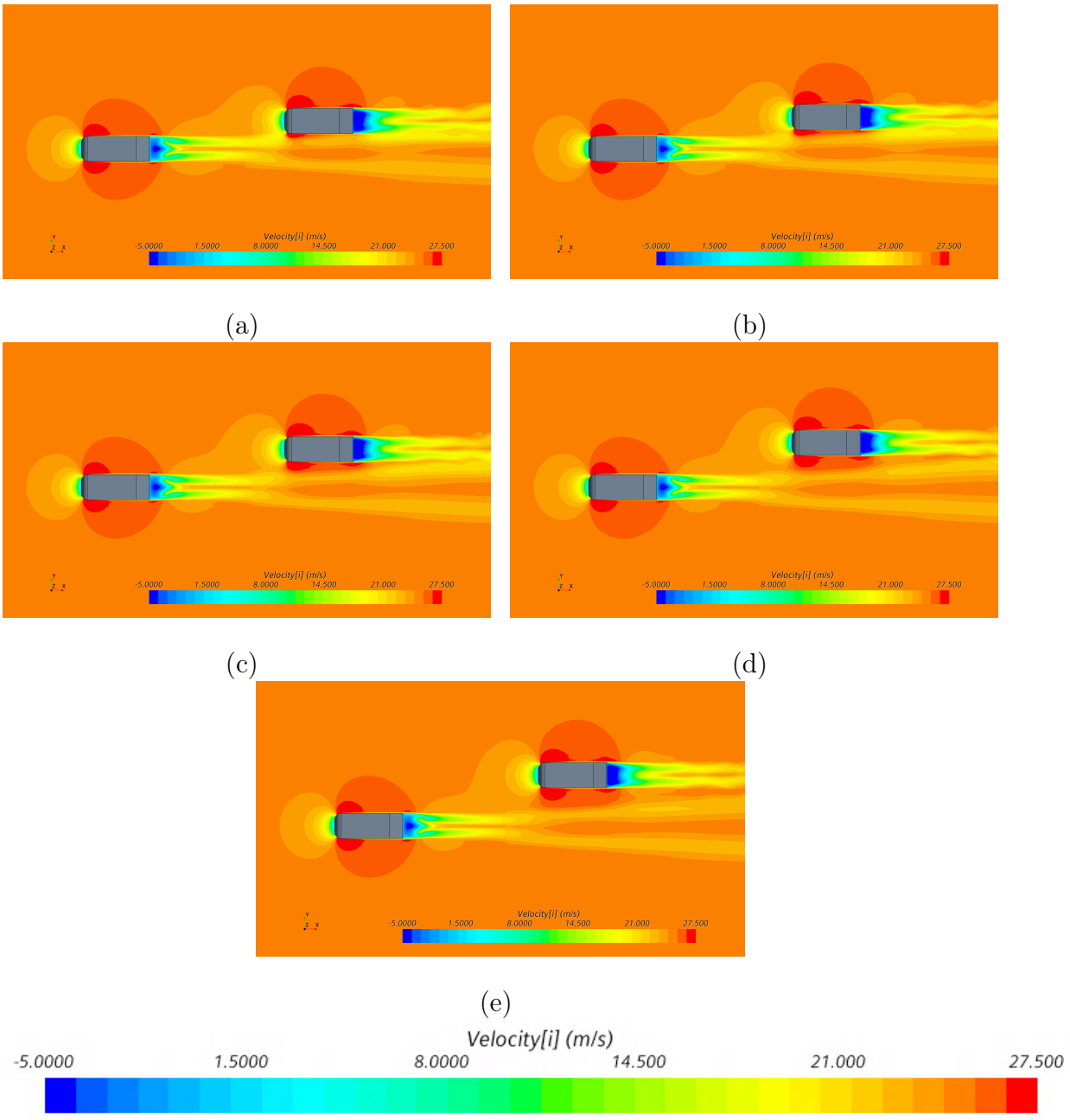

Figure 4.22: Vx distributions along the two vehicle heterogeneous system at x/L=-2 for (a) W*=0.10, (b) W*=0.25, (c) W*=0.50, (d) W*=0.75, and (e) W*=1.0

Figures 4.23 and 4.24 showcase the distribution of Vy along the top view of the two vehicle homogeneous and heterogeneous systems respectively at x/L=-2. While a slight increase in the y-component of velocity can be noticed when the wake region of the overtaken vehicle interacts with the nose of the overtaking vehicle, no significant effects on the aerodynamic properties of the overtaken and overtaking bodies is observed due to the larger longitudinal separation. The effects of heterogeneity at this position are still not profound. However, it is clear from the figures that the amount of interaction between the trailing body and the y-component of velocity in the wake of the overtaken vehicle is significant at W*=0.10. As the lateral spacing increases, this interaction decreases as it is to be expected. As the overtaking vehicle gets closer to the overtaken vehicle beyond this point, studying the y-component would be very important in order to understand the trends in side force coefficient and the yawing moment coefficient which will be discussed in next section.

Figures 4.25 and 4.26 showcase the distribution of Vz along the top view of the two vehicle homogeneous and heterogeneous systems respectively at the same lateral spacing of x/L=-2. As is the case with the y-component of velocity, a slight increase in the z-component of velocity can be observed at this location. This gain in velocity in z-direction is part of the velocity lost in the x-direction of the overtaking vehicle due to wake impingement and the interaction of the pressure regions between the two vehicles. While this gain is yet insignificant at this point due to the large longitudinal spacing, it can be observed that the maximum gain is obtained for the W*=0.10 case due to the close proximity of the two vehicles. As the lateral spacing increases, the net change in the z-component of velocity also decreases as it is to be expected. It is also interesting to observe that the change in the z-component of the velocity is higher for the heterogeneous cases compared to the homogeneous cases.

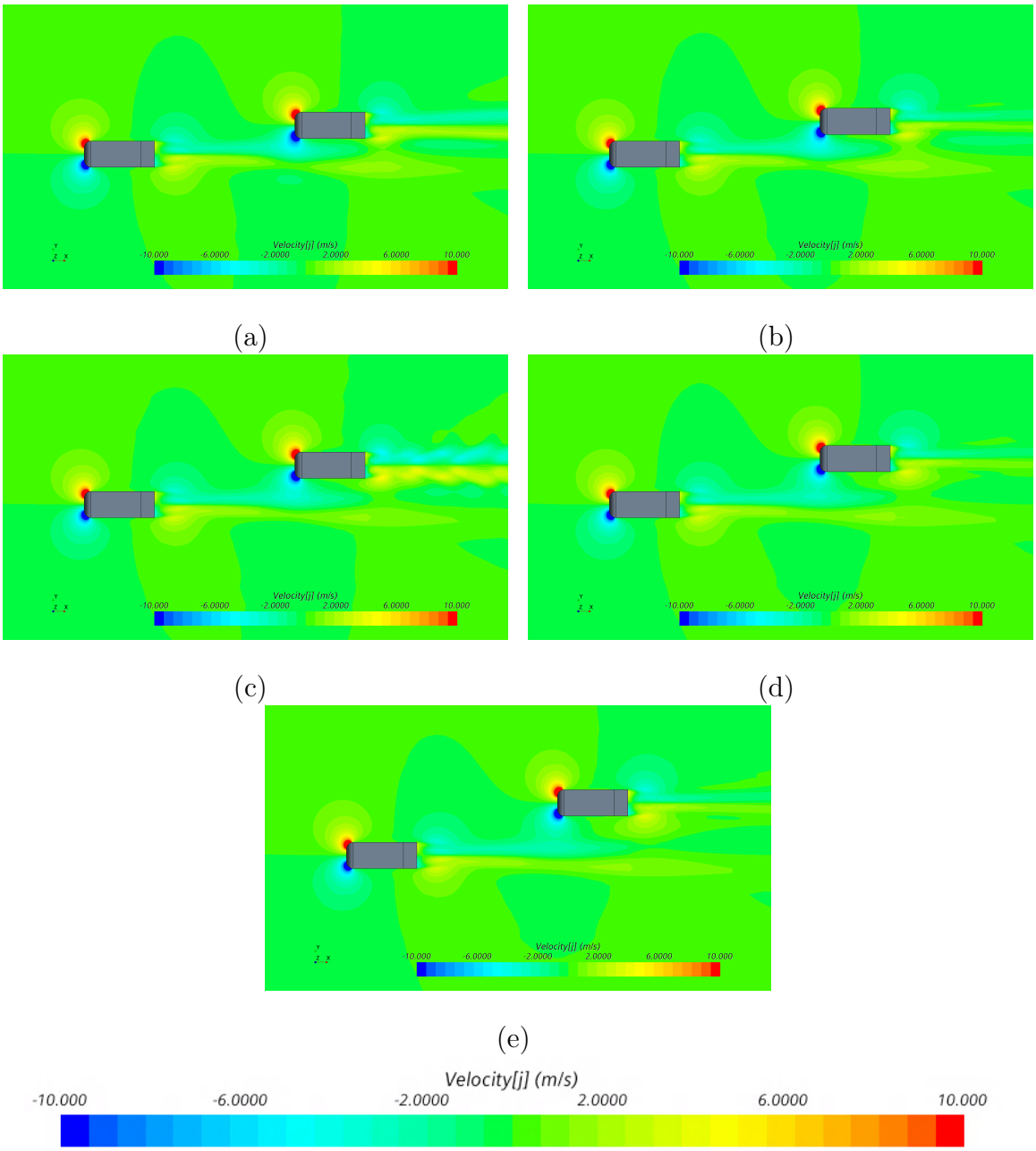

Figure 4.23: Vy distributions along the two vehicle homogeneous system at x/L=-2 for (a) W*=0.10, (b) W*=0.25, (c) W*=0.50, (d) W*=0.75, and (e) W*=1.0

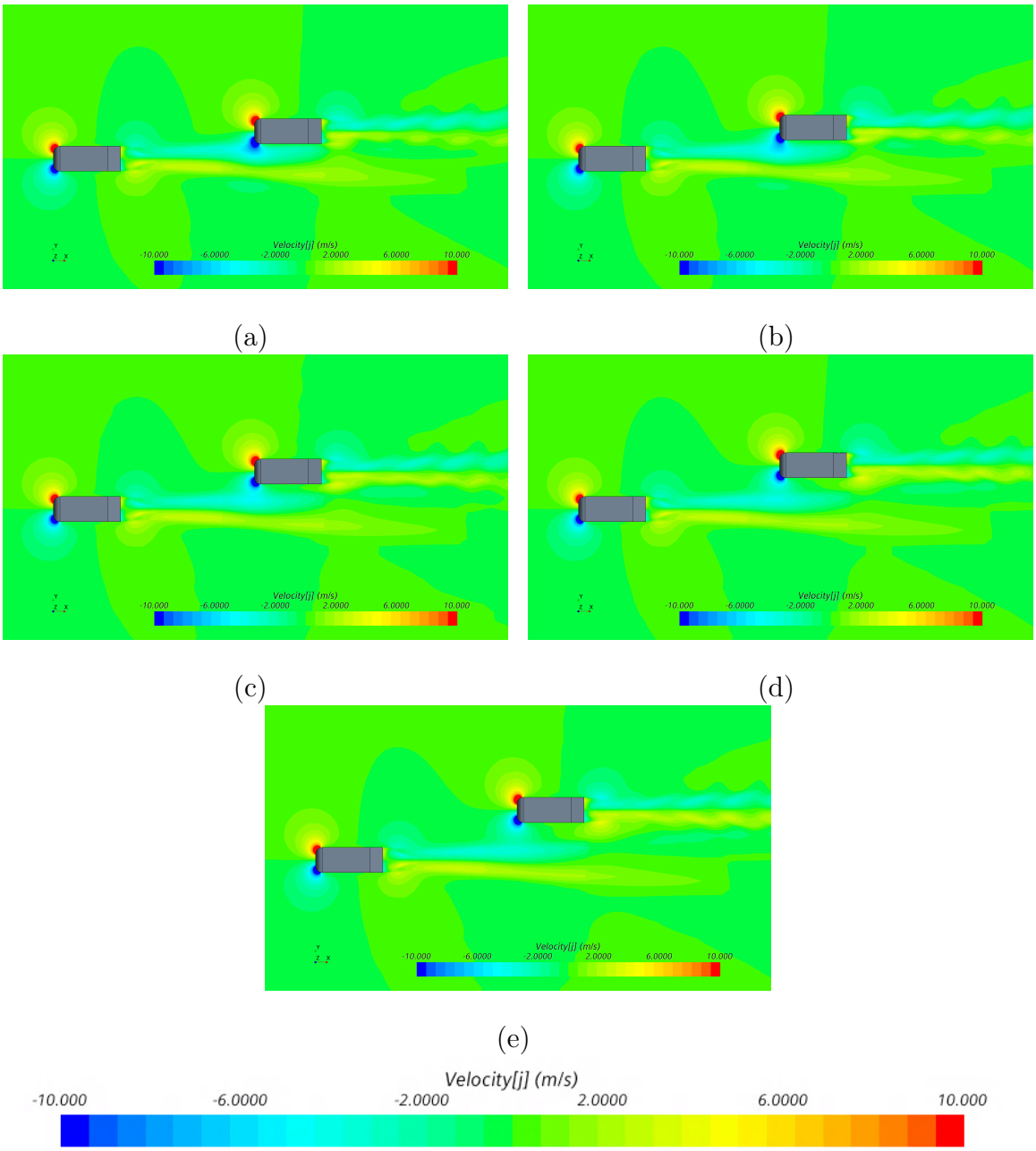

Figure 4.24: Vy distributions along the two vehicle heterogeneous system at x/L=-2 for (a) W*=0.10, (b) W*=0.25, (c) W*=0.50, (d) W*=0.75, and (e) W*=1.0

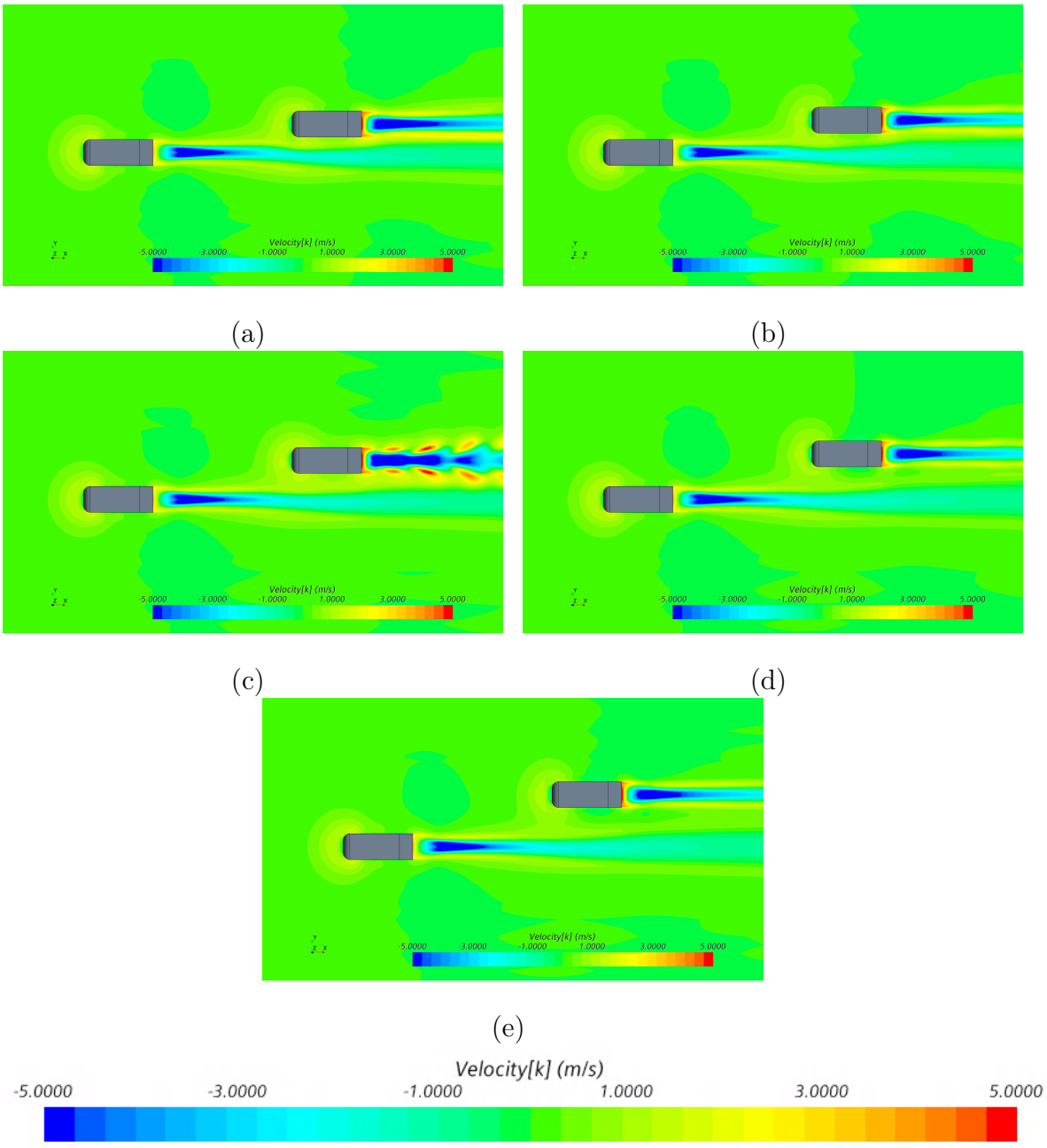

Figure 4.25: Vz distributions along the two vehicle homogeneous system at x/L=-2 for (a) W*=0.10, (b) W*=0.25, (c) W*=0.50, (d) W*=0.75, and (e) W*=1.0

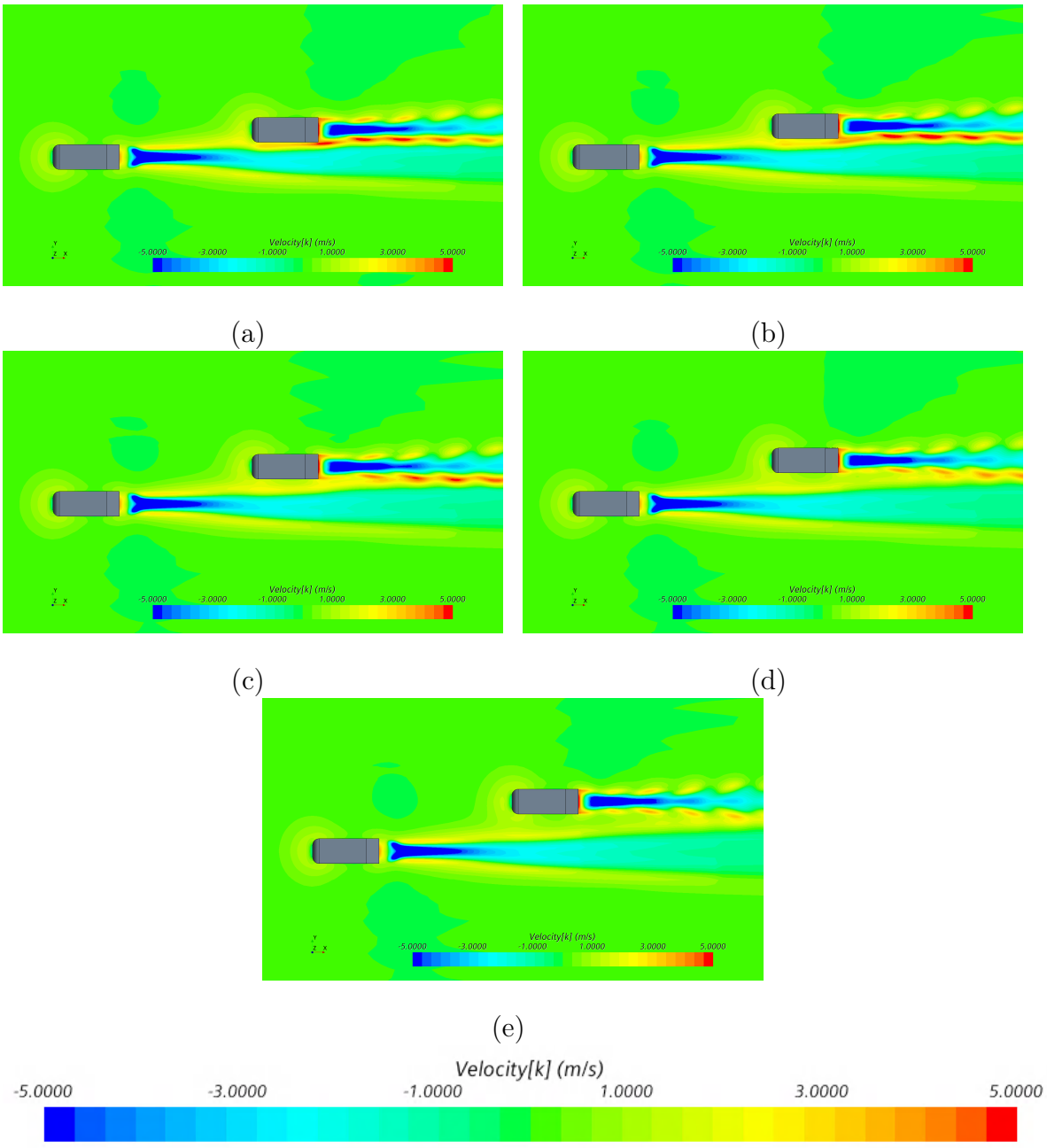

Figure 4.26: Vz distributions along the two vehicle heterogeneous system at x/L=-2 for (a) W*=0.10, (b) W*=0.25, (c) W*=0.50, (d) W*=0.75, and (e) W*=1.0

As the overtaking vehicle continues to travel upstream, the sensitivity of the aerodynamic coefficients of both vehicles to the presence of the other vehicle begins to rise. At x/L=-0.5, a local minimum was observed for the drag coefficient of the overtaken vehicle. This is also the point at which the lift coefficient of the overtaken vehicle was seen to have a sharp rise according to both CFD and experimental data. The side force coefficient of the overtaken vehicle for all the simulations, which is found to not have any effect up to this point begins its descent to the peak minimum. Major changes in the trends of the rolling and pitching moment coefficient can also be observed at this location. The yawing moment coefficient of both bodies begins to rise in opposite directions at this location as we've seen in the previous sections. Therefore, it is important to study the several scenes at this location in order to understand these changes in the trends of the aerodynamic coefficients.

The pressure coefficient distribution at this location for the homogeneous and heterogeneous simulations can be seen in Figures 4.27 and 4.28 respectively. In the figures, it can be seen that there is a strong interaction between the high pressure region at the nose of the overtaking vehicle and the low pressure region at the rear of the overtaken vehicle. The effects due to wake impingement are more pronounced at this location with the high pressure region at the nose of the overtaking vehicle pressing into and suppressing the low pressure region and the wake of the overtaken vehicle. This results in a high pressure region in the space between the two vehicles due to which significant rise can be observed in the yawing moment coefficients and the side force coefficients of the two bodies. As expected, these effects were more significant at close proximity (causing larger peak values force and moment coefficients) and as the lateral spacing increased, the effects due to this high pressure region decreased for both the homogeneous and heterogeneous sets of simulations.

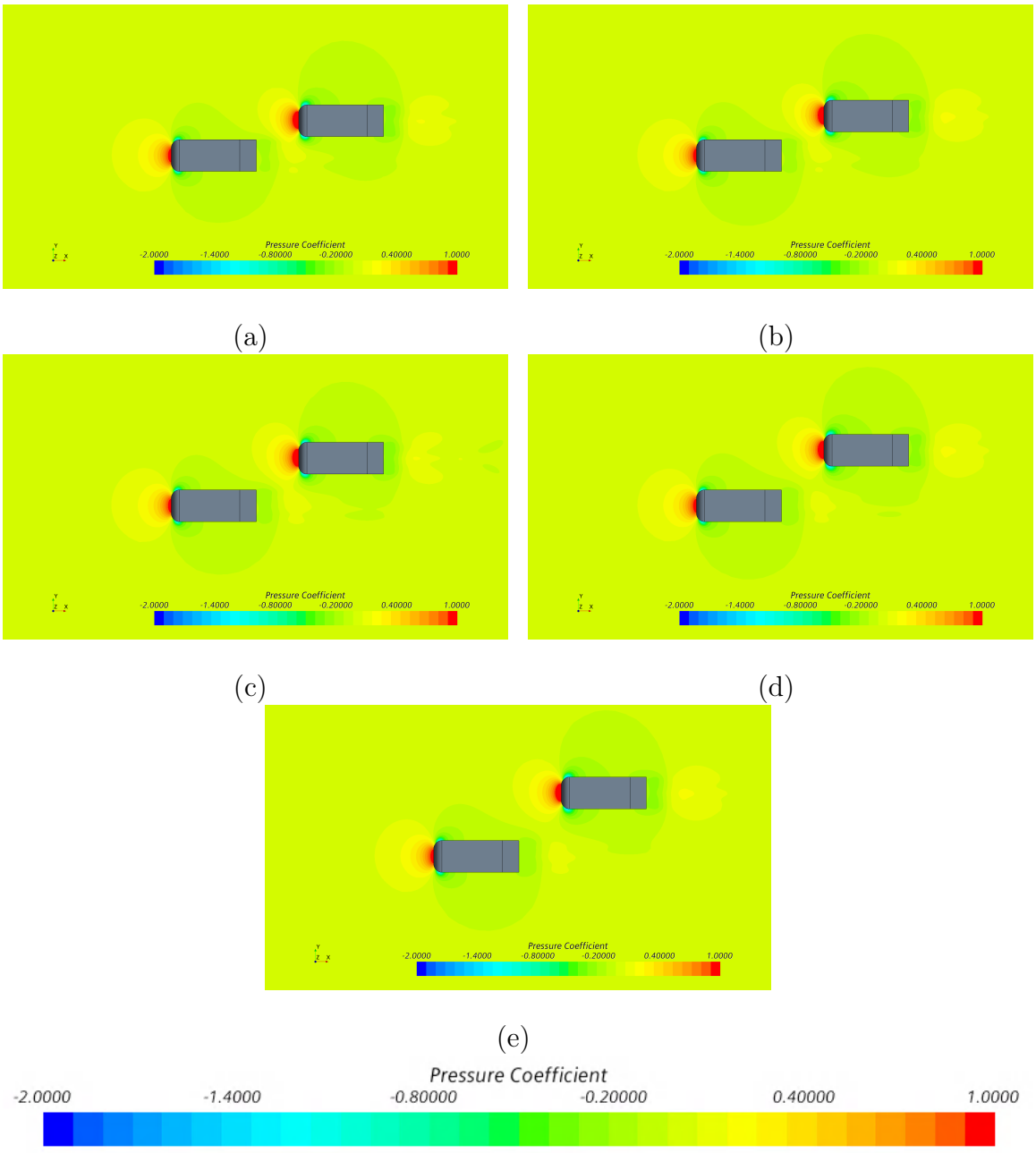

Figure 4.27: Pressure distributions along the two vehicle homogeneous system at x/L=-0.5 for (a) W*=0.10, (b) W*=0.25, (c) W*=0.50, (d) W*=0.75, and (e) W*=1.0

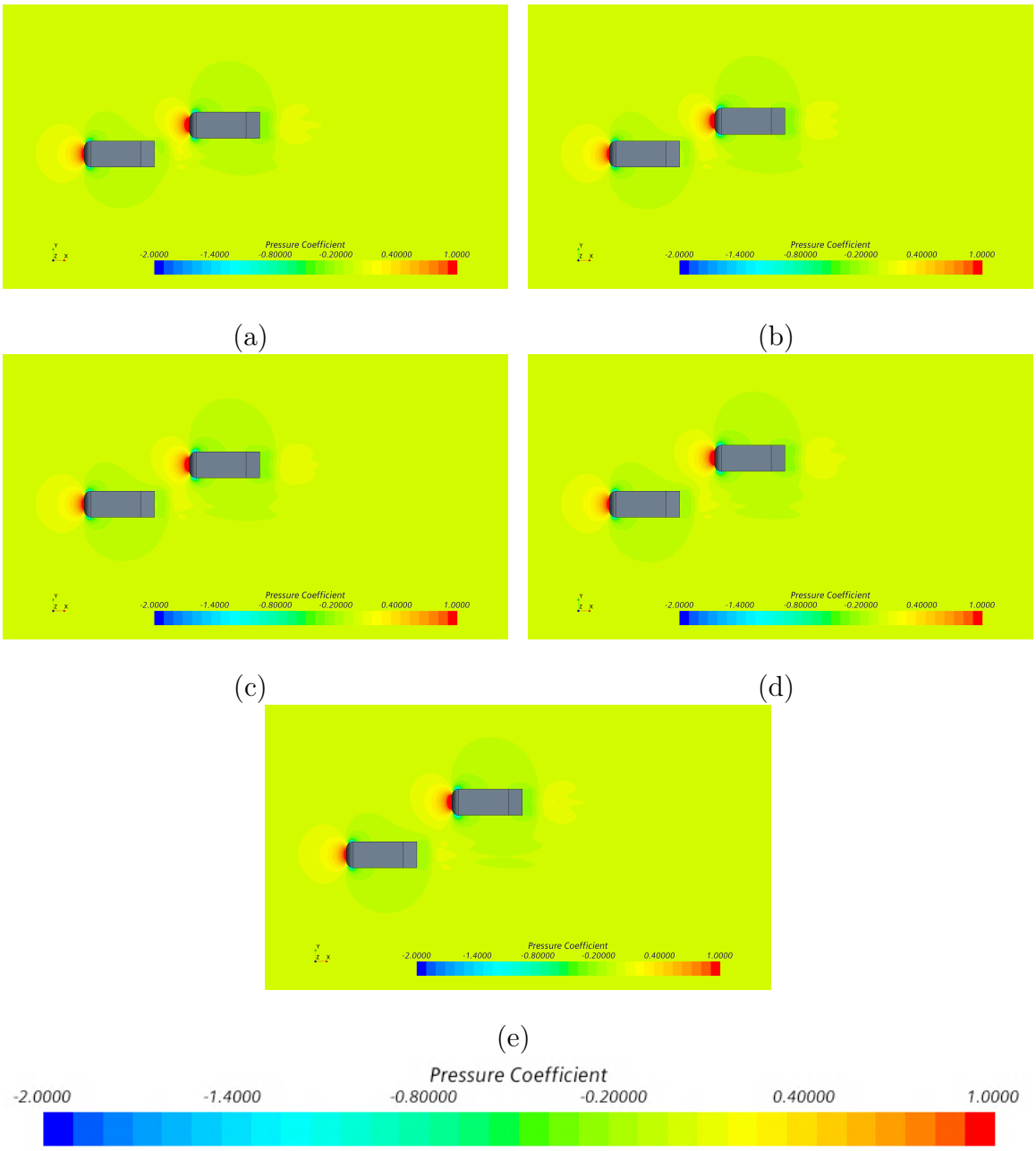

Figure 4.28: Pressure distributions along the two vehicle heterogeneous system at x/L=-0.5 for (a) W*=0.10, (b) W*=0.25, (c) W*=0.50, (d) W*=0.75, and (e) W*=1.0

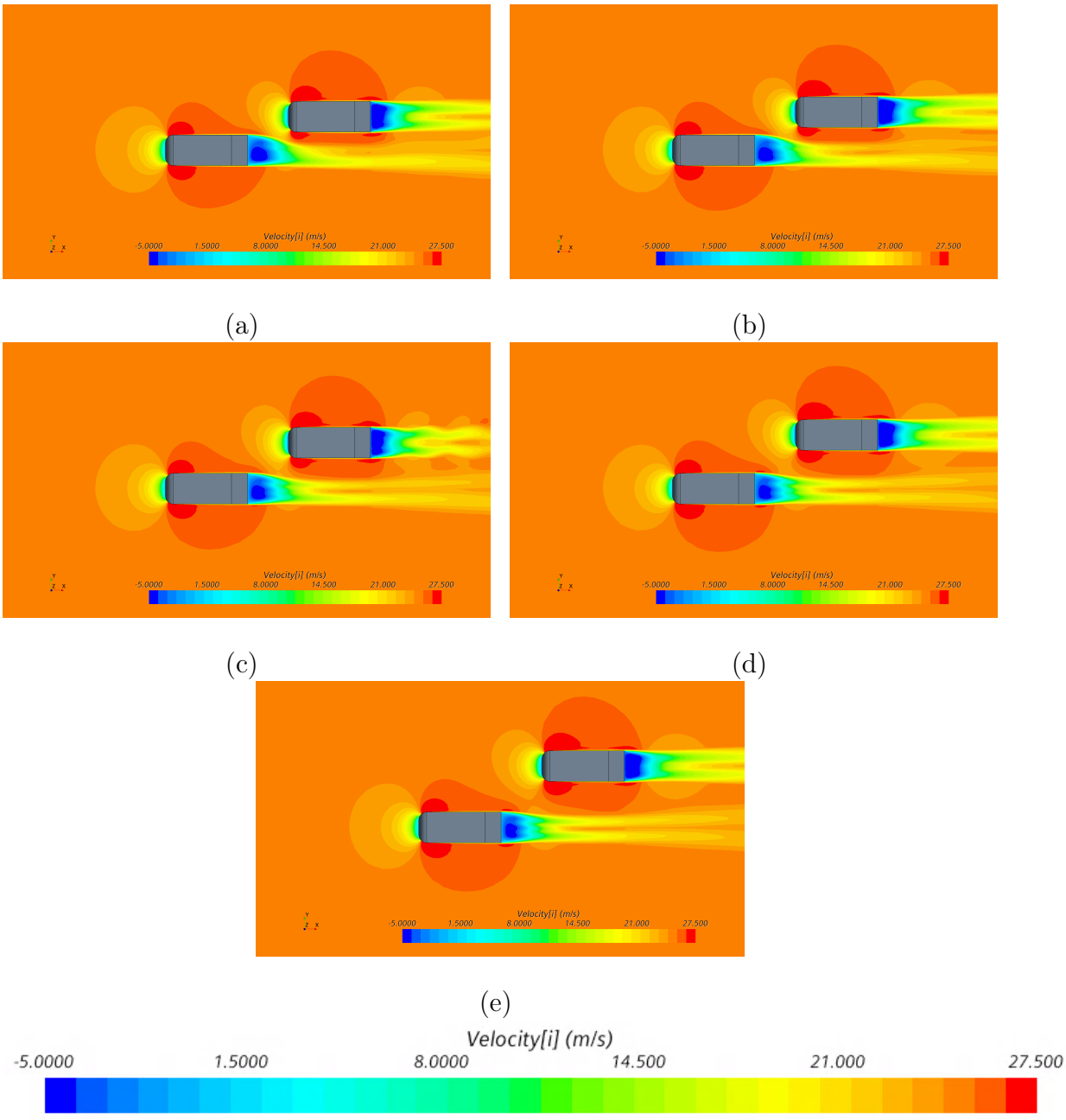

Figure 4.29: Vx distributions along the two vehicle homogeneous system at x/L=-0.5 for (a) W*=0.10, (b) W*=0.25, (c) W*=0.50, (d) W*=0.75, and (e) W*=1.0

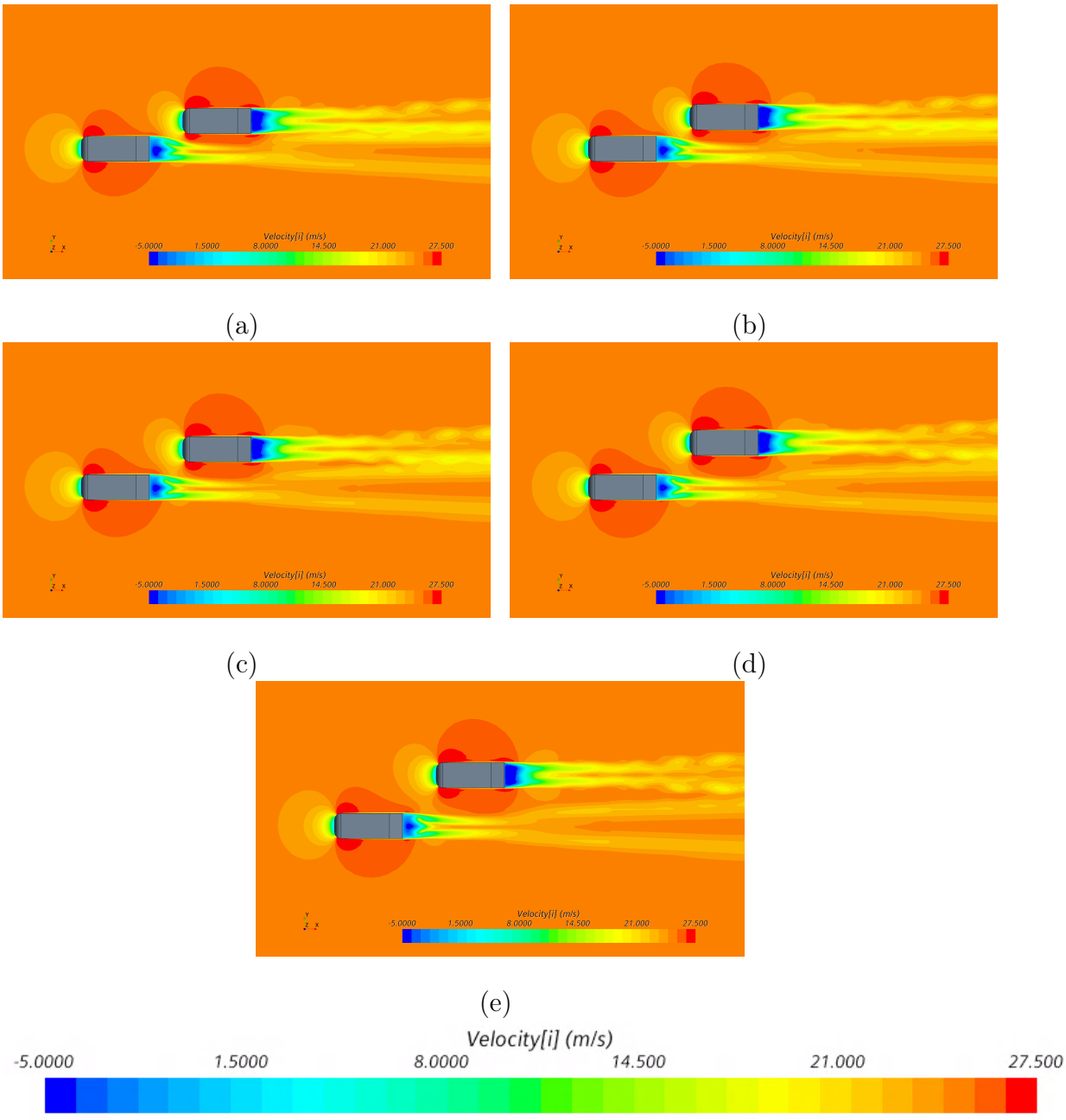

Figure 4.30: Vx distributions along the two vehicle heterogeneous system at x/L=-0.5 for (a) W*=0.10, (b) W*=0.25, (c) W*=0.50, (d) W*=0.75, and (e) W*=1.0

Figures 4.29 and 4.30 show the distribution of Vx along the top view of the two vehicle homogeneous and heterogeneous systems respectively at x/L=-0.5. At this position, the overtaking vehicle is heavily suppressing the wake region of the overtaken vehicle due to which the overtaking vehicle experiences a massive loss in the x-component of velocity. This loss in velocity is greater when the overtaking vehicle is closest to the overtaken vehicle along the transverse axis. A local minimum is observed at this location in the drag coefficient of the overtaken vehicle as can be seen in Figure 4.4. This local minimum was also observed by Noger et al. [13] in their experimental studies validating the results of the CFD.

At x/L=-0.5, the side force coefficient and the yawing moment coefficient of both overtaking and overtaken bodies begin their rise and descent to reach peak maximum and minimum values. This change in value of both the side force and yawing moment coefficients can be attributed to rise in the y-component of velocity caused due to the region of high pressure in the space between the two bodies exerting a force on both bodies in opposite directions. The distribution of Vy for the homogeneous and heterogeneous sets of simulations can be seen in Figures 4.31 and 4.32 respectively. These effects on the side force coefficient and the yawing moment coefficient are more significant at close proximity as compared to the cases with a larger traverse spacing.

A similar trend is observed on the distribution of the z-component of the velocity. An increase in the z-component of velocity is also observed to due the high pressure region between the bodies along with an increase in Vy. This increase in velocity in the z-direction explains the rise in the rolling moment coefficient of the overtaken vehicle at this position causing an outward rolling motion away from the overtaking vehicle. An opposite reaction is observed on the overtaking vehicle. It is also interesting to notice that the change in the velocity component in z-direction for the heterogeneous simulations is slightly more than that of homogeneous simulations.

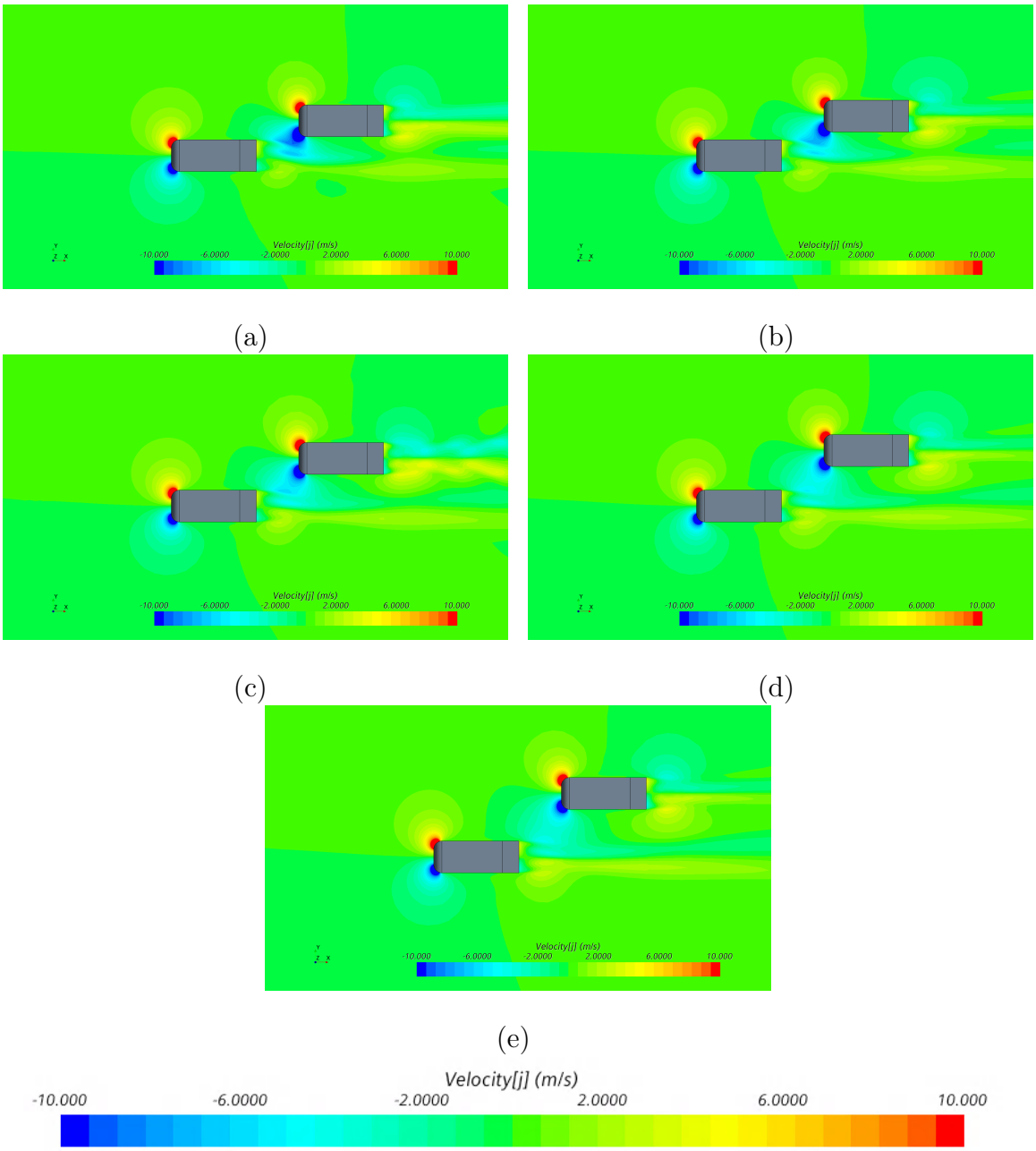

Figure 4.31: Vy distributions along the two vehicle homogeneous system at x/L=-0.5 for (a) W*=0.10, (b) W*=0.25, (c) W*=0.50, (d) W*=0.75, and (e) W*=1.0

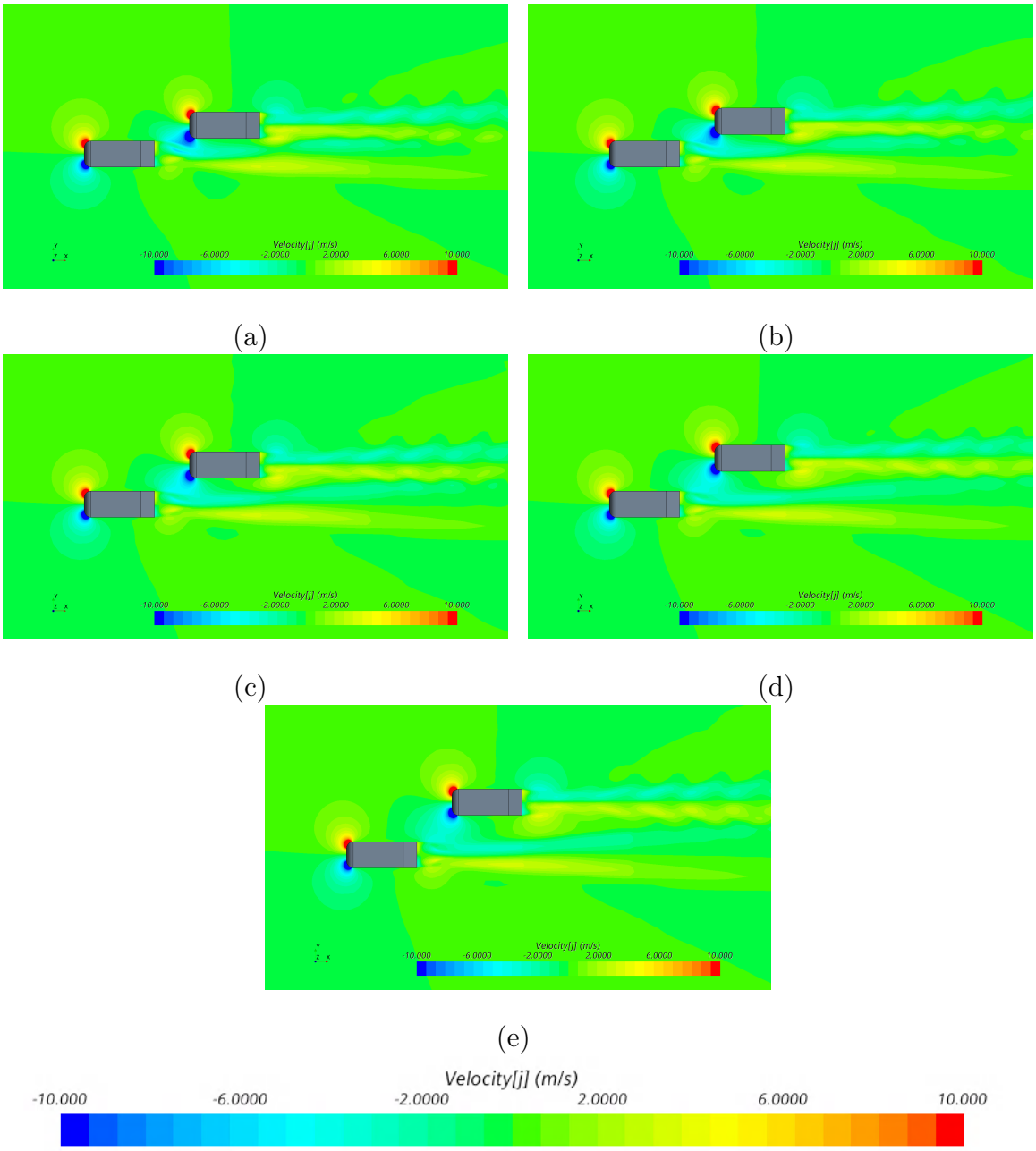

Figure 4.32: Vy distributions along the two vehicle heterogeneous system at x/L=-0.5 for (a) W*=0.10, (b) W*=0.25, (c) W*=0.50, (d) W*=0.75, and (e) W*=1.0

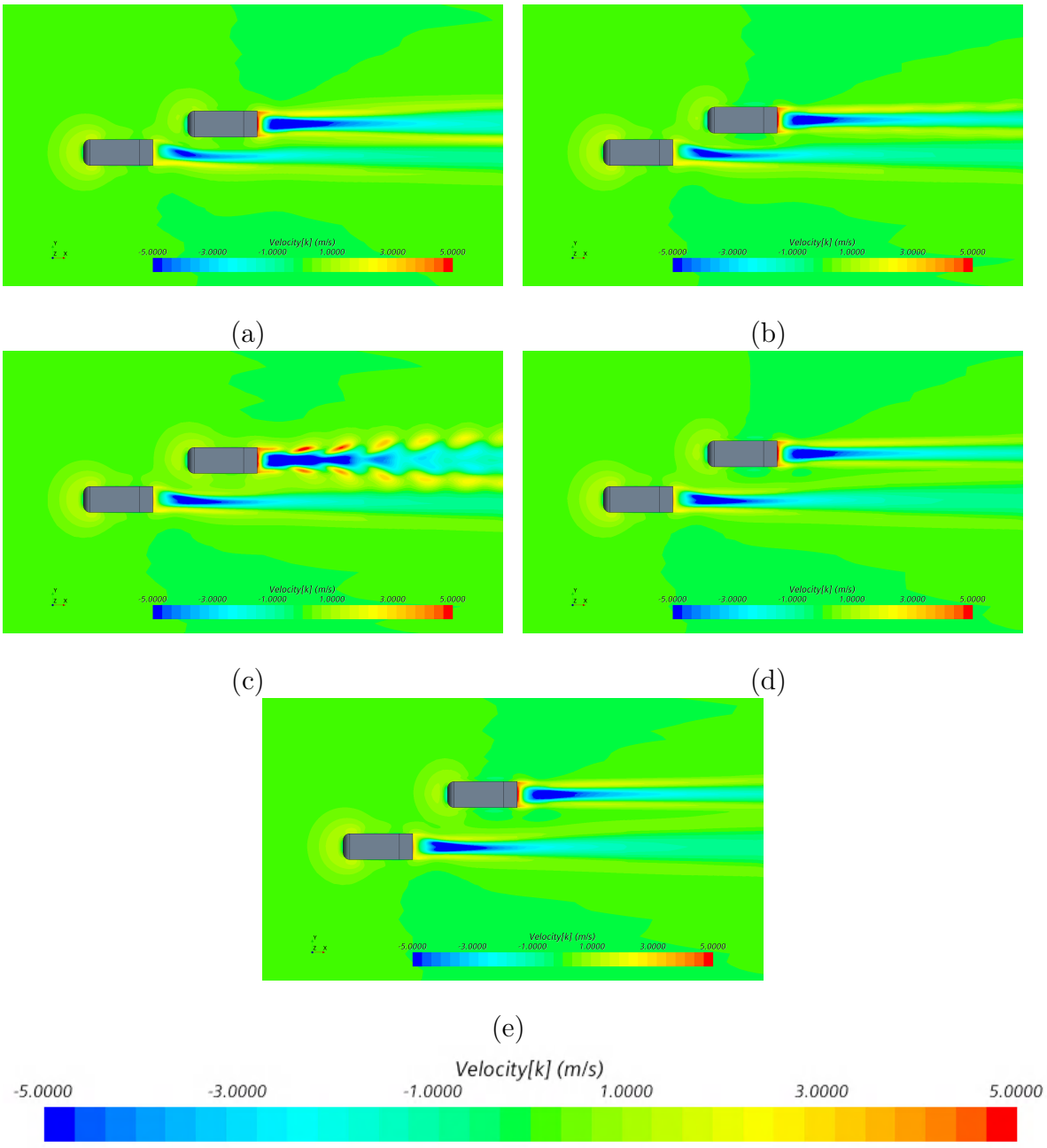

Figure 4.33: Vz distributions along the two vehicle homogeneous system at x/L=-0.5 for (a) W*=0.10, (b) W*=0.25, (c) W*=0.50, (d) W*=0.75, and (e) W*=1.0

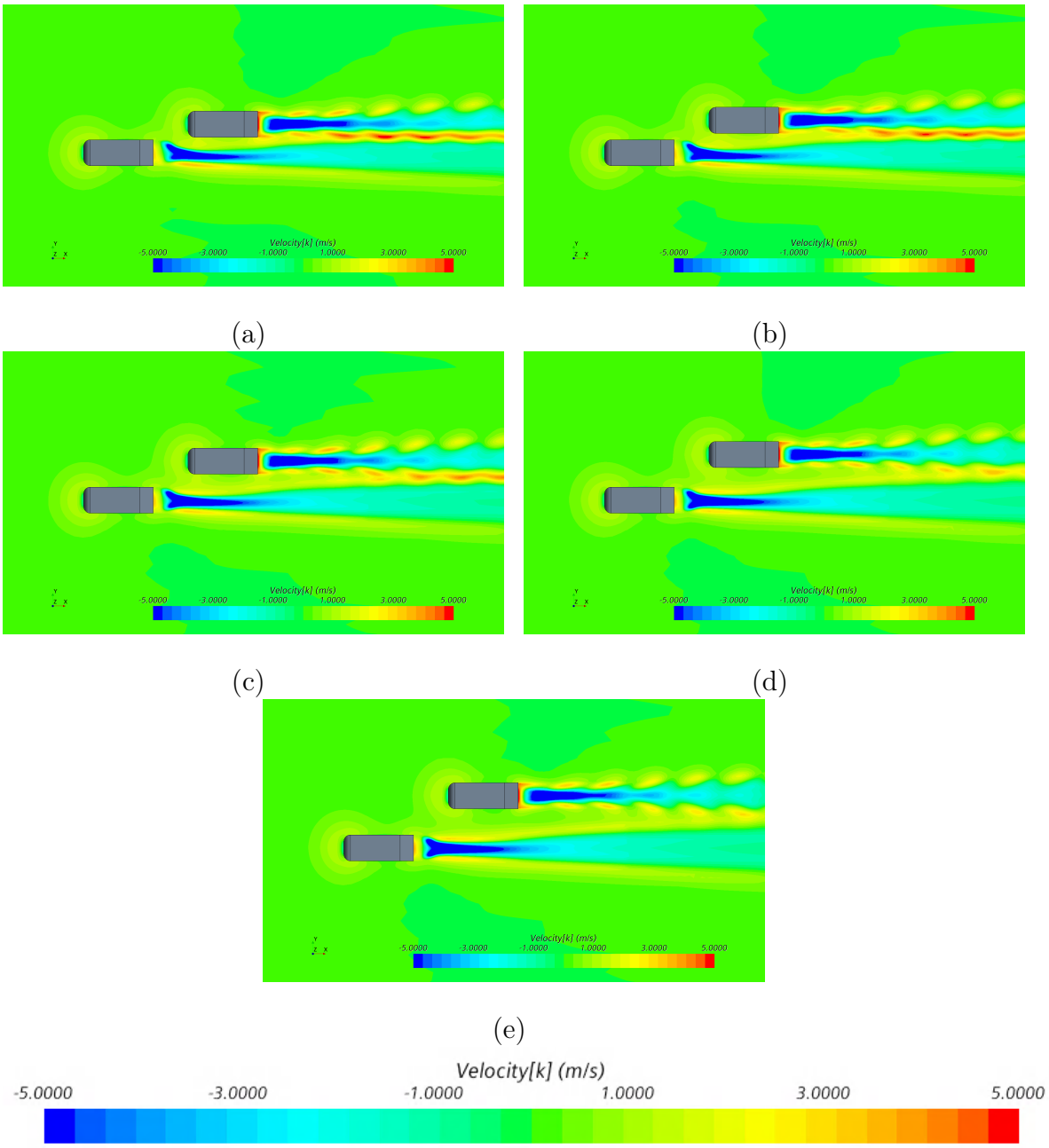

Figure 4.34: Vz distributions along the two vehicle heterogeneous system at x/L=-0.5 for (a) W*=0.10, (b) W*=0.25, (c) W*=0.50, (d) W*=0.75, and (e) W*=1.0

4.5 x/L from -0.5 to 0

As the overtaking vehicle traverses from -0.5L to 0L, significant changes in the aerodynamic force and moment coefficients were observed. As the overtaking vehicle moves forward from -0.5L, the value of the drag coefficient of the overtaken vehicle starts rising sharply from the local minimum while that of the overtaking vehicle starts dropping rapidly to reach a negative peak. At roughly -0.25L, the values of drag coefficient of both overtaking and overtaken vehicle were equal for all sets of simulations. As the nose of the overtaking vehicle drew closer to the tail of the overtaken vehicle, the region of high pressure at the nose of the overtaking vehicle began interacting with the side surface of the overtaken vehicle itself and not just with the wake region behind it anymore. At this point, the overtaken vehicle acted as a solid wall thereby suppressing the high pressure region in front of the overtaking vehicle. This suppression of the high pressure region continued until the nose of the overtaking vehicle was in line with the rear of the overtaken vehicle as can be seen in Figures 4.35 and 4.36 respectively for the homogeneous and heterogeneous set of simulations.

A significant change in the profile of the x-component of velocity can also be observed at this point (figures 4.37 and 4.38). When the overtaking vehicle reaches 0L, the high pressure region at the front of the overtaking vehicle slowly stops interacting with the wake region of the overtaken region while interacting more with the side of the overtaken body itself. This causes the slope of the drag coefficient to fall thereby creating a plateau at after reaching the peak. While the peak values of the drag coefficient of the overtaken body vary inversely with respect to the lateral spacing, it can be seen that the plateaus are also more prominent at close proximity as compared to a larger lateral separation. It is also interesting to note that the plateaus are more prominent in the heterogeneous simulations with the 25^o Ahmed body as the overtaken geometry as compared to a 25^o Ahmed body geometry.

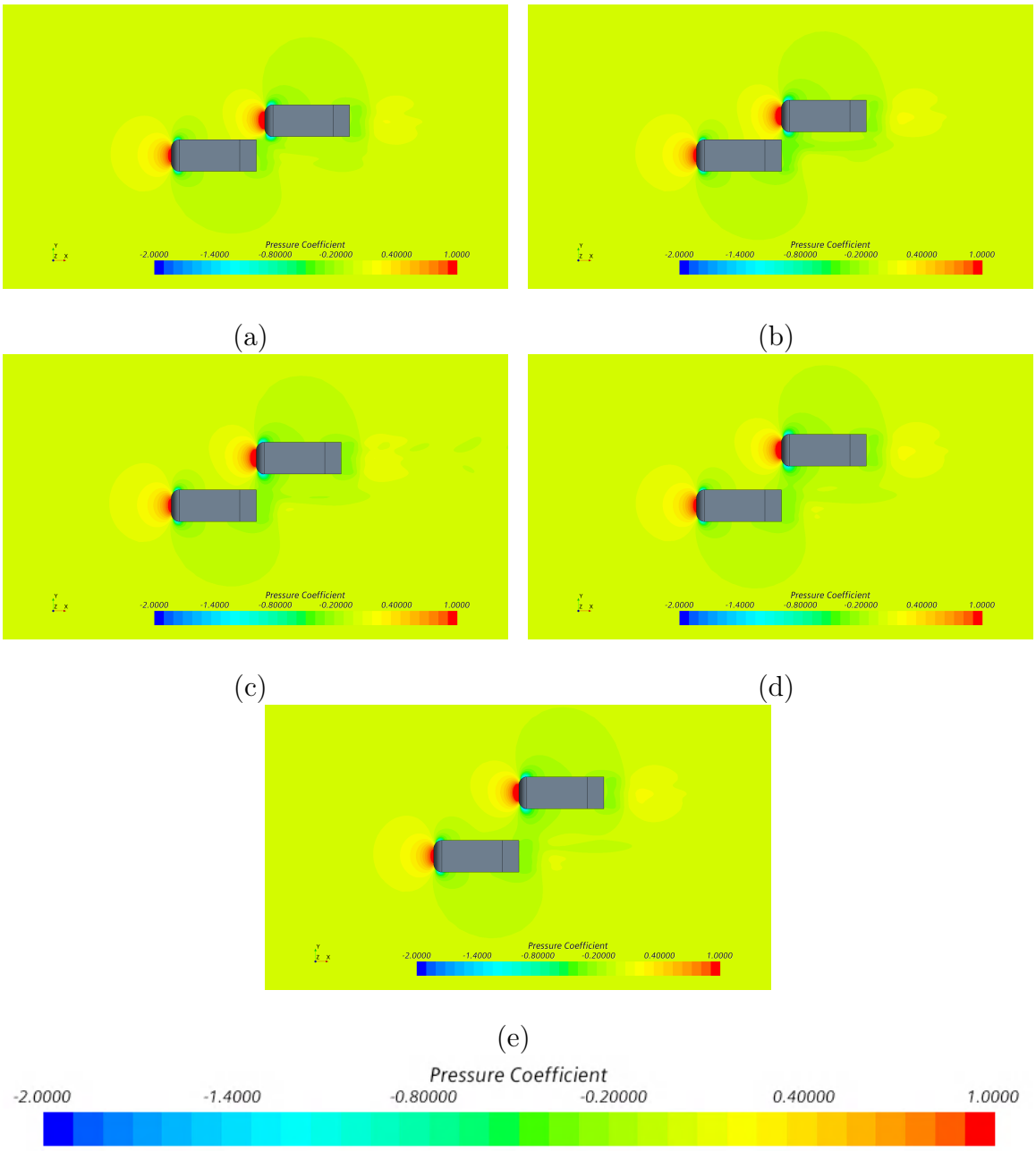

Figure 4.35: Pressure distributions along the two vehicle homogeneous system at x/L=0 for (a) W*=0.10, (b) W*=0.25, (c) W*=0.50, (d) W*=0.75, and (e) W*=1.0

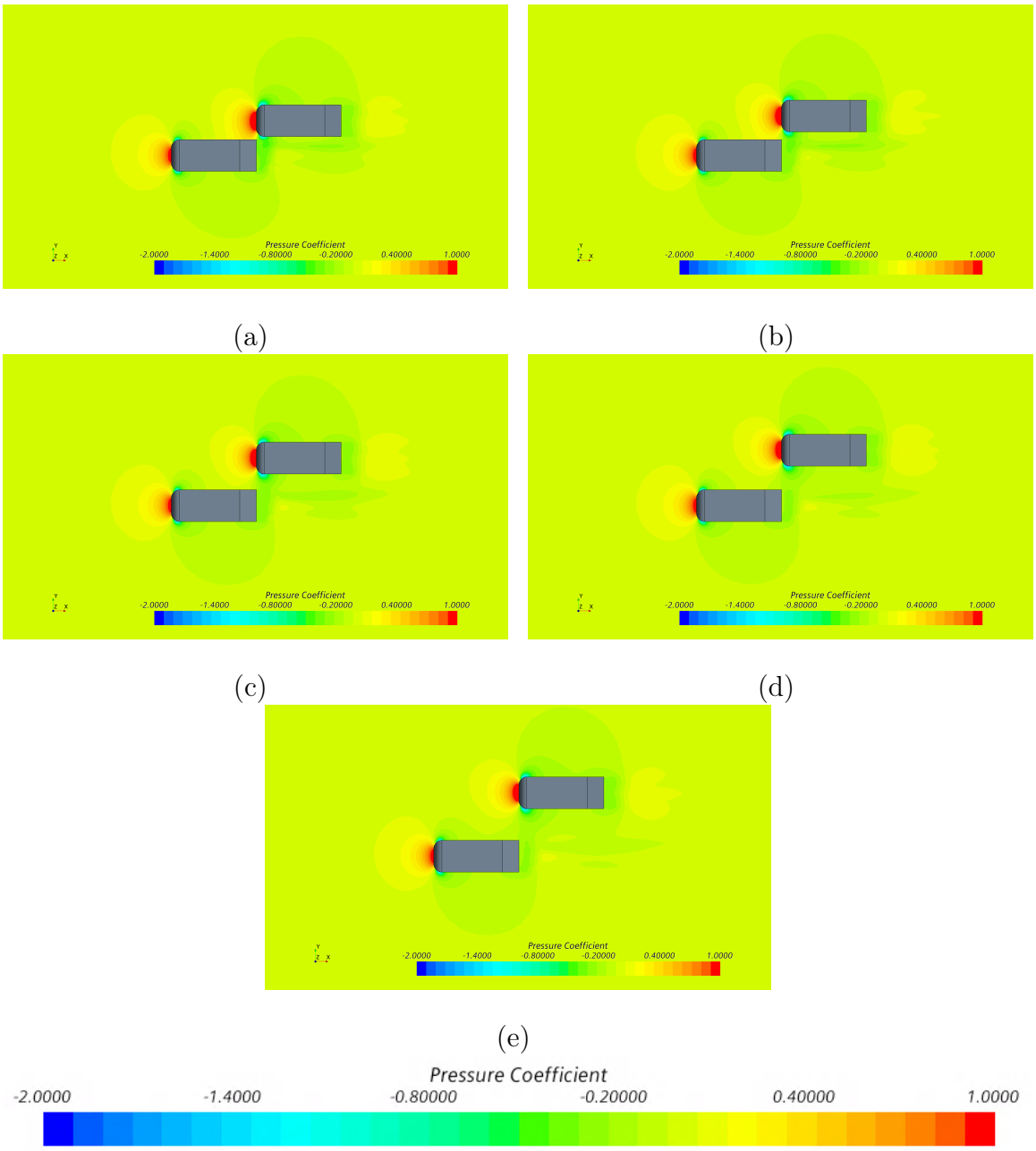

Figure 4.36: Pressure distributions along the two vehicle heterogeneous system at x/L=0 for (a) W*=0.10, (b) W*=0.25, (c) W*=0.50, (d) W*=0.75, and (e) W*=1.0

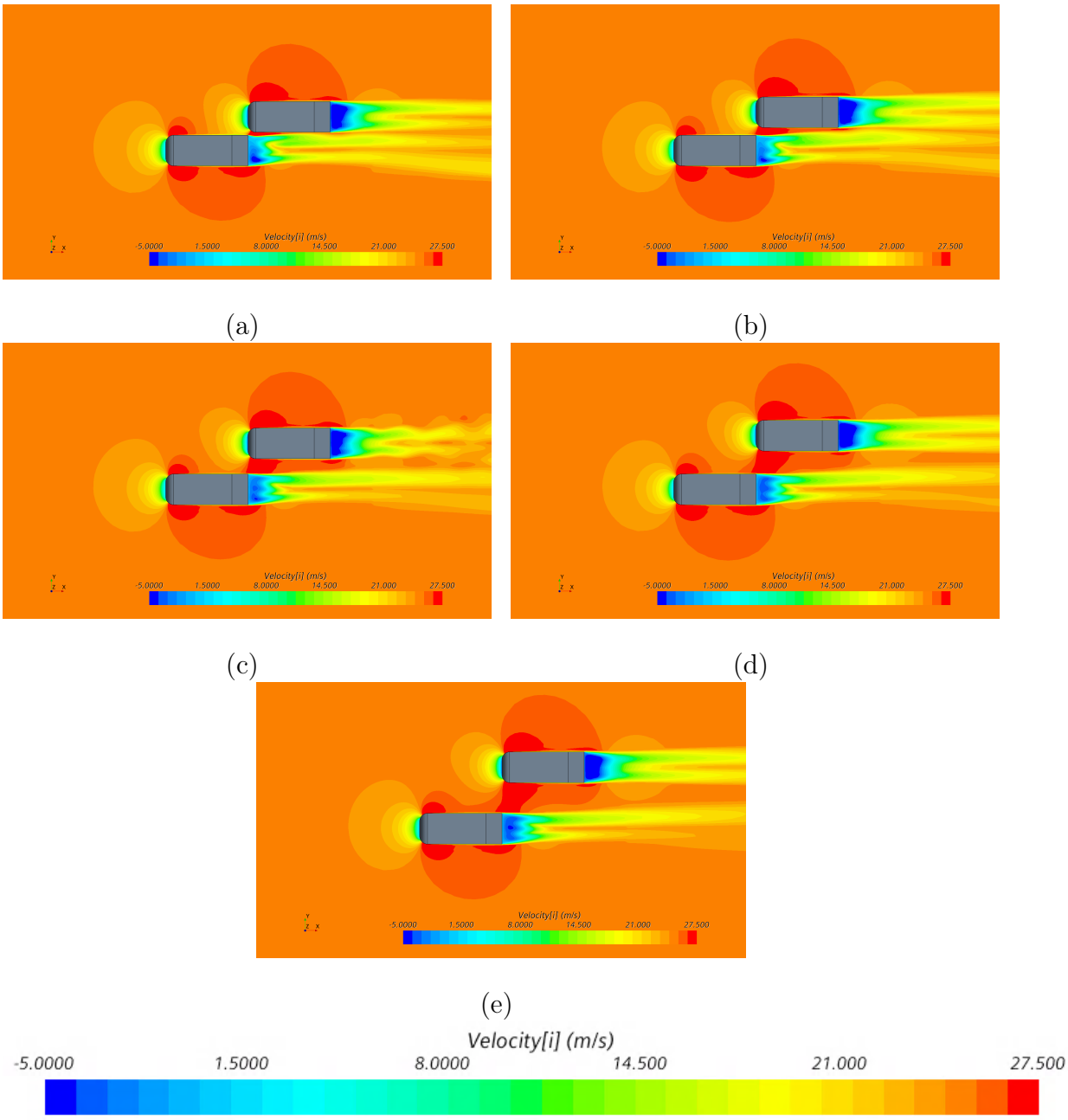

Figure 4.37: Vx distributions along the two vehicle homogeneous system at x/L=0 for (a) W*=0.10, (b) W*=0.25, (c) W*=0.50, (d) W*=0.75, and (e) W*=1.0

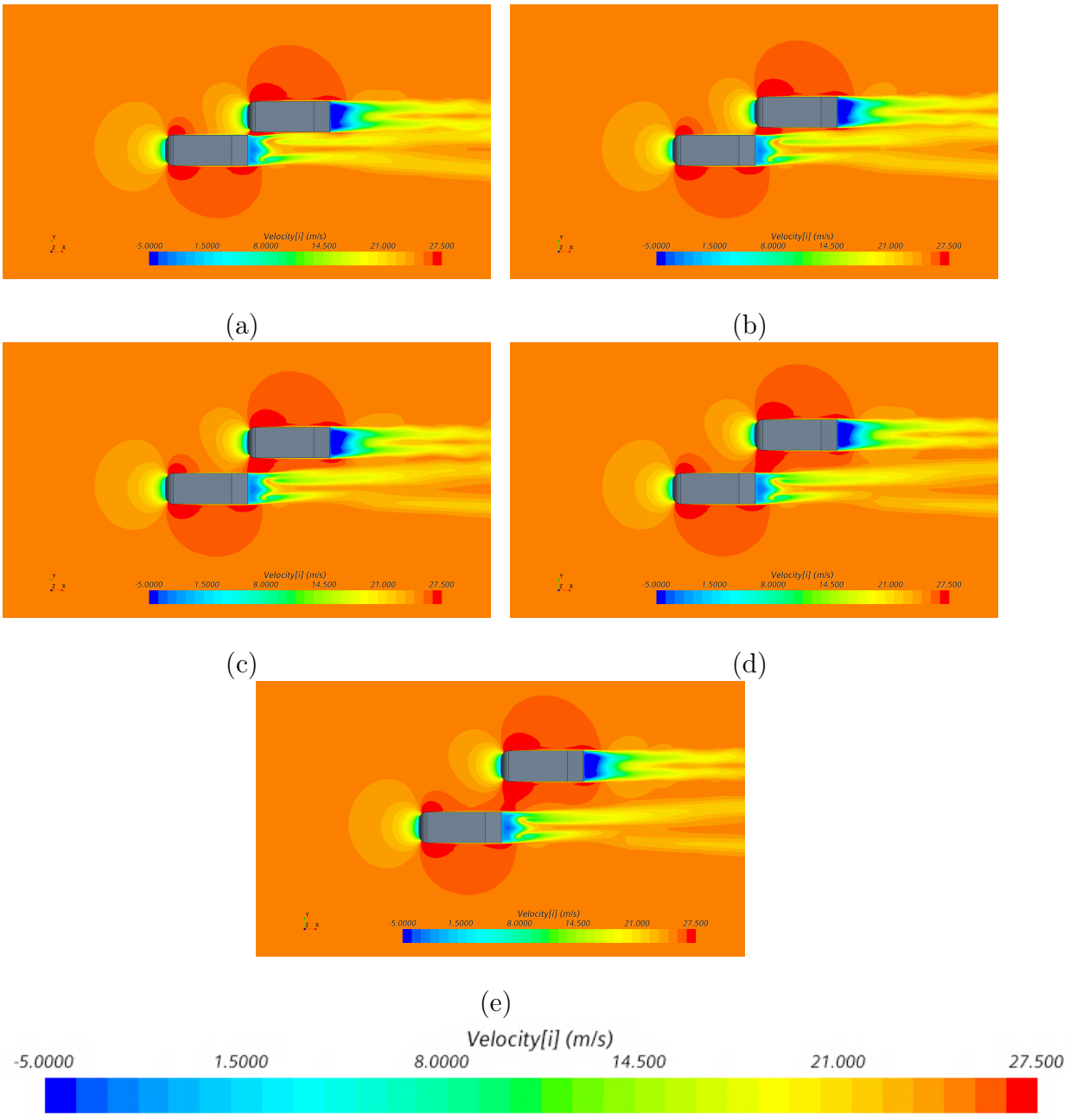

Figure 4.38: Vx distributions along the two vehicle heterogeneous system at x/L=0 for (a) W*=0.10, (b) W*=0.25, (c) W*=0.50, (d) W*=0.75, and (e) W*=1.0

In order to compensate for the significant change in the x-component of velocity, both 'y' and 'z' components of velocity experienced a rise in magnitude at the nose of the overtaking vehicle while the overtaking vehicle traversed from -0.5L to 0L. This can also be attributed to the high pressure region in the space between the cars. This caused a significant drop in the side force coefficient and a minimum peak was observed at a point just after the nose of the overtaking vehicle was in line with the rear of the overtaken vehicle as can be seen in Figure 4.7. An equal and opposite force acts on the overtaking vehicle causing it to reach a positive peak at this location. At 0L, the high pressure region between the two vehicles effectively pushes both vehicles away from each other thereby causing a peak in the yawing moment coefficient of the overtaken vehicle and a negative peak in the yawing moment coefficient of the overtaking vehicle as can be observed in Figures 4.11 and 4.12 respectively. The magnitude of the peaks of both the side force coefficient and the yawing moment coefficient increase with decreasing lateral spacing. The trends in the behavior of both side force coefficient and the yawing moment coefficient of both bodies are very similar for both homogeneous and heterogeneous set of simulations although a higher magnitude of the the y-component of velocity can be observed for the heterogeneous simulations as can be seen in Figures 4.39 and4.40. A very similar pattern is observed for the z-component of velocity (Figures 4.41 and 4.42). A rise in magnitude of velocity in z-direction is observed to compensate for the change in the x-component of velocity as the overtaking vehicle traverses to the 0L mark. This rise in Vz is more prominent in the heterogeneous set of simulations with 35^o Ahmed body as the overtaken vehicle. Also, a peak in the rolling moment coefficient of overtaken vehicle is observed right after the nose of the overtaking vehicle passes beyond the rear of the overtaken vehicle which can be attributed to the increase in the z-component of velocity.

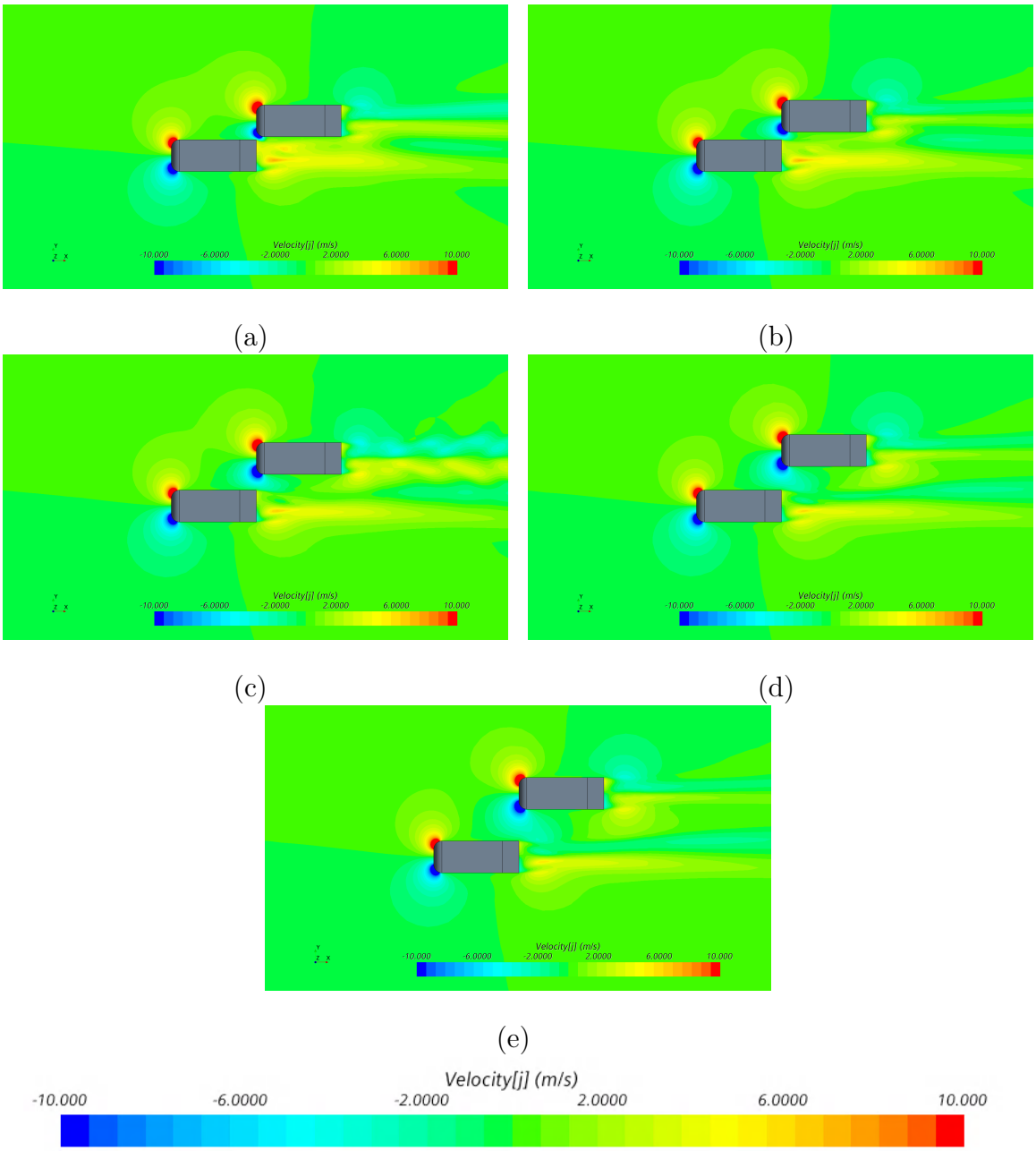

Figure 4.39: Vy distributions along the two vehicle homogeneous system at x/L=0 for (a) W*=0.10, (b) W*=0.25, (c) W*=0.50, (d) W*=0.75, and (e) W*=1.0

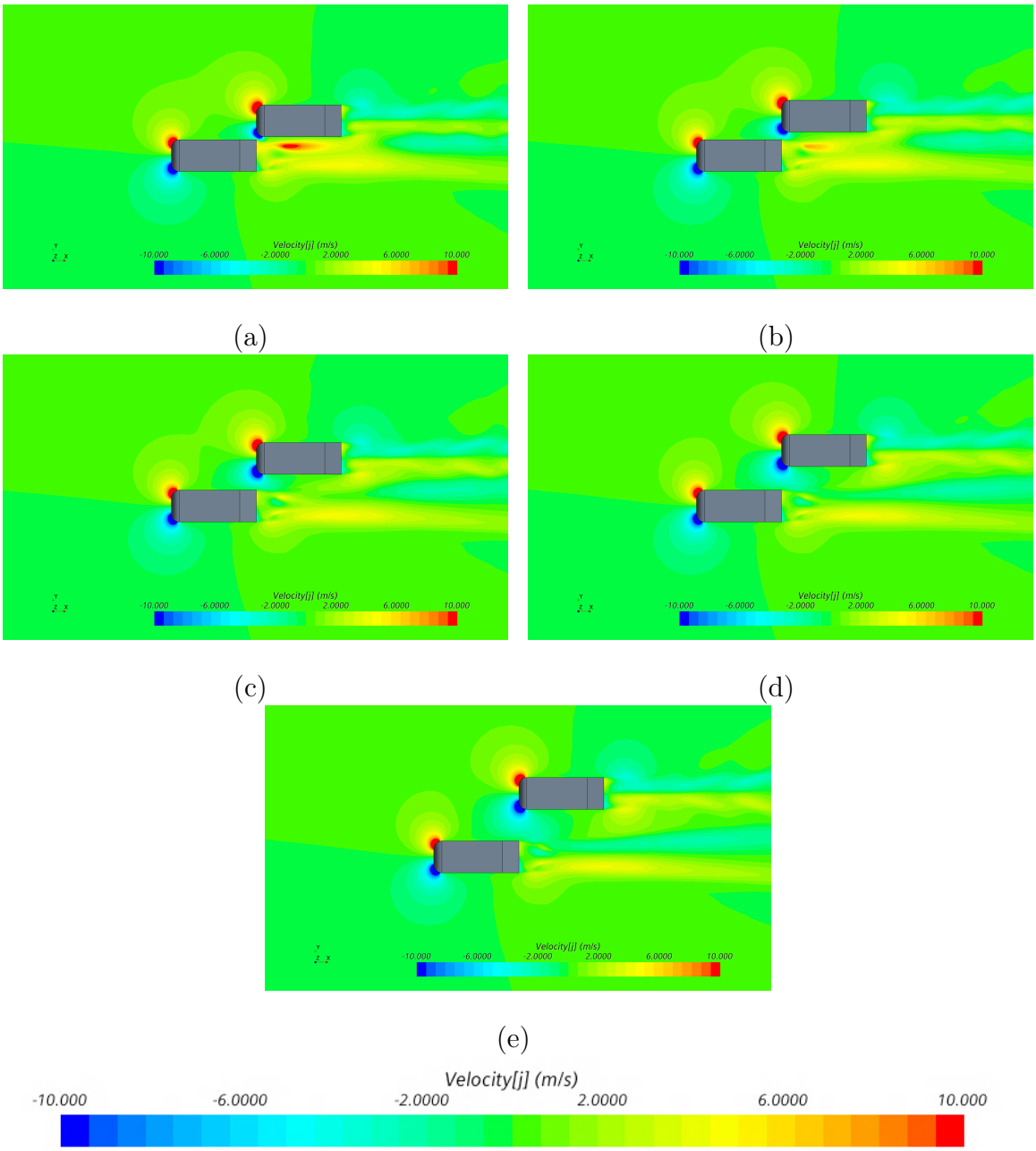

Figure 4.40: Vy distributions along the two vehicle heterogeneous system at x/L=0 for (a) W*=0.10, (b) W*=0.25, (c) W*=0.50, (d) W*=0.75, and (e) W*=1.0

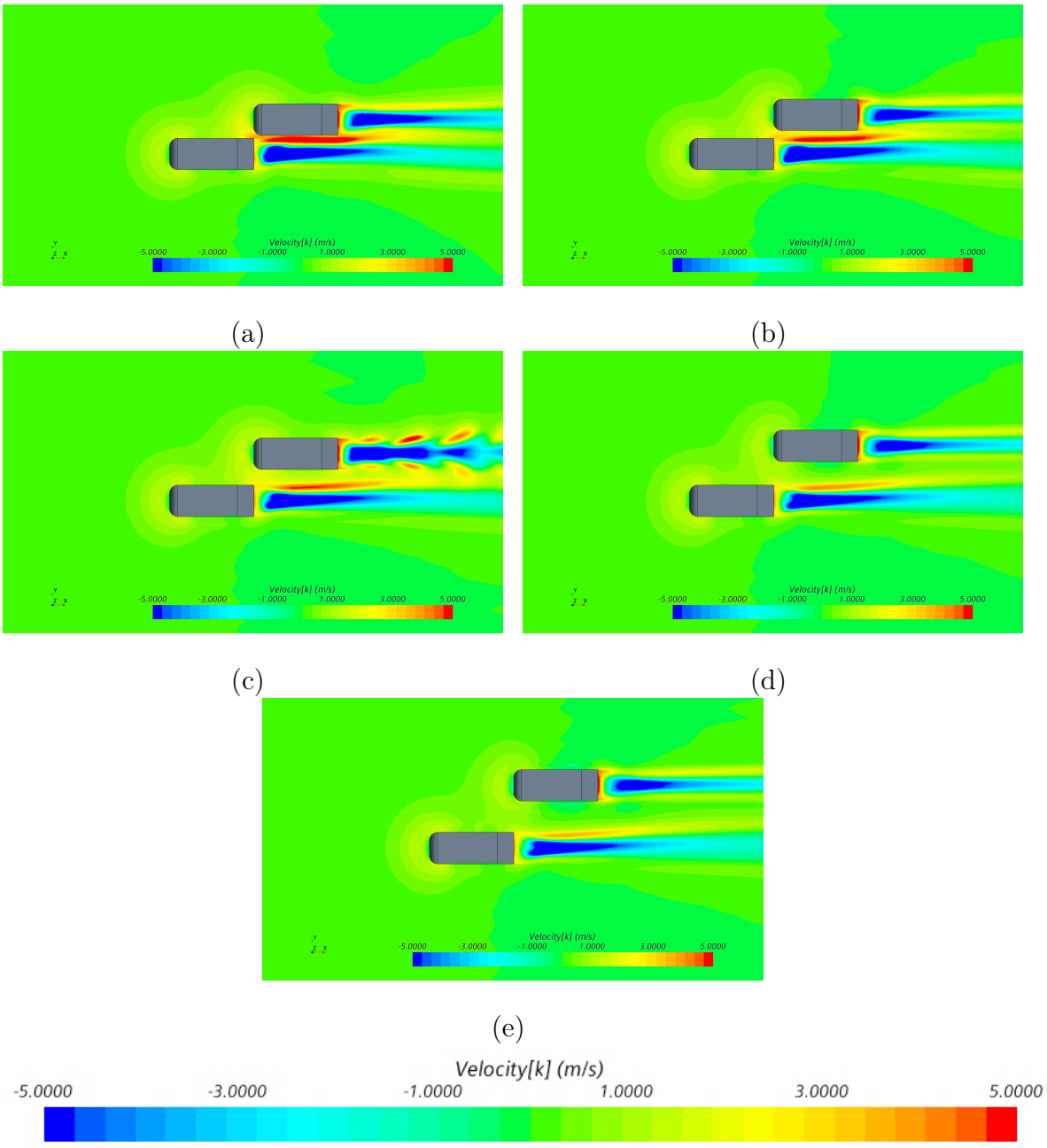

Figure 4.41: Vz distributions along the two vehicle homogeneous system at x/L=0 for (a) W*=0.10, (b) W*=0.25, (c) W*=0.50, (d) W*=0.75, and (e) W*=1.0

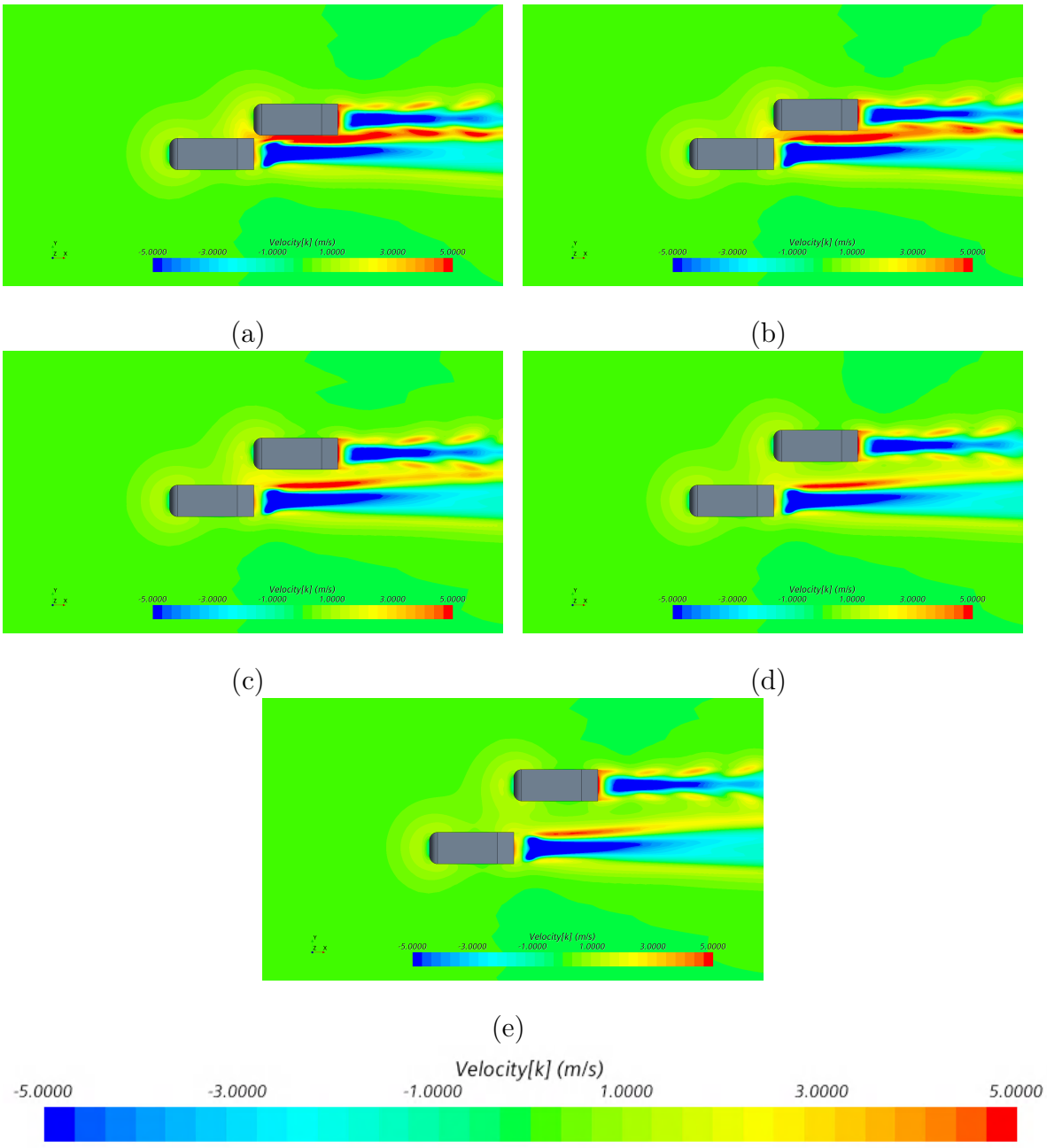

Figure 4.42: Vz distributions along the two vehicle heterogeneous system at x/L=0 for (a) W*=0.10, (b) W*=0.25, (c) W*=0.50, (d) W*=0.75, and (e) W*=1.0

4.6 x/L from 0 to 1

As the overtaking vehicle moves beyond 0L, it begins to interact even less and then stops interacting with the low pressure wake region of the overtaken vehicle while it begins interacting more with the low pressure region along the side of the overtaken vehicle and the overtaken body itself. When the overtaking body reaches 0.5L from 0L, the drag coefficient of the overtaken body slowly increase until it reaches a peak value just before 0.5L after which a plateau was observed as discussed previously. At this point, the drag coefficient of the overtaking vehicle experiences a negative peak. The coefficient of drag of the overtaken vehicle at this point begins to drop until it reaches a minimum just before the overtaking vehicle reaches 1.5L. As the overtaking vehicle approaches 1L, the point at which both vehicles are in line, the high pressure region at the nose of the overtaking vehicle begins to interact with the high pressure region at the nose of the overtaken vehicle. Once the two bodies were in line, the high pressure regions at the front of both bodies continued to interact forming a large high pressure bubble at the front of both vehicles. At the rear, the low pressure wake region of both the vehicles seemed to merge into a larger low pressure region as can be seen in figures 4.43 and 4.44 respectively for both homogeneous and heterogeneous simulations. It can be seen that the strength of both the high pressure and low pressure bubbles at the front and rear of both the bodies respectively is considerably high and increases with increase in proximity of the two bodies. As the lateral spacing increase, the strength of the common high and low pressure regions decreases. For lateral spacings of W*=0.75 and W*=1.0, the high pressure region at the front can be seen to split due to the large separation between the two bodies. It is to be noticed that, at this point, the large variations in pressure resulted in an increase in the coefficient of drag values for both the overtaken and the overtaking vehicles as compared a body in isolation for both homogeneous and heterogeneous simulations.

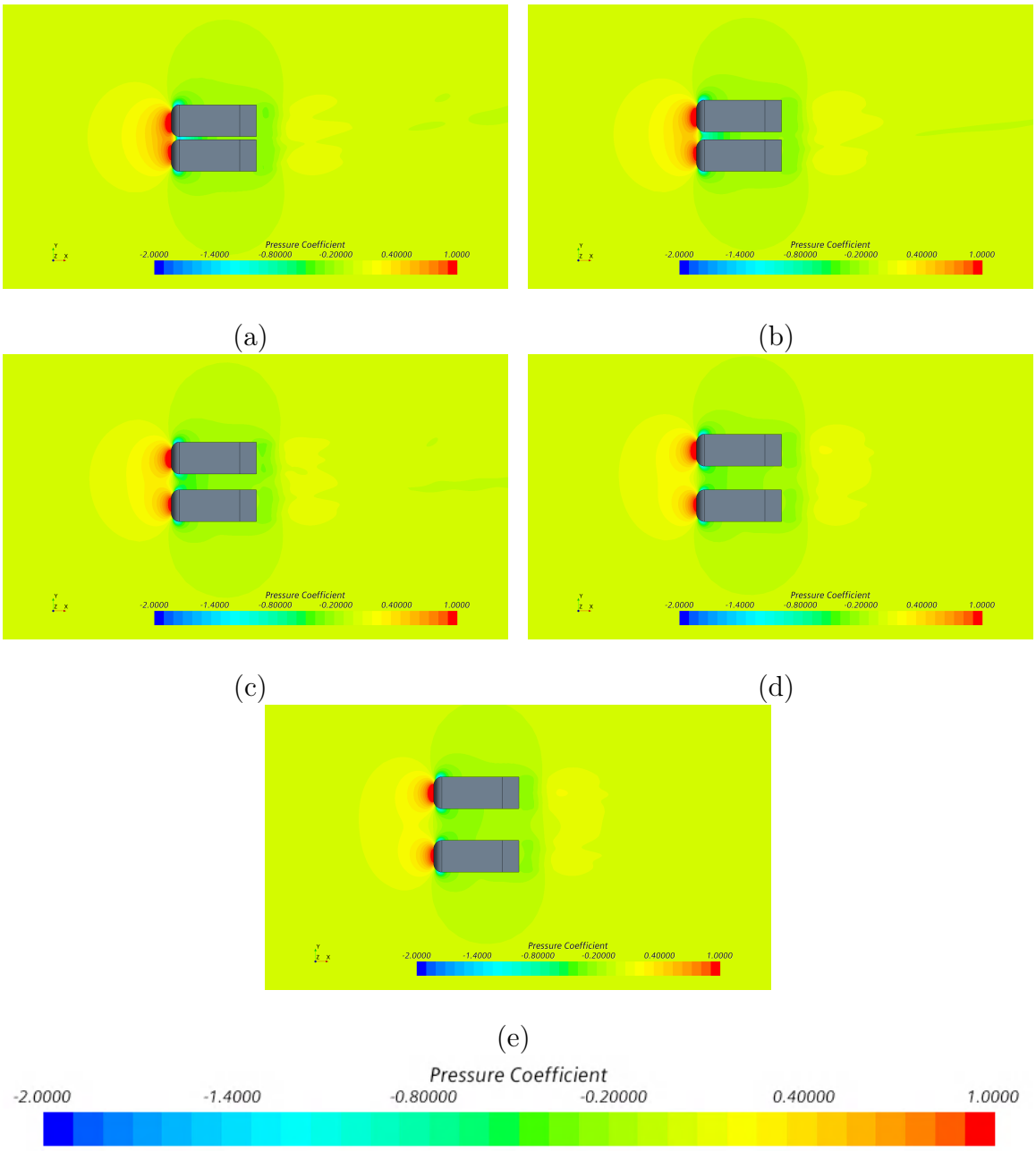

Figure 4.43: Pressure distributions along the two vehicle homogeneous system at x/L=1 for (a) W*=0.10, (b) W*=0.25, (c) W*=0.50, (d) W*=0.75, and (e) W*=1.0

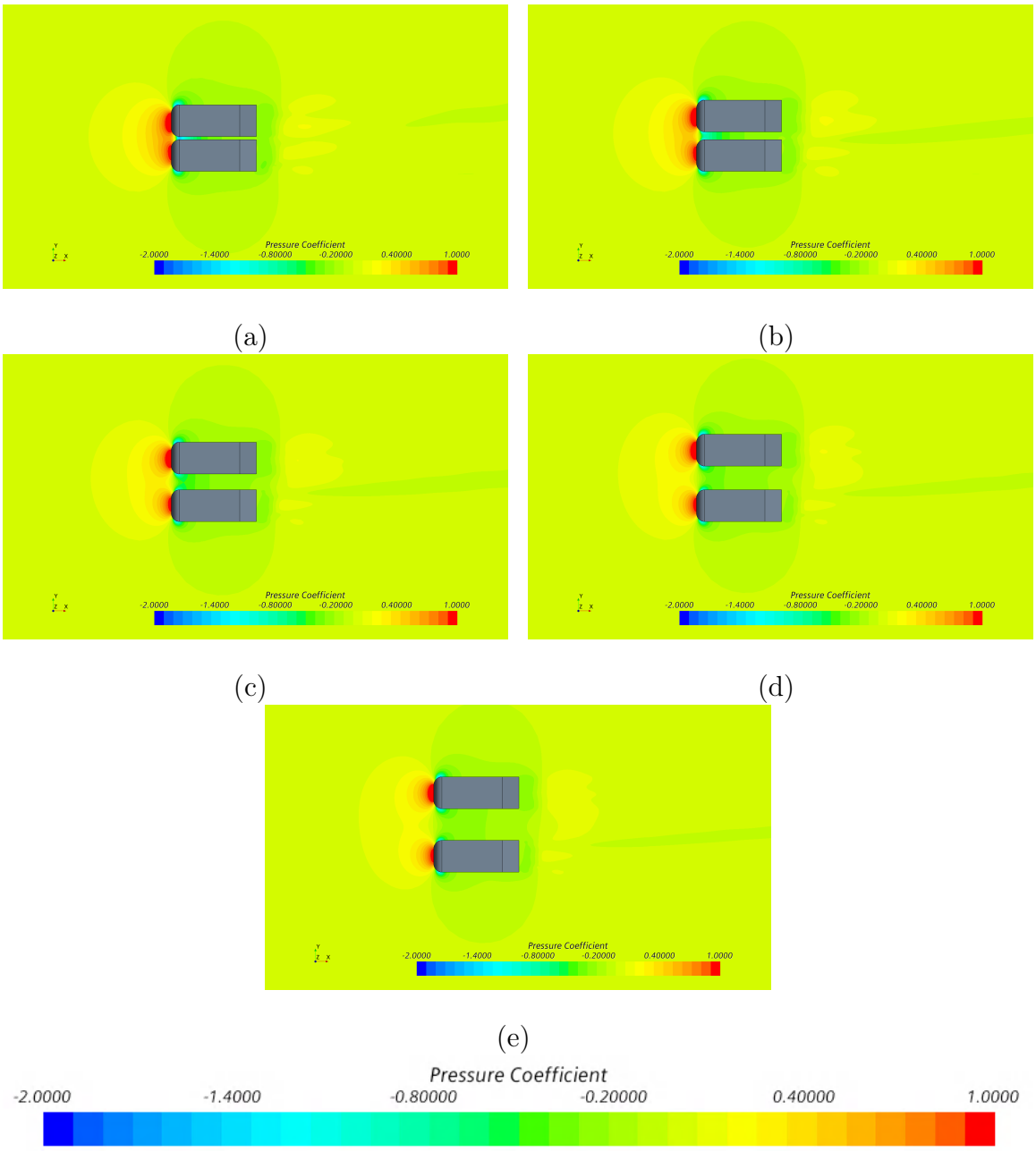

Figure 4.44: Pressure distributions along the two vehicle heterogeneous system at x/L=1 for (a) W*=0.10, (b) W*=0.25, (c) W*=0.50, (d) W*=0.75, and (e) W*=1.0

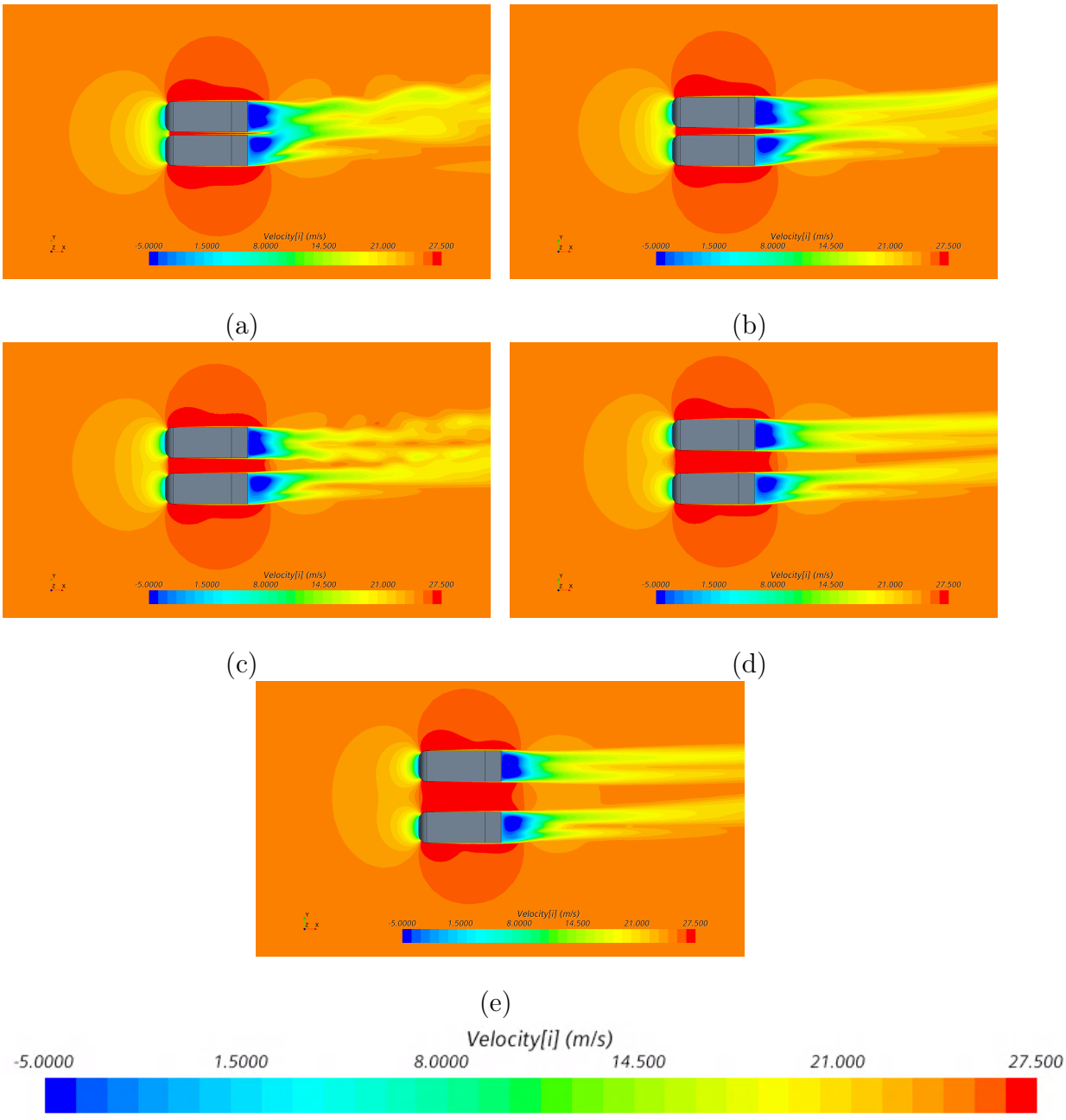

Figure 4.45: Vx distributions along the two vehicle homogeneous system at x/L=1 for (a) W*=0.10, (b) W*=0.25, (c) W*=0.50, (d) W*=0.75, and (e) W*=1.0

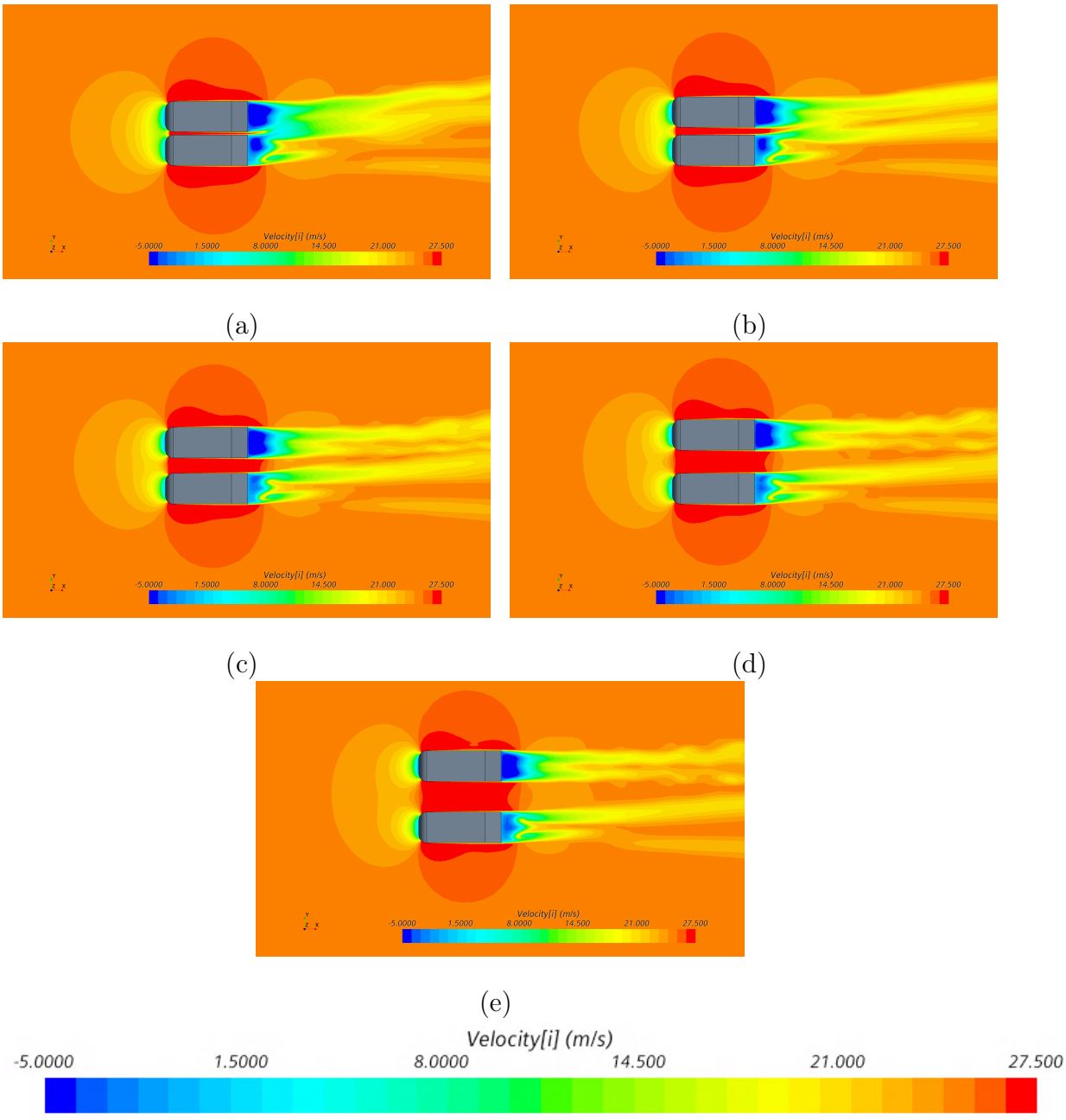

Figure 4.46: Vx distributions along the two vehicle heterogeneous system at x/L=1 for (a) W*=0.10, (b) W*=0.25, (c) W*=0.50, (d) W*=0.75, and (e) W*=1.0

As the overtaking body moves past 0L, the side force coefficients of both the bodies fallback from their universal maximum and minimum values respectively. This sudden increase in the side force coefficient of the overtaken vehicle (Figure 4.7) can be attributed to the lack of interaction of the high pressure region at the front of the overtaking vehicle with the low pressure wake region of the overtaken vehicle. For the overtaking vehicle, the side force coefficient drops sharply from the local maximum as can be seen in Figure 4.8. At approximately 0.5L, the coefficient of side force of both bodies seem to coincide after which the cycle is reversed and a universal maximum is seen for the overtaken vehicle while the overtaking vehicle experiences a universal minimum at 1L. A similar observation can be made with the yawing moment coefficient. The yawing moment coefficient of the overtaken vehicle reaches a universal minimum right after 0L after which it steeply begins to rise while the opposite behavior is observed for the yawing moment coefficient of the overtaking vehicle as can be seen in Figure 4.12. The yawing moment coefficients of both bodies also coincide at 0.5L after which the trends are reversed. As the overtaking vehicle reaches 1L, the yawing moment coefficient of the overtaken vehicle tries to reach a universal maximum while a negative peak is observed for the yawing moment coefficient of the overtaking vehicle. The rolling moment coefficient of the overtaken vehicle also experiences a local minimum at 1L. This can be attributed to the interactions of the pressure field and the velocity fields at the front of the two bodies. Figures 4.45 through 4.50 show the distribution of Vx, Vy, and Vz when the two bodies are inline with each other. When the two bodies are inline, the velocity of the air upstream is slowed down and is funneled through the gap between the two bodies as is evident from the velocity scenes. Figures 4.47 and 4.48 clearly show this phenomenon. It is also interesting to notice that flow patterns in all the velocity scenes at this position when the two vehicles are parallel to each other are perfectly symmetrical about the center-line of the spacing between the two bodies.

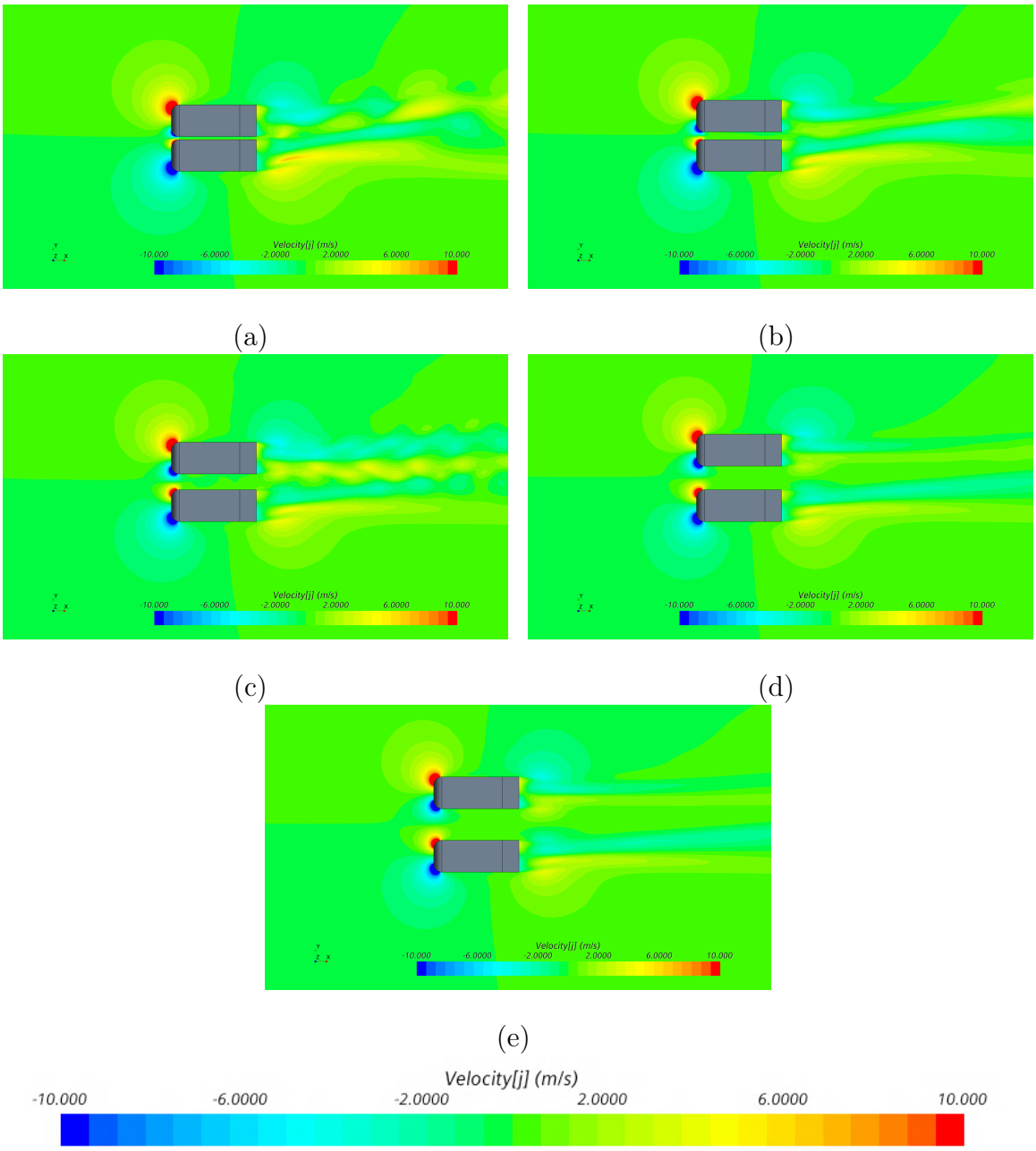

Figure 4.47: Vy distributions along the two vehicle homogeneous system at x/L=1 for (a) W*=0.10, (b) W*=0.25, (c) W*=0.50, (d) W*=0.75, and (e) W*=1.0

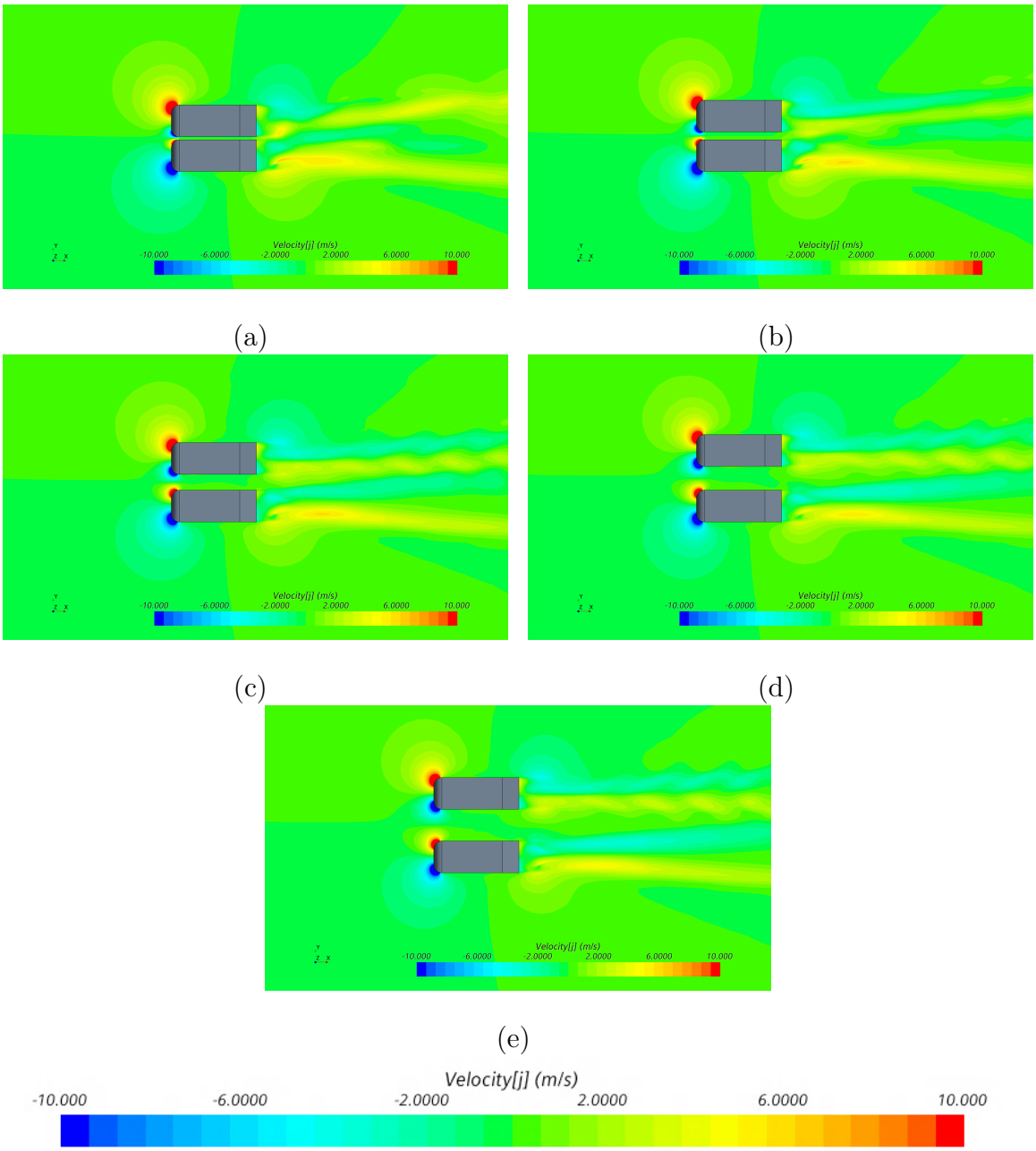

Figure 4.48: Vy distributions along the two vehicle heterogeneous system at x/L=1 for (a) W*=0.10, (b) W*=0.25, (c) W*=0.50, (d) W*=0.75, and (e) W*=1.0

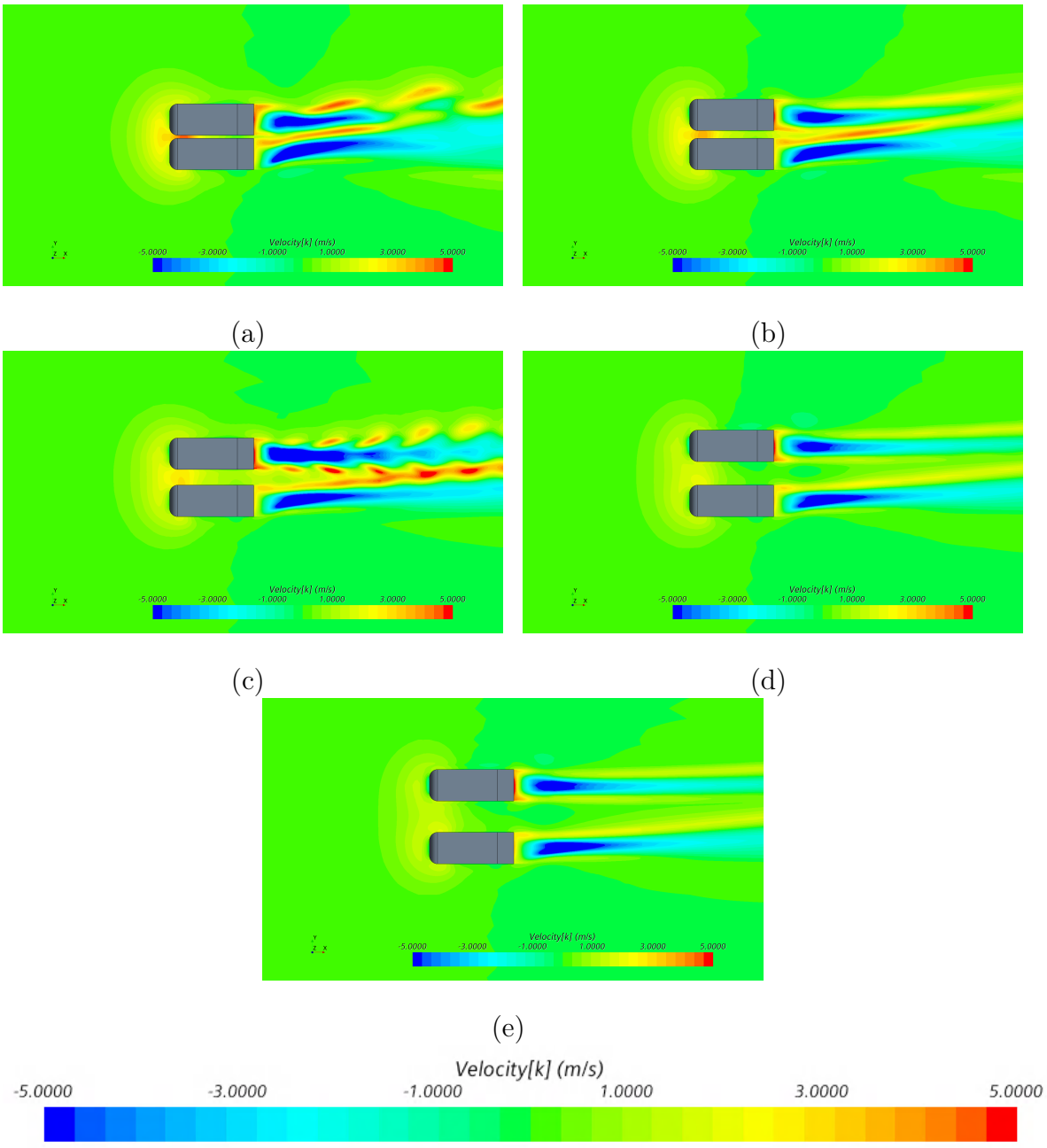

Figure 4.49: Vz distributions along the two vehicle homogeneous system at x/L=1 for (a) W*=0.10, (b) W*=0.25, (c) W*=0.50, (d) W*=0.75, and (e) W*=1.0

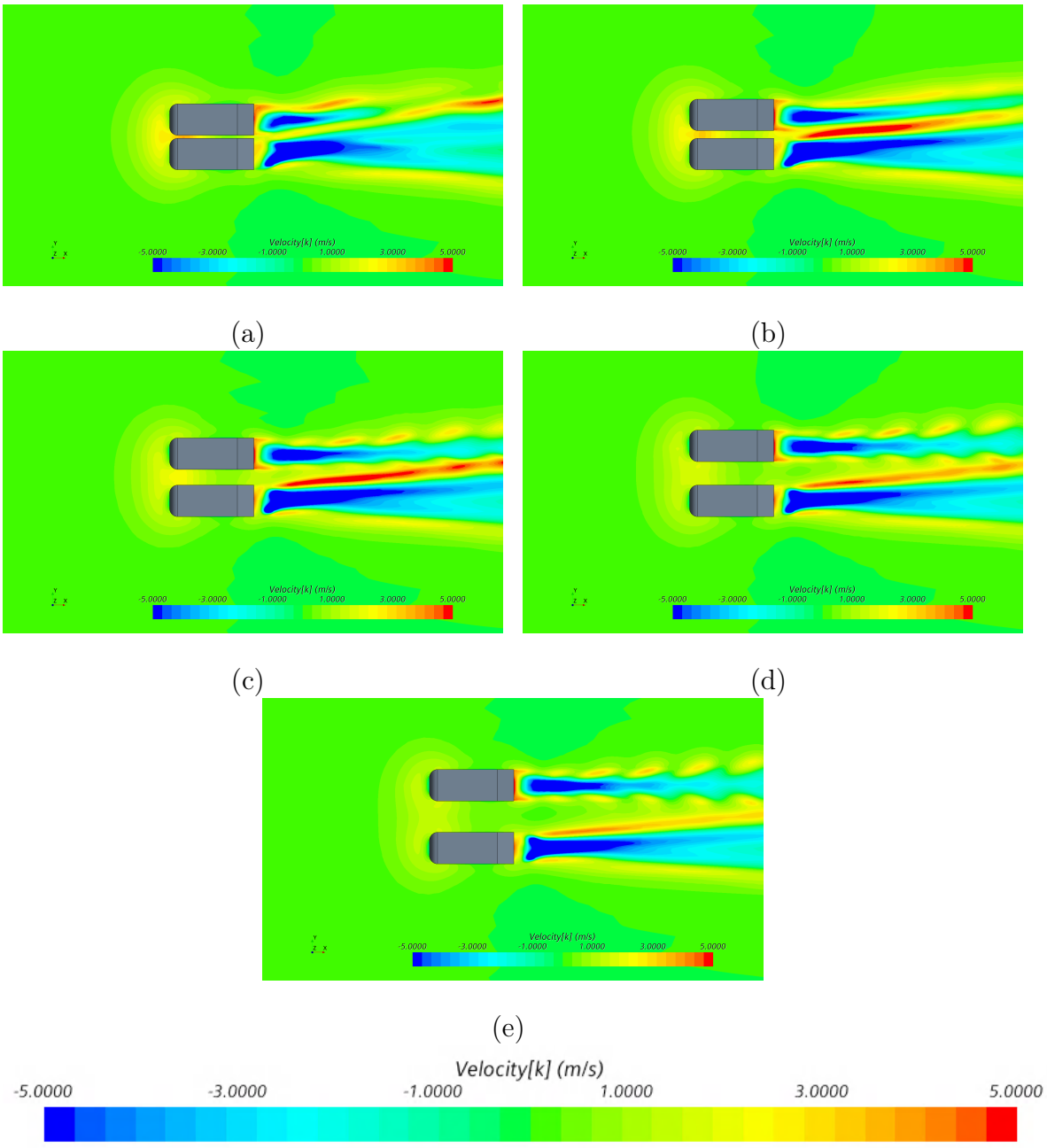

Figure 4.50: Vz distributions along the two vehicle heterogeneous system at x/L=1 for (a) W*=0.10, (b) W*=0.25, (c) W*=0.50, (d) W*=0.75, and (e) W*=1.0

4.7 x/L from 1 to 2

The values of the coefficient of drag of both overtaking and overtaken bodies are equal to each other when the two bodies are parallel to each other at 1L. Following this, the drag o-efficient of the overtaken body continues to fall (which started between 0L and 0.5L) and experience a universal minimum just before the overtaking body reaches 1.5L. The opposite is experience by the overtaking body where it reaches a universal maximum at 1.5L. Beyond this point, the drag coefficient of the overtaken body tends to slowly rise back up all the way up to 2L beyond which it will continue to go back to its original value. The side force coefficient of the overtaken vehicle also rises to a universal maximum at 1.5L beyond which it starts to slowly fall back to its original value. A similar trend is observed in the behavior of the yawing moment coefficient of the overtaken vehicle. Both side force coefficient and the yawing moment coefficient of the overtaken body mirror their results at 1.5L to that of what they experienced at 0.5L. These changes in side force and yawing moment coefficients are attributed to the pressure interactions between the two bodies. At 0.5L, although the high pressure regions at the front of the two bodies still interact with each other, the low pressure region along the side of the moving overtaking vehicle passes alongside the nose of the overtaken vehicle contributing to the sudden variation in side force and yawing moment coefficients. Furthermore, at 2L, when the nose of the overtaken vehicle is inline with the tail of the overtaking vehicle, a universal maximum is experienced by the side force coefficient and the yawing moment coefficient of the overtaking body. This can be attributed to the interaction of the high pressure region at the nose of the overtaken vehicle with the low pressure wake region at the rear of the overtaking vehicle as can be seen in Figures 4.51 and 4.52.

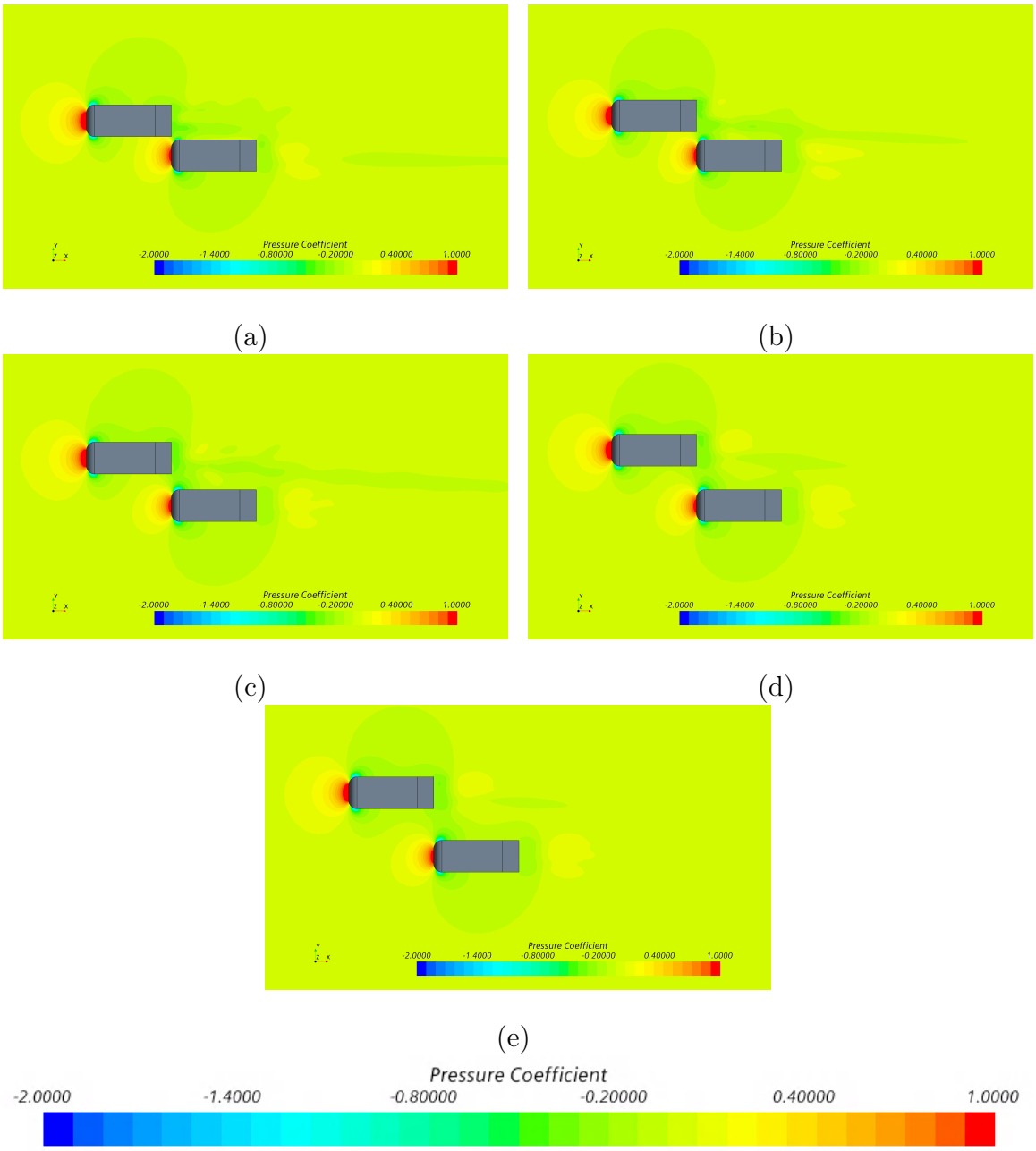

Figure 4.51: Pressure distributions along the two vehicle homogeneous system at x/L=2 for (a) W*=0.10, (b) W*=0.25, (c) W*=0.50, (d) W*=0.75, and (e) W*=1.0

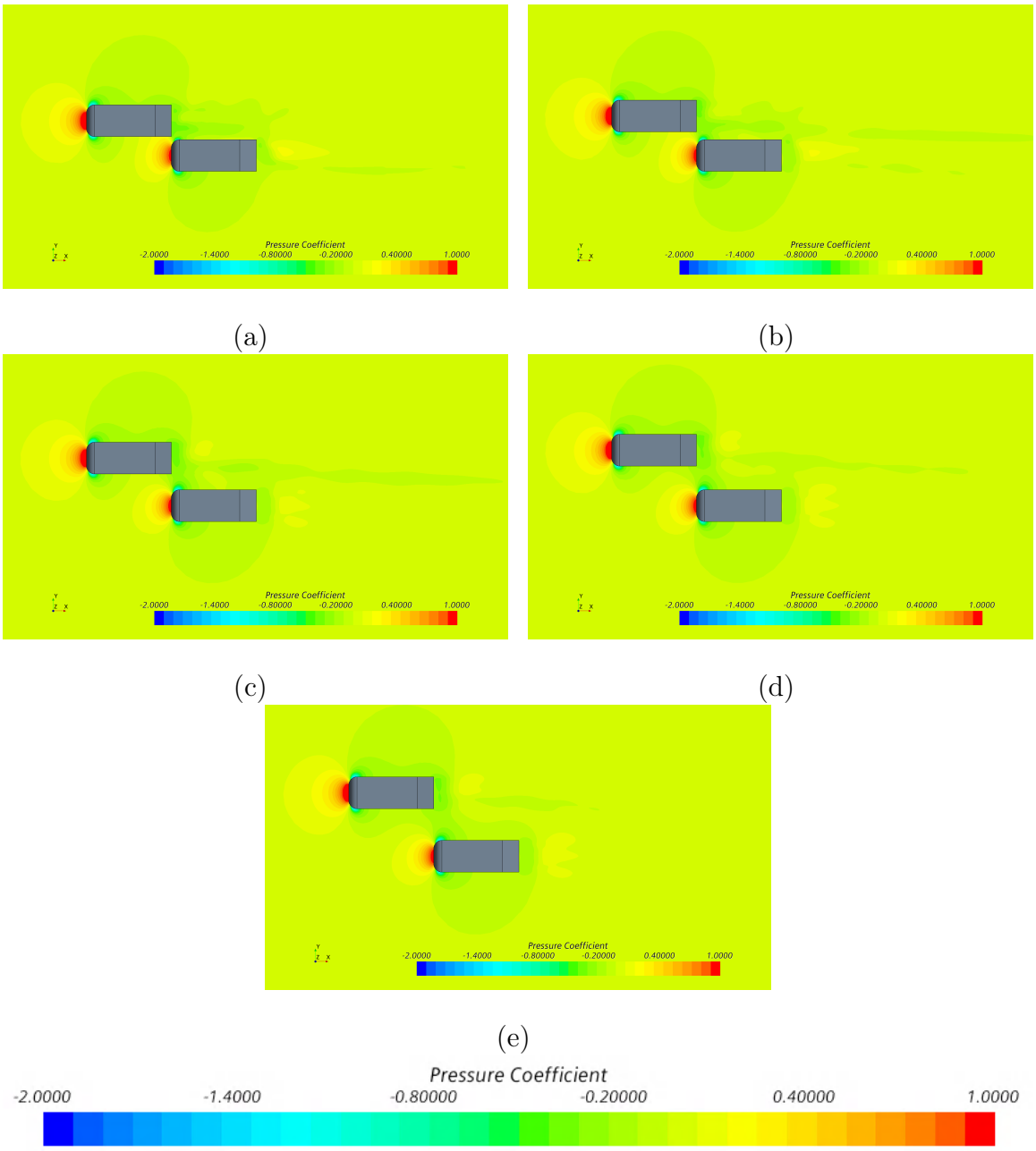

Figure 4.52: Pressure distributions along the two vehicle heterogeneous system at x/L=2 for (a) W*=0.10, (b) W*=0.25, (c) W*=0.50, (d) W*=0.75, and (e) W*=1.0

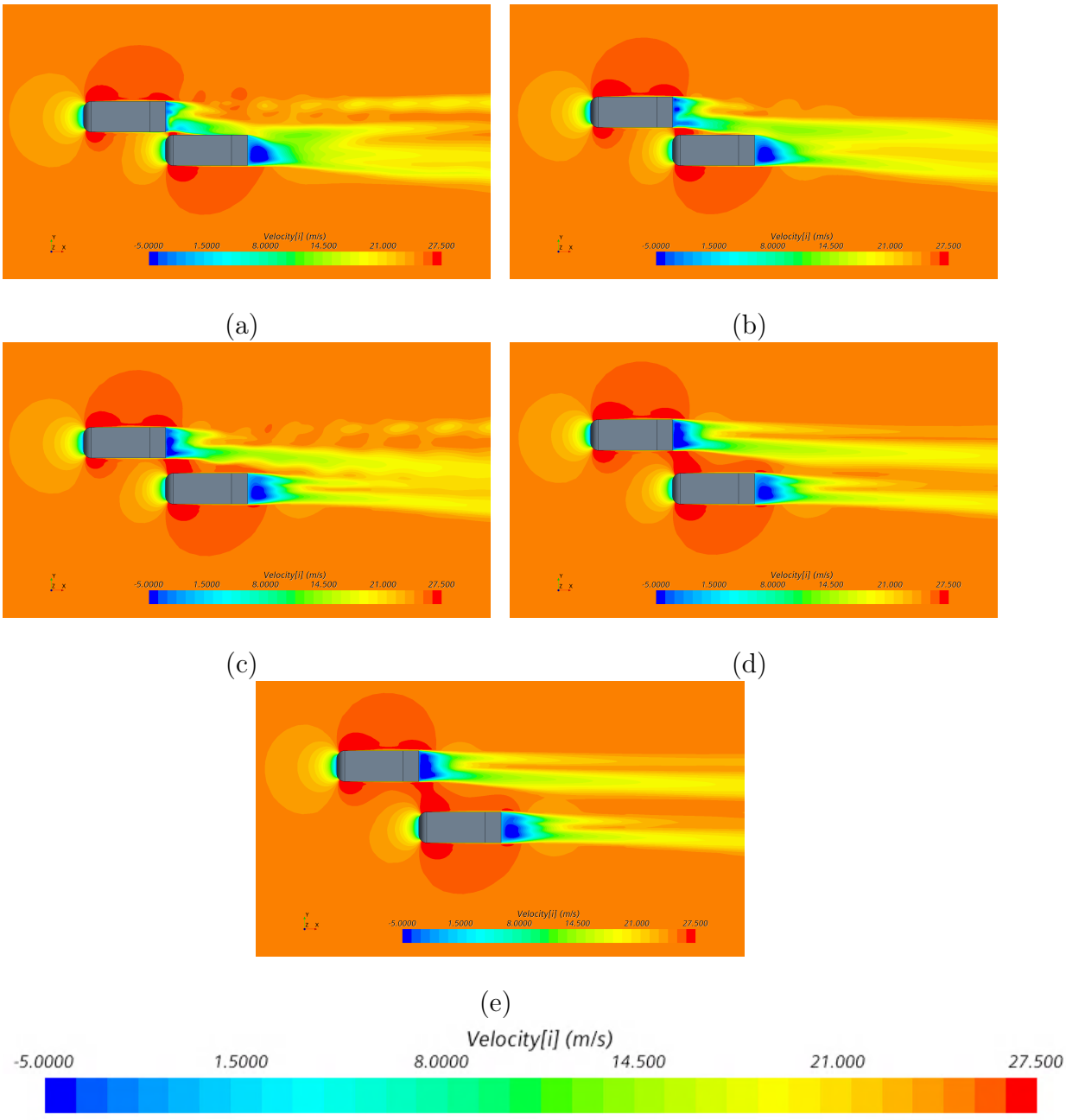

Figure 4.53: Vx distributions along the two vehicle homogeneous system at x/L=2 for (a) W*=0.10, (b) W*=0.25, (c) W*=0.50, (d) W*=0.75, and (e) W*=1.0

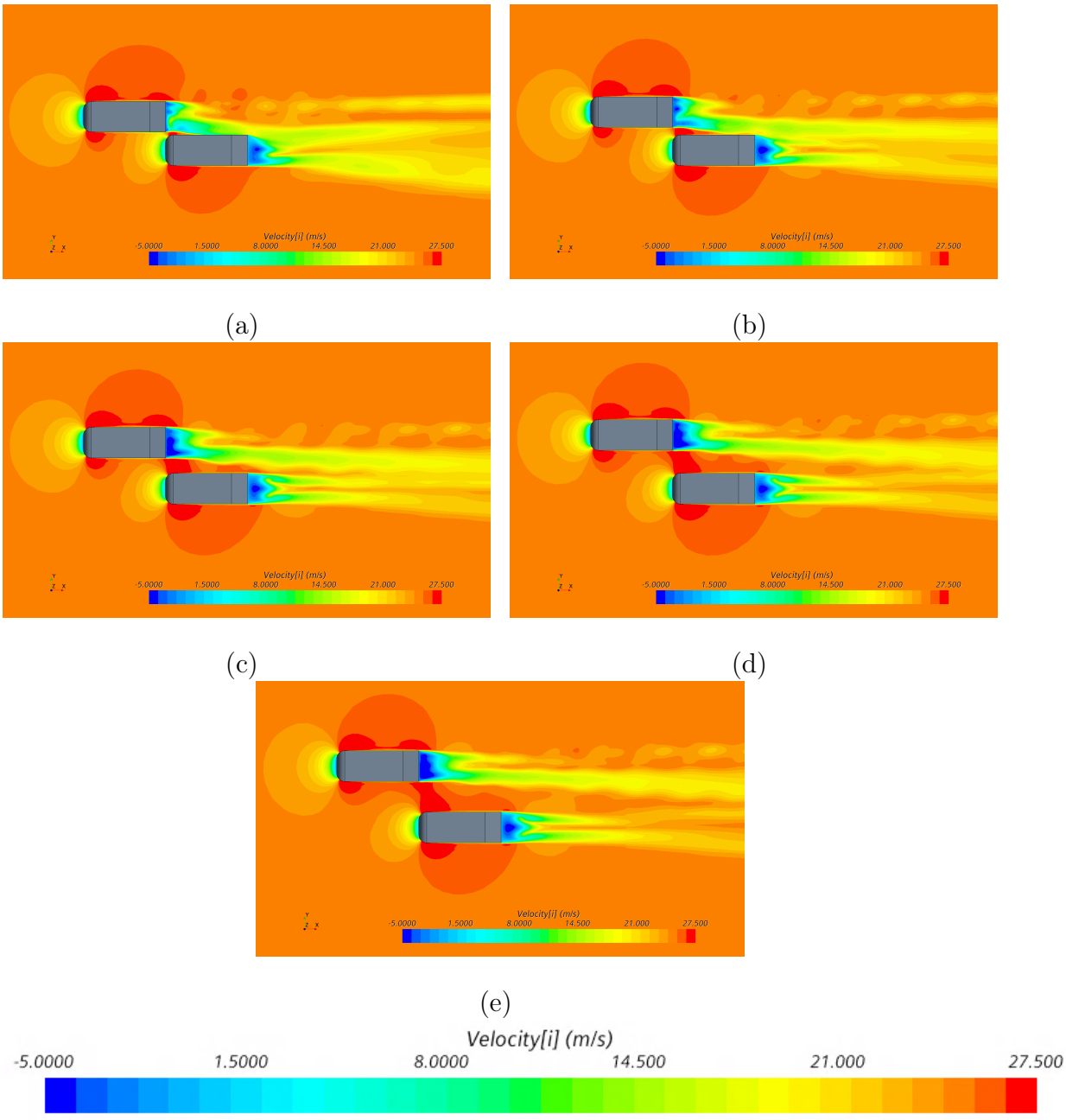

Figure 4.54: Vx distributions along the two vehicle heterogeneous system at x/L=2 for (a) W*=0.10, (b) W*=0.25, (c) W*=0.50, (d) W*=0.75, and (e) W*=1.0

Figures 4.53 through 4.58 show the distribution of Vx, Vy, and Vz at 2L when the rear of the overtaking vehicle is inline with the nose of the overtaken vehicle. A huge interaction of the wake region behind the overtaking vehicle with the overtaken vehicle can be seen in the scenes for the x-component of velocity. Due to the changes in the x-component of the velocity, a significant increase in the 'y' and 'z' components of the velocity can be observed at the front of the overtaken vehicle in order to compensate for it. This interaction is stronger at close proximities for smaller lateral spacings. As the lateral distance increases, it can be seen that the wake regions tend to separate and maintain their own unique trail. A similar pattern can be observed for the y-component of velocity. The wake region of the overtaking vehicle can be seen being largely effected by the presence of the overtaken vehicle geometry. However, as the lateral spacing increases, this effect can be seen having lesser impact owing to smaller peaks of the side force and yawing moment coefficient values for both overtaken and overtaking vehicles. Higher variations in the z-component of velocity were noticed in the homogeneous case at this location with 35^o Ahmed body model as the overtaken model

The trends in behavior of all the force and moment coefficients analysed agree well with the existing experimental data by Noger [13], Gillerion [14], Pagliarella [10], and Watkins [9]. This section completes the qualitative analysis on the effects of an overtaking maneuver for homogeneous and heterogeneous combinations of Ahmed body geometries using CFD.

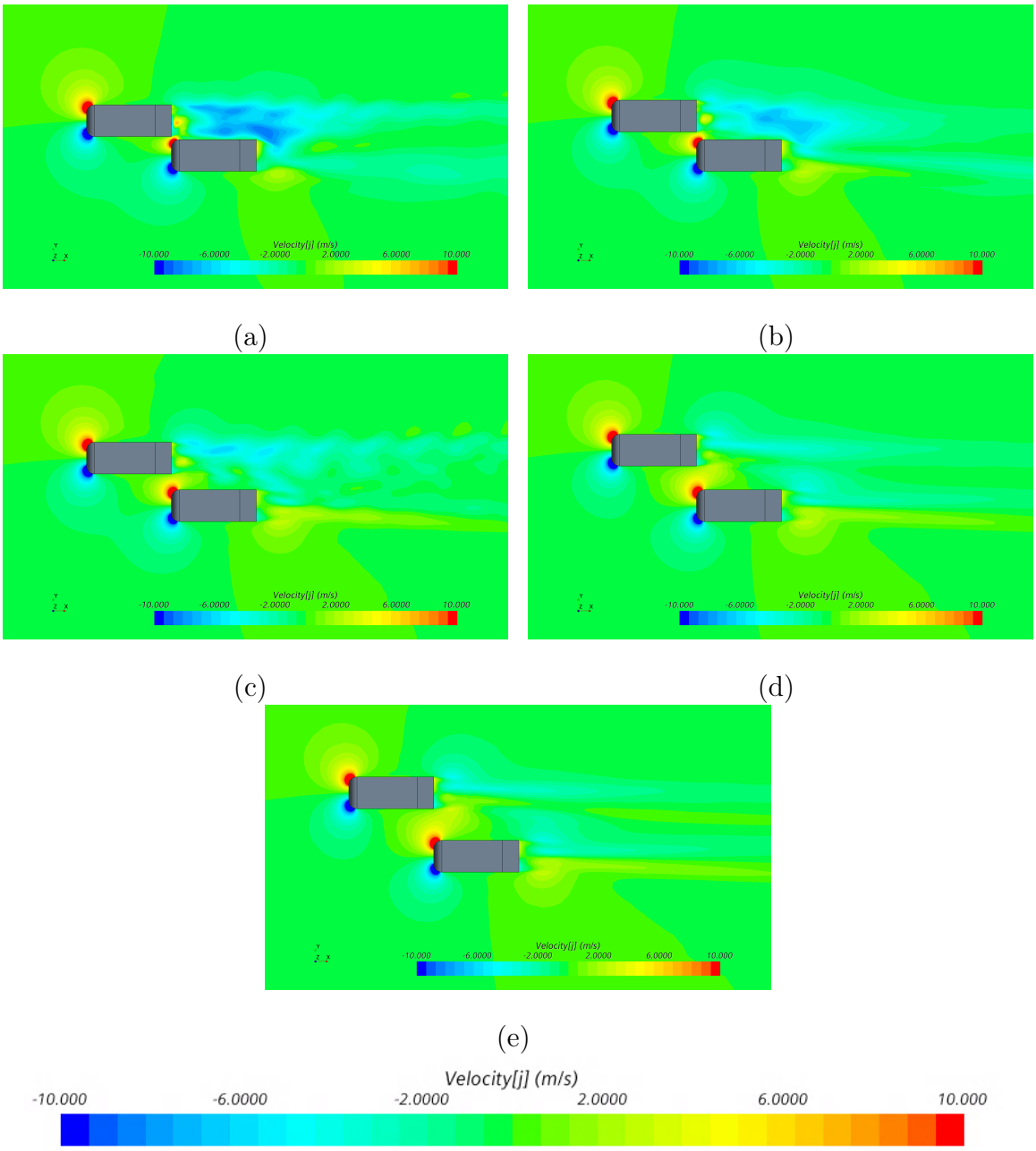

Figure 4.55: Vy distributions along the two vehicle homogeneous system at x/L=2 for (a) W*=0.10, (b) W*=0.25, (c) W*=0.50, (d) W*=0.75, and (e) W*=1.0

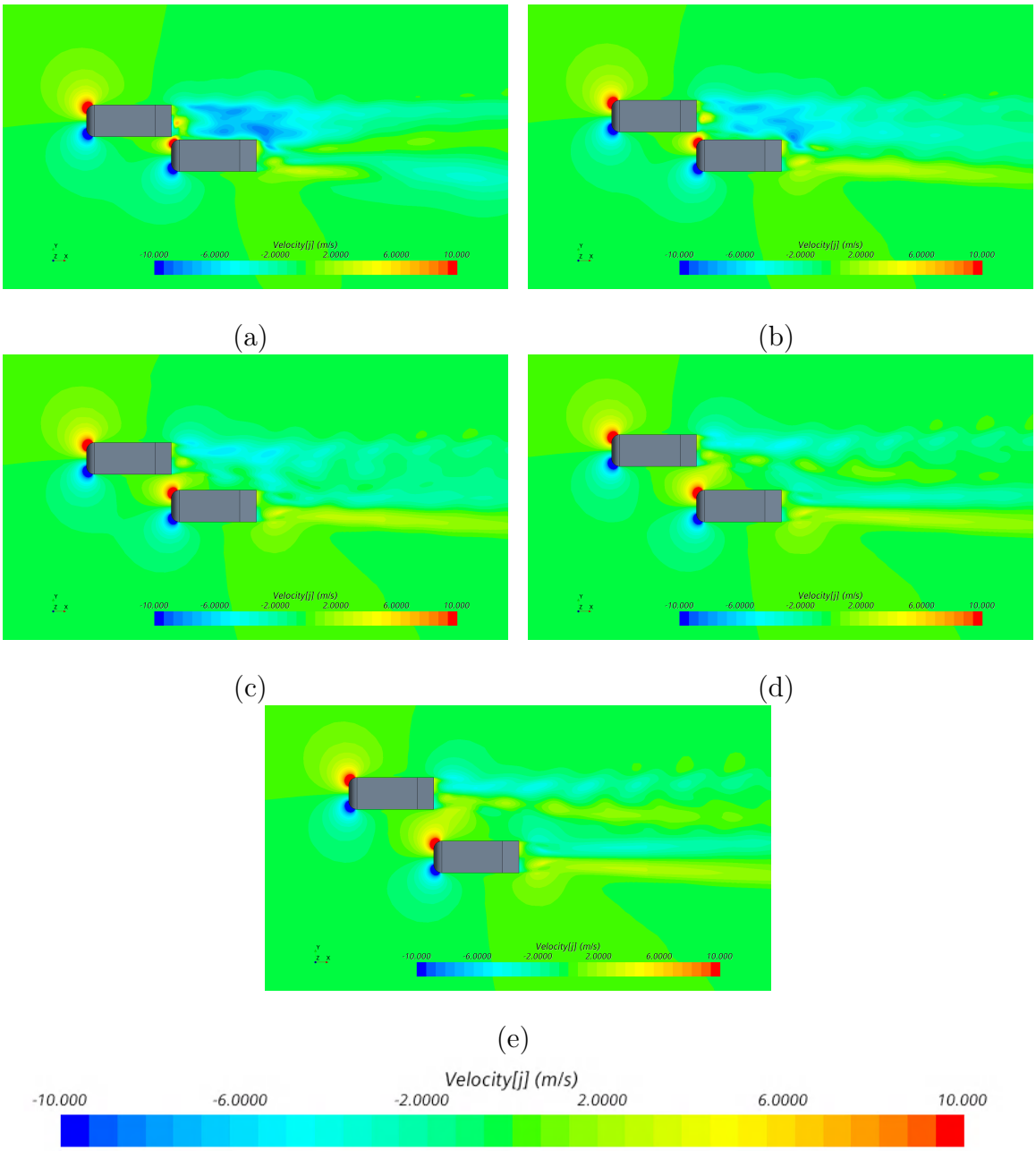

Figure 4.56: Vy distributions along the two vehicle heterogeneous system at x/L=2 for (a) W*=0.10, (b) W*=0.25, (c) W*=0.50, (d) W*=0.75, and (e) W*=1.0

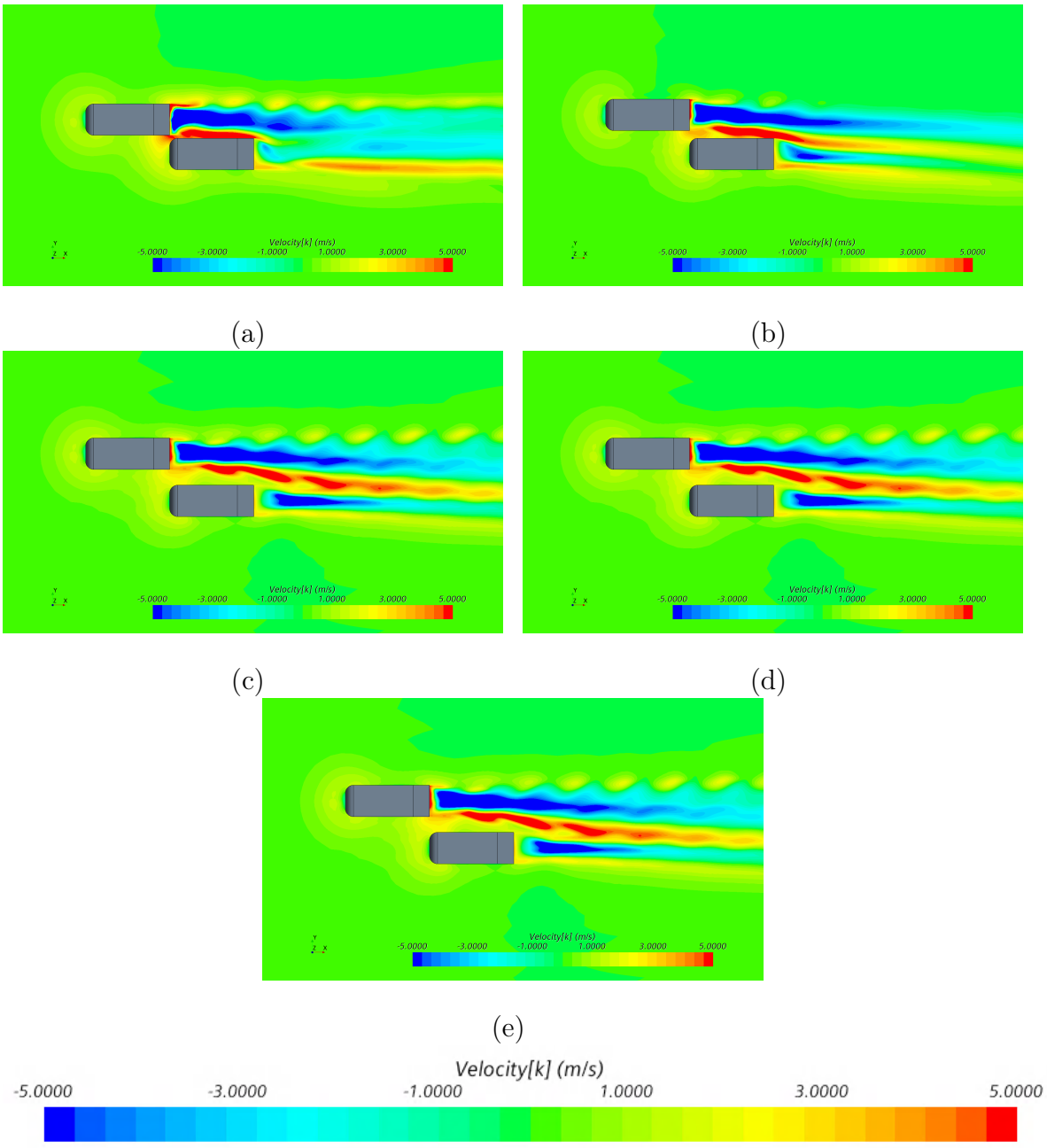

Figure 4.57: Vz distributions along the two vehicle homogeneous system at x/L=2 for (a) W*=0.10, (b) W*=0.25, (c) W*=0.50, (d) W*=0.75, and (e) W*=1.0

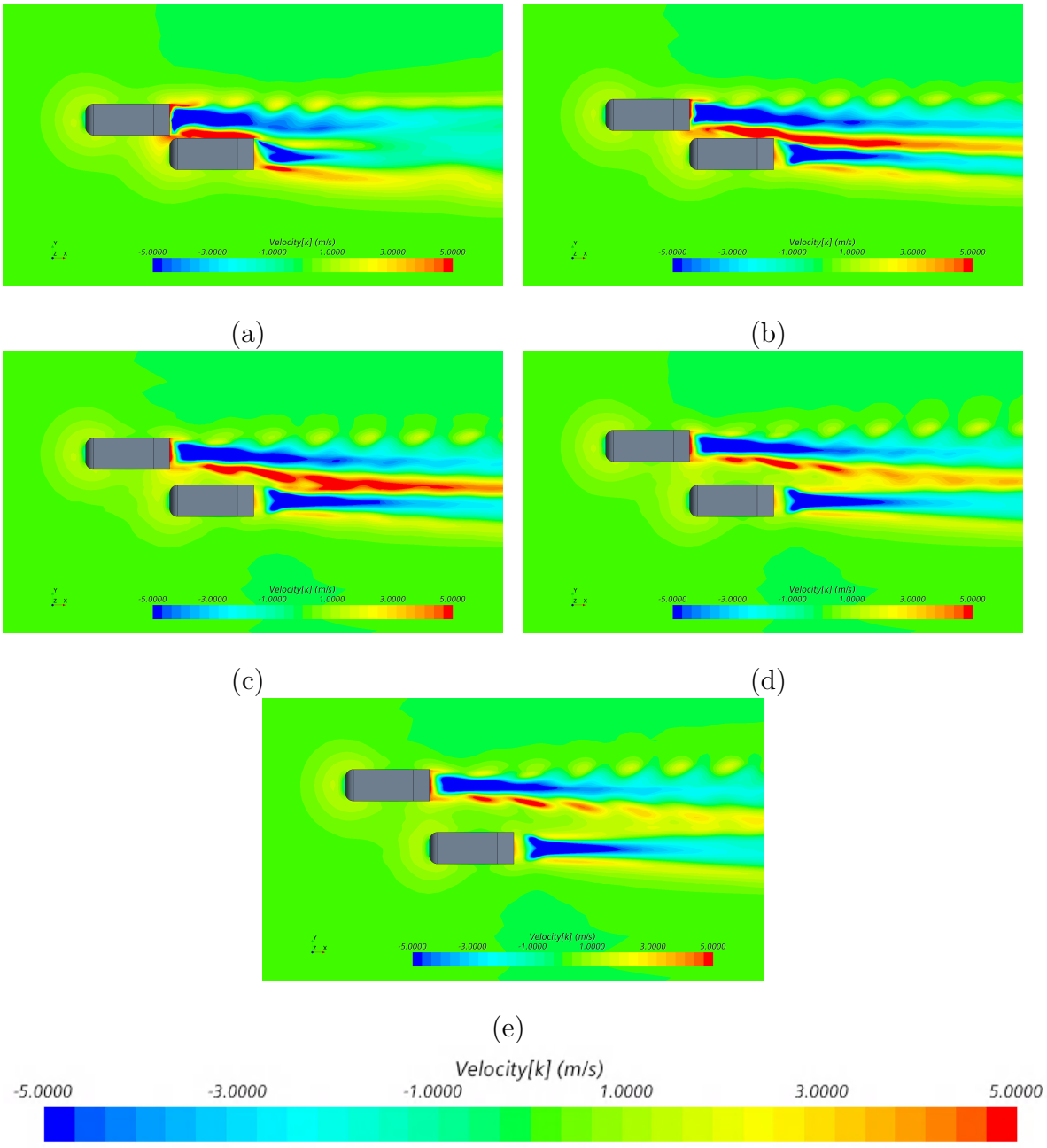

Figure 4.58: Vz distributions along the two vehicle heterogeneous system at x/L=2 for (a) W*=0.10, (b) W*=0.25, (c) W*=0.50, (d) W*=0.75, and (e) W*=1.0

CHAPTER 5: CONCLUSIONS

This chapter details the summary of the research performed in this study and discusses the several conclusions that can be made from this study. The objective of this research work was to develop and validate a CFD methodology that can be used to explore the transient effects of an overtaking maneuver. The work presented further aims to discuss the effects of lateral or transverse spacing on the various aerodynamic properties of both the overtaking and overtaken vehicles and to provide an understanding of the effects of heterogeneity in the multi-body system.

This was realized by studying the Ahmed body model in detail and developing a baseline simulation methodology that can universally be used for isolated Ahmed bodies geometries with slant angles (ϕ) of 25^o and 35^o respectively. The results from the CFD of isolated Ahmed body simulations were compared with and validated using the experimental studies conducted by Ahmed [3], Strachan [23], and Serre [1] in order to ensure proper prediction of the flow field and the aerodynamic properties of both bodies. The drag coefficient obtained for both Ahmed body geometries was found to be within an acceptable margin of the value observed by Strachan [23] with a difference in prediction of nearly 1%.

Multi-vehicle interactions of several platooning and overtaking scenarios were studied in detail to understand the trends in behavior of the several aerodynamic force and moment coefficients and to gain an understanding into the transient effects of the flow structures that were found experimentally. Following this study, the URANS simulations for the homogeneous (35^o,35^o) and heterogeneous (35^o,25^o and 25^o,35^o) studies were setup using an overset meshing technique with a relative velocity equal to 10% of the free-stream velocity. A spectral analysis was conducted for the plots of the

aerodynamic force and moment coefficients obtained from the simulations to remove unwanted numerical noise in the system. A detailed analysis of force and moment coefficients was made, the results of which strongly support the existing experimental literature. The trends in behavior of the drag coefficient, side force coefficient, and the yawing moment coefficient were closely comparable with the results of Noger [13], Gillerion [14], and Uystepruyst [15].

Following the analysis of the effects of overtaking phenomenon on the trends in aerodynamic properties, the effects of lateral or transverse spacing were studied. It was found that the trends in behavior of the aerodynamic force and moments largely remained similar for all lateral spacings. However, the amount of lateral spacing significantly effected the amount of pressure interactions between the two vehicles in the early stages of the simulations. This resulted in varying peak values of the force and moment coefficients. It is interesting to observe, however, that the location of the maximums and minimums observed in the force and moment coefficients remained at the same position while their magnitude differed as an inverse function of lateral spacing. A similar trend was observed once the overtaking vehicle started passing the overtaken vehicle. While the trends were reversed as was predicted in the several experimental literature, the pressure interactions between the two vehicles were very sensitive to the proximity of the two bodies. To summarize, as the lateral spacing between the two vehicles decreased, the effects due to the interference of one vehicle on another increased significantly (which can be understood by studying the side force and yawing moment coefficients of both vehicles) which correlates well with the studies performed by Noger [13] and Uystepruyst [15].

Lastly, the effects of heterogeneity were also studied by varying the geometry of both overtaking and overtaken vehicles while retaining the other using the two configurations of Ahmed body geometries. It was found that the effects of heterogeneity on the overtaken vehicle due to varying the geometry of the overtaking body were

minimal and the trends in behavior of the aerodynamic properties largely remained unchanged for both bodies. However, significant changes in the peak values of the maximums and minimums were observed on the aerodynamic properties of the overtaken vehicle when heterogeneity was introduced by varying the overtaken body geometry although the positions of the points of interest still remained the same. From this study, it can be concluded that the overall aerodynamic performance of the multi-vehicle system is broadly dominated by the geometric configuration of the overtaken vehicle model regardless of the heterogeneity of the system supporting the conclusions of Pagliarella [10], Watkins [9], and Uystepruyst [15].

The agreement of these observations with existing literature highlight the capability of the turbulence model and meshing techniques used to accurately capture the transient flow characteristics during an overtaking maneuver. The results obtained are promising and provide a detailed insight into the effects of lateral spacing and the effects of heterogeneity in multi-vehicle systems. The usability and universality of the numerical setup can be used for repeatability in any future work.

5.1 Future Work

The ability of the numerical setup to accurately capture the transient flow characteristics can be used in the understanding of the effects of several other factors such as varying relative velocities and yaw angles. Different platooning and overtaking conditions can be studied introducing one or more vehicle geometries in different configurations. The current study can be used as a baseline to study the overtaking effects of more realistic vehicle models such as the DrivAer model highlighting the differences of using a more representative vehicle model. Furthermore, the data collected from this investigation can be used to help in developing real-time path planning approaches by using predictive behavior-based control modules or sequences for trajectory planning of future vehicles with partial or full automation during an overtaking maneuver.

REFERENCES

[1] E. Serre, M. Minguez, R. Pasquetti, E. Guilmineau, G. B. Deng, M. Kornhaas, M. Schafer, J. Frohlich, C. Hinterberger, and W. Rodi, "On simulating the turbulent flow around the ahmed body: A french-german collaborative evaluation of les and des," *Computers & Fluids*, vol. 78, pp. 10–23, 2013.

[2] B. F. Zhang, S. To, and Y. Zhou, "Strouhal numbers of unsteady flow structures around a simplified car model," in *Fluid-Structure-Sound Interactions and Control* (Y. Zhou, Y. Liu, L. Huang, and D. H. Hodges, eds.), (Berlin, Heidelberg), pp. 179–184, Springer Berlin Heidelberg, 2014.

[3] S. R. Ahmed, G. Ramm, and G. Faltin, "Some salient features of the time - averaged ground vehicle wake," *SAE Transactions*, vol. 93, pp. 473–503, 1984.

[4] J. McNally, N. Mazellier, F. Alvi, and A. Kourta, "Control of salient flow features in the wake of a 25^o ahmed model using microjets," *Experiments in Fluids*, vol. 60, 2018.

[5] I. Bayraktar, D. Landman, and O. Baysal, "Experimental and computational investigation of ahmed body for ground vehicle aerodynamics," *SAE Transactions*, 2001.

[6] C. Hinterberger, M. García-Villalba, and W. Rodi, "Large eddy simulation of flow around the ahmed body," in *The Aerodynamics of Heavy Vehicles: Trucks, Buses, and Trains* (R. McCallen, F. Browand, and J. Ross, eds.), (Berlin, Heidelberg), pp. 77–87, Springer Berlin Heidelberg, 2004.

[7] R. J. Martinuzzi and B. Havel, "Turbulent flow around two interfering surface-mounted cubic obstacles in tandem arrangement," *Journal of Fluids Engineering*, vol. 122, 2000.

[8] P. Schito and F. braghin, "Numerical and experimental investigation on vehicles in platoon," *SAE International Journal of Commercial Vehicles*, vol. 5, pp. 63–71, apr 2012.

[9] S. Watkins and G. Vino, "The effect of vehicle spacing on the aerodynamics of a representative car shape," *Journal of Wind Engineering and Industrial Aerodynamics*, vol. 96, no. 6, pp. 1232–1239, 2008. 5th International Colloquium on Bluff Body Aerodynamics and Applications.

[10] R. M. Pagliarella, S. Watkins, and A. Tempia, "Aerodynamic performance of vehicles in platoons: The influence of backlight angles," in *SAE World Congress Exhibition*, SAE International, apr 2007.

[11] H. Humphreys and D. Bevly, "Computational fluid dynamic analysis of a generic 2 truck platoon," in *SAE 2016 Commercial Vehicle Engineering Congress*, SAE International, sep 2016.

[12] R. G. Dominy, "The influence of slipstreaming on the performance of a grand prix racing car," *Proceedings of the Institution of Mechanical Engineers, Part D: Journal of Automobile Engineering*, vol. 204, no. 1, pp. 35–40, 1990.

[13] C. Noger, C. Regardin, and E. Szechenyi, "Investigation of the transient aerodynamic phenomena associated with passing manoeuvres," *Journal of Fluids and Structures*, vol. 21, no. 3, pp. 231–241, 2005. Marine and Aeronautical Fluid-Structure Interactions.

[14] P. GilliÃ©ron and C. Noger, "Contribution to the analysis of transient aerodynamic effects acting on vehicles," in *SAE 2004 World Congress Exhibition*, SAE International, mar 2004.

[15] D. Uystepruyst and S. KrajnoviÄ, "Numerical simulation of the transient aerodynamic phenomena induced by passing manoeuvres," *Journal of Wind Engineering and Industrial Aerodynamics*, vol. 114, pp. 62–71, 2013.

[16] M. Uddin, A. D. Chellaram, and A. C. Robinson, "Cfd investigations of the aerodynamics of vehicle overtaking maneuvers," *AIP Conference Proceedings*, vol. 1851, no. 1, p. 020085, 2017.

[17] S. Yamamoto, K. Yanagimoto, H. Fukuda, H. China, and K. Nakagawa, "Aerodynamic influence of a passing vehicle on the stability of the other vehicles," *JSAE Review*, vol. 18, no. 1, pp. 39–44, 1997.

[18] C. Noger and P. Gillieron, "Banc experimental d'analyse des phenomenes aerodynamiques automobiles," in *16th French Mechanical Congress (CFM)*, Nice, Sep 2003.

[19] C. Noger and E. Szechenyi, "Experimental study of the transient aerodynamic phenomena generated by vehicle overtaking," in *Eighth International Conference on Flow-Induced Vibration (FIV)*, Ecole Polytechnique, Jul 2004.

[20] R. Corin, L. He, and R. Dominy, "A cfd investigation into the transient aerodynamic forces on overtaking road vehicle models," *Journal of Wind Engineering Industrial Aerodynamics*, vol. 96, no. 8-9, pp. 1390–1411, 2008.

[21] A. D. Chellaram, "Simulation of an overtaking maneuver using simplified vehicle bodies," 2016.

[22] H. Lienhart, C. Stoots, and S. Becker, "Flow and turbulence structures in the wake of a simplified car model (ahmed modell)," in *New Results in Numerical and Experimental Fluid Mechanics III* (S. Wagner, U. Rist, H.-J. Heinemann, and R. Hilbig, eds.), (Berlin, Heidelberg), pp. 323–330, Springer Berlin Heidelberg, 2002.

[23] R. K. Strachan, K. Knowles, and N. J. Lawson, "A cfd and experimental study of an ahmed reference model," in *SAE 2004 World Congress Exhibition*, SAE International, mar 2004.

[24] R. Strachan, K. Knowles, and N. Lawson, "The vortex structure behind an ahmed reference model in the presence of a moving ground plane," *Experiments in Fluids*, vol. 42, pp. 659–669, 05 2007.

[25] M. Minguez, R. Pasquetti, and E. Serre, "High-order large-eddy simulation of flow over the âahmed bodyâ car model," *Physics of Fluids*, vol. 20, no. 9, p. 095101, 2008.

[26] E. Guilmineau, "Computational study of flow around a simplified car body," *Journal of Wind Engineering and Industrial Aerodynamics*, vol. 96, no. 6, pp. 1207–1217, 2008. 5th International Colloquium on Bluff Body Aerodynamics and Applications.

[27] E. Guilmineau, G. Deng, A. Leroyer, P. Queutey, M. Visonneau, and J. Wackers, "Assessment of hybrid rans-les formulations for flow simulation around the ahmed body," *Computers Fluids*, vol. 176, pp. 302–319, 2018.

[28] K. HanjaliÄ, M. Popovac, and M. HadÅŸiabdiÄ, "A robust near-wall elliptic-relaxation eddy-viscosity turbulence model for cfd," *International Journal of Heat and Fluid Flow*, vol. 25, no. 6, pp. 1047–1051, 2004.

[29] G. Houzeaux, B. Eguzkitza, R. Aubry, H. Owen, and M. VÃ¡zquez, "A chimera method for the incompressible navierâstokes equations," *International Journal for Numerical Methods in Fluids*, vol. 75, no. 3, pp. 155–183, 2014.

[30] F. Menter, *Zonal Two Equation k-w Turbulence Models For Aerodynamic Flows*.

[31] D. C. Wilcox, "Reassessment of the scale-determining equation for advanced turbulence models," *AIAA Journal*, vol. 26, no. 11, pp. 1299–1310, 1988.

[32] W. P. Jones and B. E. Launder, "The prediction of laminarization with a two-equation model of turbulence," *International Journal of Heat and Mass Transfer*, vol. 15, pp. 301–314, 1972.